





Metals as Energy Carriers: Analysis of the Turbulent Flame Front of Iron Particle Cloud Combustion

Master Thesis of

Alessandra Zannini

At the Department of Mechanical Engineering, Institute of Fluid Mechanics

Advisors: M.Sc. Gabriel Thäter

Prof. Dr.-Ing. Bettina Frohnapfel

Prof. Dr. Oliver Stein

Prof. Dr. Luciano Rolando

Duration: April 2025 - September 2025

I declare that I have developed and written the enclosed thesis completely by myself, and have not used sources or means without declaration in the text.
Karlsruhe, 15. 09. 2025
(Alessandra Zannini)

Abstract

This thesis investigates the combustion of iron particle clouds as a potential pathway for renewable energy storage and conversion. Iron is considered a promising energy carrier due to its high volumetric energy density, abundance, and the possibility of integrating its redox cycle into a circular energy economy. Unlike conventional gaseous or volatile solid fuels, iron combustion is heterogeneous: the flame propagates through a cloud of reacting particles making the definition of a flame front not straightforward.

To address this challenge, post-processing routines have been developed and tested to capture the flame front in numerical simulations of propagating iron flames under both laminar and turbulent conditions. The methodology builds on concepts from premixed turbulent flames, where correlations between flame speed and flame surface are well established, and explores their transferability to heterogeneous metal combustion. In particular, interface reconstruction techniques inspired by the Volume of Fluid (VoF) method have been adapted to identify and quantify the reaction surface from particle-based simulation data.

The results provide initial insights into the relationship between the intensity of turbulence, the evolution of the flame surface, and the speed of propagation of the flame in iron combustion. By comparing the behavior of iron particle clouds with established results from premixed flames, the study highlights both the potential and the limitations of extending classical turbulent combustion theory to heterogeneous iron ignition.

Contents

ΑD	DSLFACE	V
No	omenclature	ix
Ac	cronyms	хi
1.	Introduction	1
	1.1. The Energy Transition	
	1.2. The Role of Iron	
	1.3. Research Objectives	
2.	Literature research	5
	2.1. Premixed Flames	5
	2.1.1. What is a premixed flame?	6
	2.1.2. What is a <i>flamelet</i> structure?	8
	2.2. Existing correlation between the burning speed and the flame structure	11
	2.2.1. <i>Flamelet</i> Regime	14
	2.2.2. Distributed-Reaction Regime	14
	2.2.3. The Borghi–Williams Diagram	
	2.2.4. The progressive parameter	
	2.3. Comparison with the ignition behavior of iron particles in HIT	18
3.	Methodology	21
	3.1. Description of the model	21
	3.1.1. Fluid phase model	21
	3.1.2. Particle phase	22
	3.2. Simulation setup: one-dimensional homogeneous propagating flame	
	3.2.1. Laminar case	
	3.2.2. Turbulent case	
	3.3. Postprocessing routine: flame front detection	
	3.3.1. Geometric VOF: reconstructor step	
	3.3.2. Marching cubes algorithm	29
4.	Results and evaluations	35
	4.1. Iso-surface reconstruction: inaccuracies and influencing parameters	35
	4.1.1. Flame Front Visualization	39
	4.1.1.1. Laminar case	40
	4.1.1.2. Turbulent case	41
	4.1.2. Number of boxes N_b	42
	4.1.3. Iso-value C_{ox}^{level}	45
	4.1.4. Iso-value T^{level}	47
	4.2. Comparing different simulation setups: one-direction propagating flames	49
	4.2.1. Different N_{part}	49
	4.2.2. Different ϵ : relation between flame speed and flame surface	51
5 .	Conclusion	59

List of	Figures	5	61
List of	Tables		65
Bibliog	raphy		67
Append	dix		71
A.	Premi	xed Flames	71
	A.1.	Bray-Moss-Libby model	71
	A.2.	Bray-Cant Formulation Derivation	71
	A.3.	Markstein Number	71
В.	Furth	er developments of model equations	72
	B.1.	Voronoi Tesselation	
С.	Addit	ional plots	74
	C.1.	Fluid isothermal lines	74
	C.2.	Flame thickness definition	75
	C.3.	Different simulation setup	77

Nomenclature

 d_p

 m_p

 C_{ox}

$Greek\ symbols$ Flame thickness δ_L Characteristic kinetic time scale au_f Mass fraction ω Φ Equivalence ratio Kinematic viscosity Shear stress au_{ij} Kolmogorov length-scale Dissipation energy Dynamic viscosity μ Σ Flame surface density Coordinate normal to the brush η_{flame} Density Pressure Oscillations due to momentum π Volume fraction α Roman symbols LDomain length L_b Grid cell length Diffusivity D_{O_2} Mass fraction ω_i R_M Gas constant ReReynolds number ShSherwood number NuNusselt number PrPrandtl number StStokes number DaDamköhler number KaKarlovitz number u'Root mean square of velocity fluctuations Progressive parameter cIntegral turbulent length-scale L_T Wrinkled surface area A_T A_L Not-wrinkled surface area S_T Turbulent burning velocity S_L Laminar burning velocity k_d Diffusive transfer coefficient Arrhenius kinetic constant k_r

Particle diameter Specific enthalpy Particle mass

Oxidation fraction

 $egin{array}{ll} \mathbf{V}_{Flame} & ext{Flame velocity} \\ \mathbf{V}_{Gas} & ext{Flow velocity} \end{array}$

Subscripts

 $\begin{array}{ll} p & & \text{Particle quantity} \\ f & & \text{Fluid quantity} \end{array}$

 δ Flame thickness quantity

 $egin{array}{ll} x & ext{x-coordinate} \\ y & ext{y-coordinate} \\ \end{array}$

z Flame propagation direction coordinate

 $egin{array}{lll} ox & {
m Oxidation} \ u & {
m Unburnt} \ b & {
m Burnt} \ \end{array}$

Superscripts

 $\begin{array}{ll} + & \text{Positive direction} \\ - & \text{Negative direction} \\ 0 & \text{Initial quantity} \\ i,j,k & \text{Cell quantity} \end{array}$

Acronyms

LHV	Lower Heating Value
DNS	Direct numerical simulation
CP-DNS	Carrier phase direct numerical simulation
ODE	Ordinary Differential Equations
FVM	Finite volume method
VOF	Volume of fluid
PLIC	Piecewise-linear interface construction
SLIC	Simple line interface construction
MC	Marching Cubes
FSD	Flamse surface density
BML	Bray-Moss-Libby
PDF	Probability Density Function

1. Introduction

1.1. The Energy Transition

At the COP28 summit in 2023, nearly 200 countries signed a landmark agreement committing to collectively double the global average annual rate of energy efficiency improvements by 2030. This ambitious goal reflects the recognition that efficiency is a key driver of the transition away from fossil fuels. However, the path towards an effective transition remains highly challenging. One year after the agreement, progress in accelerating efficiency improvements has been modest and stronger policy measures are urgently required to achieve the desired transformation.

According to the International Energy Agency (IEA) [1], in 2023 the energy intensity of the economy in both Germany and Italy was estimated at $2.4\,\mathrm{MJ/USD}$, while their carbon intensities amounted to $130\,\mathrm{g_{CO_2}/USD}$ and $120\,\mathrm{g_{CO_2}/USD}$, respectively [2]. Achieving net-zero emissions by 2050 requires a substantial acceleration in efficiency improvements. Nevertheless, the exploration and deployment of novel energy carriers and storage technologies will also play a crucial role.

Within this context, a promising concept under investigation is the storage of renewable energy through the cyclic reduction and oxidation of metals, also known as the *Metalenabled Cycle of Renewable Energy* (MeCRE) [3]. Metals can act as recyclable energy carriers that allow the storage of large amounts of energy over long periods. The reduction of metal oxides can be carried out in regions with abundant renewable resources, such as solar or wind power. In this way, the carbon-neutral energy produced can be stored chemically in the solid metal phase. This feature represents one of the main advantages of using metals as energy carriers: they enable secure long-term storage and efficient transport. An investigation about exploiting metals as recyclable low-carbon electrofuels is done in [4]. In this study, metal powders are burned with air to produce heat for a heat engine or with steam to produce heat and hydrogen, which are useful to power fuel cells.

A direct comparison is relevant with hydrogen, widely considered the leading energy carrier of the transition, especially when produced sustainably as green hydrogen. However, while hydrogen has an extremely high specific energy, its volumetric energy density is much lower than that of metals. Thus, hydrogen storage and transport remain highly complex [3]: compressed hydrogen requires very high pressures, liquefied hydrogen demands extreme cryogenic conditions, and both include high energy costs and safety concerns. Another alternative approach is to store hydrogen in hydrogen-rich compounds, such as ammonia NH₃, which require lower pressures for liquefaction[5]. However, there are clear concerns regarding its toxicity, odor and vapor explosions. By contrast, metal fuels can be safely transported and stored as solids, offering a more practical solution for long-distance and seasonal energy storage.

Figure 1.1 shows a comparison between different possible fuels, including metals (aluminum Al, iron Fe, silicon Si, magnesium Mg et al.), emerging fuels such as liquefied or compressed hydrogen H_2 and ammonia NH_3 , and conventional fuels such as coal. The x-axis reports the gravimetric energy density expressed in $kW h kg^{-1}$, while the y-axis shows the volumetric energy density in $kW h L^{-1}$. From this plot, it becomes evident that metals exhibit a

much higher volumetric energy density compared to other emerging technologies (hydrogen, ammonia), coal, or even lithium-based batteries. However, their gravimetric energy density is significantly lower.

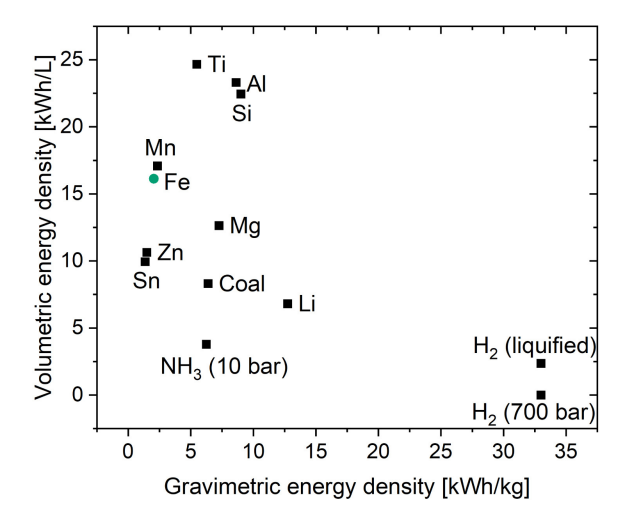


Figure 1.1.: Volumetric and gravimetric energy densities of possible metal fuels, coal, ammonia and hydrogen reprinted from [6]

Several metals have been identified as potential energy carriers, including silicon [7], aluminum[8] and iron [6] which are the second, third and fourth most abundant element in the Earth's crust, respectively [3]. Among these, iron is considered the most promising due to its high volumetric energy density and its heterogeneous combustion in air at ambient pressure, which prevents iron and its oxides from entering the vapor phase and thus allows easier separation of combustion products.

1.2. The Role of Iron

Iron offers multiple advantages as a metal fuel: besides being one of the most abundant elements in nature, it is inexpensive, and it is non-toxic. Moreover, its boiling point is well above the typical flame temperature, which means that both iron and its oxides remain in the solid phase during combustion [9]. Table 1.1 summarize the thermophysical and energetic properties of iron, its oxides, and different coal ranks Bituminous, sub-bituminous, and lignite coals are commonly used in power plants, and mainly differ in terms of their energy density. Iron and iron oxides, on the other hand, are highly dense materials, with metallic iron showing a much higher density than coal. While the specific (mass-based) heating value of iron is lower than that of coal, its volumetric energy density is significantly higher, which is advantageous for transportation, storage, and combustion system design, since less volume is required for the same energy content. The progressive oxidation of iron reduces its heating value, which reaches zero for hematite (Fe₂O₃). In addition, the high melting points of iron and its oxides are consistent with heterogeneous combustion, where the reaction products remain in the or liquid phase. This feature enables the possibility of separating and recycling the solid oxides, which is essential for closing the iron fuel cycle.

On the other hand, issues such as the stability of the oxides, particle agglomeration, flow properties, and potential inhalation risks need to be addressed before large-scale implementation in industrial systems [3].

When comparing different energy carriers, one of the most relevant parameters is the so-called power-to-power efficiency, which reflects the share of stored energy that can be recovered.

Fuel	$\begin{array}{c} \textbf{Density} \\ [\text{kg/m}^3] \end{array}$	$\begin{array}{c} \mathbf{Melting} \\ \mathbf{Point} \ [^{\circ}\mathbf{C}] \end{array}$	$rac{ m LHV}{ m [MJ/kg]}$	$\frac{\rm LHV}{\rm [GJ/m^3]}$
Fe	7870	1538	7.36	57.92
FeO	5740	1377	2.03	11.65
Fe_3O_4	5180	1590	0.35	1.81
Fe_2O_3	5260	1565	0	0
Bituminous Coal	1200-1600	_	25-36	30–57
Sub-Bit. Coal	900 - 1200	_	20 - 25	18 – 30
Lignite	700 – 900	_	10 - 20	7-18

Table 1.1.: Properties of iron, iron oxides, and different coal ranks. Adapted from [10].

A study done by Kuhn et al. [6] pointed out a cycle efficiency of the iron redox cycle of 27%. The oxidation was modeled on the basis of a state-of-the-art coal-fired power plant (RDK-8, Karlsruhe) and an efficiency of $\eta_{\rm ox}=0.43$ was assumed. The reduction step was simulated using equilibrium reactions at $T_{\rm red}=800$ –900 °C and an hydrogen-to-iron ratio $\lambda_{\rm red}\approx 3$, resulting in an efficiency of $\eta_{\rm red}\approx 0.91$. Combining both steps yields an optimum cycle efficiency of about 39%. When also considering hydrogen production via electrolysis with an assumed efficiency of 70%, the overall round-trip (power-to-power) efficiency is reduced to about 27%, placing it above some other chemical carriers but still below electrochemical storage technologies. On contrast, lithium-ion batteries [11] can reach 85-100% efficiency, although they are not suited for shipping energy over long distances. Coal-fired power plants operate at efficiencies of about 38-42% [10], while aluminum redox cycles reach values between 25% and 40% [8]. It should be noted that the resulting efficiency of iron redox cycle neglects transport and storage losses, as well as pressure drops and heat losses in reactors, and assume pure Fe₂O₃ as the combustion product [6]. Therefore, the reported values represent upper-limit estimates of the achievable efficiency.

Figure 1.2 illustrates a schematic example of a carbon-neutral reduction-oxidation cycle of iron and its oxides [10]. In the "release" step, metallic iron is oxidized at high temperature, releasing heat in a process comparable to the combustion of conventional solid fuels. The reaction products are solid iron oxides (mainly FeO), which can be readily collected. In the subsequent "storage" step, these oxides are transported to dedicated reduction facilities, where renewable energy is used to regenerate metallic iron through either electrochemical or thermochemical processes. In the latter case, green hydrogen can serve as the reducing agent. Both routes enable the recovery of iron fuel without carbon emissions, thereby establishing a circular and sustainable energy economy.

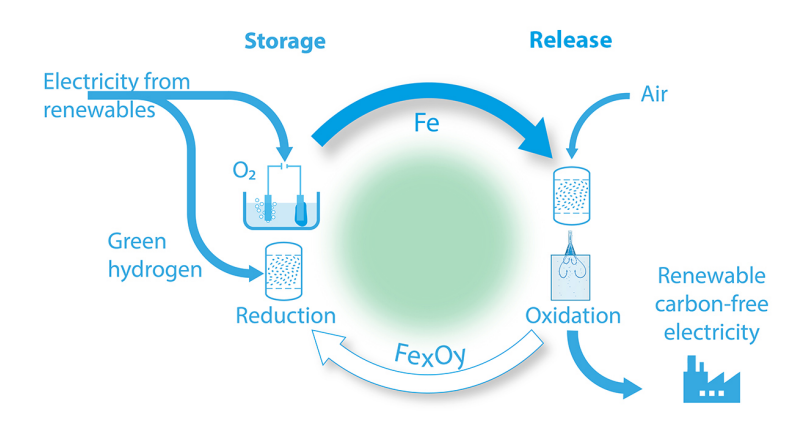


Figure 1.2.: Schematic of an iron reduction—oxidation cycle for a CO_2 -free energy supply . Reprinted from [10]

1.3. Research Objectives

The present work is motivated by the need to understand the role of turbulence in iron combustion, where the flame propagates through a cloud of reacting particles rather than a homogeneous gas mixture. In the literature, extensive studies have been devoted to premixed turbulent flames, particularly for hydrocarbon [13, 14, 15, 16] and hydrogen systems [17, 18], and a variety of correlations have been proposed to link turbulence intensity with flame speed and flame structure [19, 20, 21]. These established results provide a valuable reference point for comparison.

This perspective raises several guiding research questions. Can well-established theories of the turbulence-combustion interaction of premixed gaseous flames be translated to heterogeneous particle-cloud flames? In which way must they be adapted to account for the presence of solid particles and the formation of oxides? How can the propagation front of an iron particle cloud flame be defined and captured consistently in both numerical and experimental frameworks? And how does turbulence intensity influence the propagation speed and the internal flame structure in iron combustion?

To address these questions, a numerical model of iron particle oxidation is employed. The model assumes point particles suspended in a low-Mach-number flow and simulates their combustion in homogeneous isotropic turbulence. It captures mass and heat transfer between the particles and the surrounding gas. The chemical description is limited to the first oxidation step from metallic iron to FeO, while subsequent oxidation stages (Fe₃O₄, Fe₂O₃) are not considered.

The objectives of this thesis are therefore dual. First, to assess whether correlations established for premixed hydrocarbon and hydrogen flames can be extended to iron particle flames. Second, identify the limitations of these analogies by analyzing in detail how turbulence modifies the propagation speed and the flame structure in heterogeneous iron combustion. These objectives define the conceptual framework of the thesis and will later be revisited in the discussion and conclusion.

2. Literature research

Understanding the interaction between turbulence and flames is one of the central challenges in combustion science. Turbulence strongly modifies flame structure and morphology, thereby controlling stability, efficiency, and pollutant formation in practical systems. A large body of research has therefore focused on premixed flames, which provide representative framework for analyzing turbulence–combustion interactions.

In this chapter the basic concepts of premixed flames are introduced, including their laminar one-dimensional structure. Then, the influence of flow and turbulence on the flame front is discussed, leading to the development of the flamelet concept. Finally, existing correlations between turbulent burning velocity and flame surface area are presented, together with regime diagrams that classify flame behavior under different turbulence intensities. These concepts form the reference background for later comparison with iron particle flames.

2.1. Premixed Flames

Combustion is an exothermic chemical process in which a fuel reacts with an oxidizer, producing heat and products. Different combustion processes could be classified according to the physical state of the reactants, the degree and type of mixing between them, and the fluid flow regime. Figure 2.1 reports a schematic examples of a premixed and a diffusional flame.

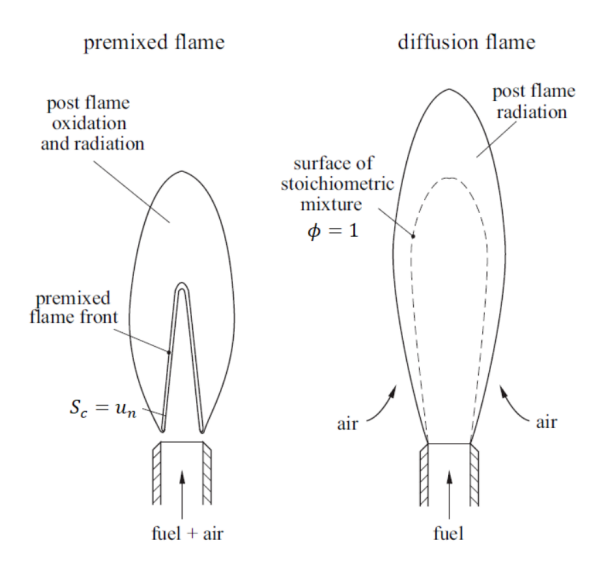


Figure 2.1.: Laminar case: premixed and diffusive flames. Reprinted from [22].

On the left-hand side of 2.1, a premixed flame is shown. Fuel and oxidizer are homogeneously mixed at the molecular level prior to ignition. The flame front thus acts as a reaction zone separating unburnt reactants from hot burnt products, with heat and mass transfer occurring primarily along the normal direction to the front. The mixture equivalence

ratio Φ is uniform throughout the unburnt gases and determines whether the flame can propagate, within lean and rich extinction limits.

On the right-hand side of 2.1, a diffusion flame (or non-premixed flame) is displayed. A premixed flame occurs when fuel and oxidizer are supplied separately and combustion takes place only in regions where they mix at the molecular level. In this case, the reaction zone is located along the interface between the fuel and oxidizer streams, and the flame structure is controlled mainly by the rate of molecular diffusion rather than by the intrinsic chemical time scales.

2.1.1. What is a premixed flame?

Semenov [23] was the pioneer on the model of the structure of premixed flames. He theorized that combustion occurs when the heat release by a chemical reaction exceeds the rate of heat loss due to diffusion towards the unburnt reactants. Later Zeldovich [24] introduced a mathematical model to describe the flame propagation speed for laminar premixed flames, by solving the diffusion and reaction equations. The internal structure features two main layers:

- *Preheat zone*: temperature rises by thermal conduction from downstream products; dominant balance between convection and diffusion in the energy equation.
- Reaction zone: rapid conversion of reactants; dominant balance between convection and chemical source terms, with comparatively smaller molecular diffusion.

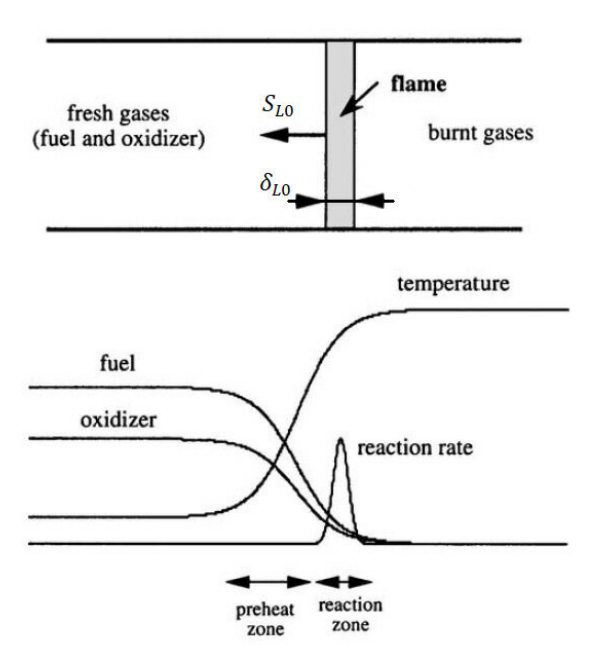


Figure 2.2.: Template for 1D laminar premixed flame profiles (temperature T, reactant mass fraction Y_{fuel} , oxidizer mass fraction $Y_{oxidizer}$, reaction rate). Reprinted from [25].

Figure 2.2 illustrates the one-dimensional structure of a laminar premixed flame. In this configuration, the fresh reactants (premixed fuel-oxidizer mixture) are separated from the hot combustion products by a thin flame front. According to the thermal theoretical model of premixed flames [26], in the preheating zone the temperature rises from the initial value T_0 toward the adiabatic flame temperature T_r , while in the reaction zone the main chemical heat release occurs. The overall premixed combustion region has a typical thickness on the

order of a millimeter, while the reaction zone within it is about one order of magnitude thinner. The flame front is defined as the region corresponding to this thin reaction zone.

Two parameters are typically used to characterize laminar premixed flames: the laminar burning velocity S_L (or consumption speed), and the laminar flame thickness δ_L , which represents the spatial extent of the temperature and species gradients across the flame front. These profiles are shown in Figure 2.2, highlighting the steep variation in temperature and composition between reactants and products across the reaction zone.

The laminar burning velocity is the speed at which a planar, not-stretched flame front propagates into a quiescent, premixed, homogeneous reactant mixture at specified thermochemical conditions. It depends only on the intrinsic chemical kinetics and the transport properties of the mixture, and it represents a fundamental reference quantity for both experiments and modeling.

The laminar flame thickness δ_L provides a measure of the spatial extent of the flame front. Although several definitions exist in the literature, a common one introduced by Zeldovich [24] relates the thickness either to the kinematic viscosity (ν) or the thermal diffusivity (α) and a characteristic velocity (u):

$$\delta_L = \frac{\nu}{u}$$
 or $\frac{\alpha}{u}$ (Zeldovich definition). (2.1)

Peters [27] applied this expression in premixed laminar flame, where the characteristic velocity is the laminar burning velocity and the thermal diffusivity $\alpha = (\lambda/(\rho c_p))_{RB}$ is evaluated at the upstream reaction layer conditions at 1500 K. Alternatively, the laminar flame thickness can be defined based on the maximum temperature gradient across the flame front,

$$\delta_T = \frac{T_b - T_u}{\left(\frac{dT}{dx}\right)\big|_{max}}$$
 Thermal definition: u stands for unburnt, while b for burnt

The two definitions coincide if evaluated at the conditions specified by Peters according to what stated in the article [22].

Both S_L and δ_L serve as reference parameters for freely propagating laminar flames and are often used to normalize turbulence—flame interaction models. Across δ_L , a steep temperature gradient preheats the unburnt mixture by thermal diffusion, initiating ignition and sustaining propagation of the flame front into the reactants at velocity S_L .

Afterwards, Lewis and von Elbe [28] highlighted the importance of the Lewis number (Le) for flame stability and structure. The Lewis number is defined as the ratio between thermal diffusivity (α) and mass diffusivity (D), thereby correlating the rates of heat and mass transport in a fluid. In the context of combustion, the Lewis number governs the relative transport rates of heat and mass across the flame front, thus exerting a critical influence on flame thickness, propagation speed, and stability. When Le=1, heat and mass diffuse at the same rate, which often simplifies the flame structure and is the assumption underlying many classical models [14, 29]. If Le < 1, mass diffuses faster than heat, leading to thinner flames with higher burning velocities and a strong tendency to develop "cellular structures" [17]. By contrast, if Le > 1, thermal diffusion dominates, resulting in broadened flames. Thus, the Lewis number is a fundamental parameter in premixed flame theory, as it directly affects flame thickness, propagation speed, and stability against perturbations.

In this context, the concepts derived from laminar flame theory provide the foundation for more advanced models, such as the *flamelet* approach, which describes how small-scale turbulent eddies interact with and wrinkle the flame front.

2.1.2. What is a *flamelet* structure?

The premixed flame structure has subsequently been studied under different flow regimes to understand how turbulent eddies interact with flame propagation. A major contribution in this area was made by F. A. Williams [30], who introduced the *flame-sheet model*. In this model, the flame front is idealized as an infinitely thin sheet separating reactants from products, across which chemical conversion and heat release occur. Despite its simplicity, this representation captures the essential role of flame geometry in determining propagation. This mechanism provides the physical foundation of the *flamelet* concept: a turbulent premixed flame can be regarded as an ensemble of wrinkled laminar flames, where geometry and kinetics jointly determine the propagation process.

Building on this idea, Michael A. Liberman [31] developed expressions valid in the flamelet regime that correlate the laminar burning velocity S_L with the turbulent burning velocity S_T . In laminar conditions, a premixed flame remains essentially one-dimensional and steady, propagating into the unburnt mixture at S_L . Under turbulent conditions, however, the flame front is no longer planar: eddies wrinkle and stretch it, increasing the surface area and complicating the propagation dynamics. As a result, S_T depends not only on chemical kinetics and transport properties, but also on the turbulent motions themselves. Experimental and numerical studies have clearly visualized these effects, revealing the strong distortion of premixed flame fronts under different turbulence intensities. Figure 2.3 displays some examples of preheat layers and reaction layers that were imaged in Bunsen, counterflow, and low-swirl burners [14].

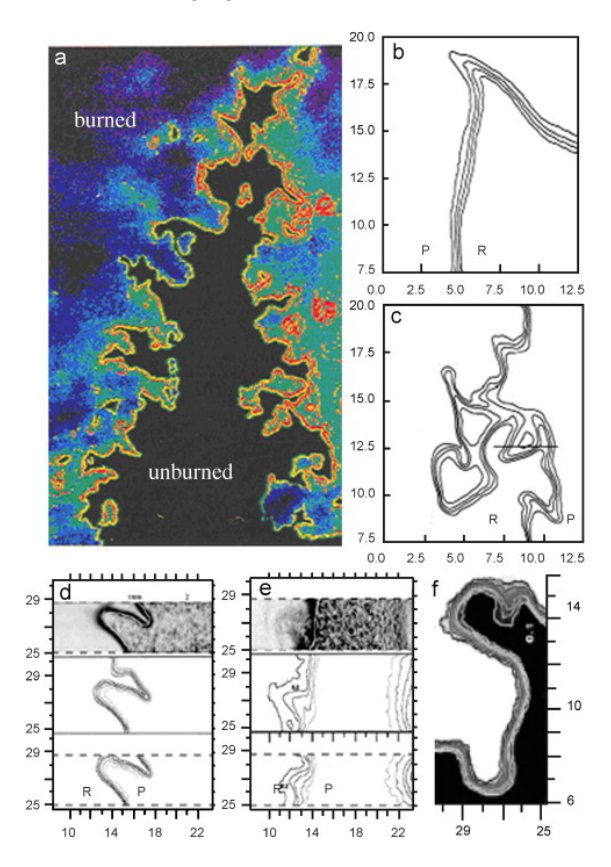


Figure 2.3.: Structure of preheat zones of flamelets in turbulent flames: several combustor have been analyzed in these experiments. Dimensions in mm. Reprinted from [14]

The term flamelet, first introduced by Williams, refers to the idea that even in a turbulent flame, the local structure can often be approximated by a laminar, one-dimensional

premixed flame. Peters [22, 27] provided the first systematic theoretical foundation for this concept, defining flamelets as:

- 1. thin wrinkled layers that contain both a preheat zone and a reaction zone,
- 2. whose internal structure is governed by equations similar, though not necessarily identical, to those of a laminar flame.

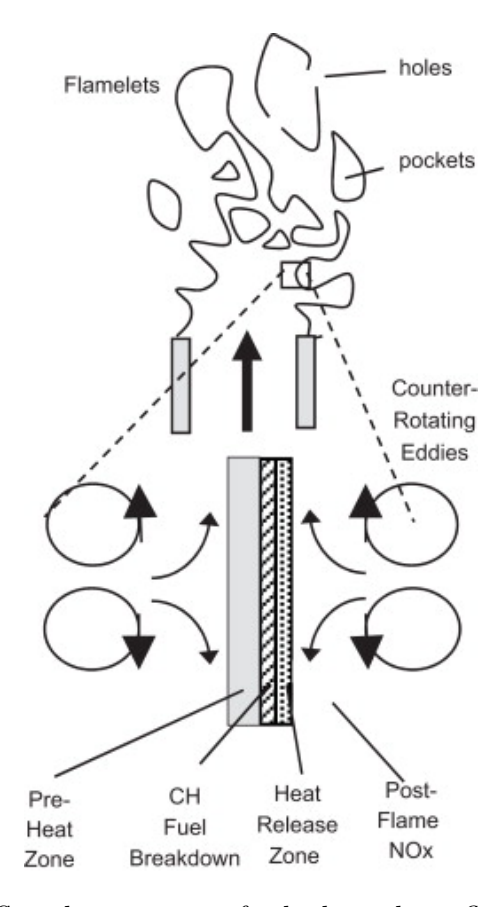


Figure 2.4.: Schematic flamelet structures for hydrocarbons flame. Reprinted from [14]

Figure 2.4 illustrates the schematic structure of turbulent premixed flames of light hydrocarbons with air. A long, nearly continuous flamelet typically encloses the main region of unburned reactants, while additional flamelets often surround smaller regions containing either products or reactants. In the former case, the flame propagates outward, whereas in the latter it propagates inward. Such configurations may also lead to localized flame extinction. The figure further highlights the distinction between the primary reaction zone, delineated by temperature and CH contours, and the post-flame gases, where reactions associated with OH recombination and NO formation occur in a spatially distributed manner.

In addition, Peters emphasized that flame wrinkling retains a form of memory, since the flame geometry at a given location is influenced by distortions generated upstream. Wrinkling arises when turbulent eddies stretch or fold the flame front, and it depends on the complex geometry of shear layers, wall effects, flame–flow interactions, and reference conditions. Depending on turbulence intensity, flamelets may remain continuous and thin, or they may broaden, fragment, and in extreme cases become partially extinguished. Peters defined extreme turbulence as conditions where the turbulent Reynolds number based on the integral length scale is very large ($Re \gg 2800$), or equivalently when the Karlovitz number greatly exceeds unity ($Ka \gg 1$), such that the smallest turbulent eddies penetrate the reaction zone.

The Karlovitz number (Ka) is a dimensionless parameter widely used in combustion literature to characterize flame regimes and identify the dominant turbulence–chemistry interaction mechanisms. It is defined as the ratio between the chemical time scale of the flame $(\tau_F = \alpha/S_L^2)$ and the Kolmogorov time scale of the smallest eddies (τ_{η}) . In this form, it expresses whether the smallest turbulent structures are fast enough to disturb the flame front:

$$Ka = \frac{\tau_F}{\tau_\eta} = \frac{\delta_L^2}{\eta^2} = \frac{(\nu \epsilon)^{1/2}}{S_L^2}$$
 (2.2)

Where the laminar flame thickness is given by Eqn.(2.1), η the Kolmogorov length scale, ν the kinematic viscosity, ϵ the dissipation rate of turbulence kinetic energy. A related parameter is the Damköhler number (Da=1/Ka), which compares the turbulence and the chemical timescales. Together, Da and Ka provide a systematic way to locate the flame regime, with the global relation $Re=Da^2Ka^2$ [22].

In premixed flames, several equivalent definitions of the Karlovitz number were developed. Peters [27] introduced a practical formulation based on turbulence intensity and flame scales:

$$Ka_{\delta} = \left(\frac{u'}{S_L}\right)^{3/2} \left(\frac{\delta_L}{L_T}\right)^{1/2},\tag{2.3}$$

where u' is the root-mean-square velocity fluctuation, δ_L the laminar flame thickness, L_T the integral turbulence length scale. This formulation directly links turbulence properties to the intrinsic laminar flame parameters and is widely used to distinguish between wrinkled flamelet, corrugated flamelet, and distributed-reaction regimes.

Based on the Karlovitz criterion, flame—turbulence interaction can be classified into distinct regimes:

- 1. For Ka < 1, the Kolmogorov length scale η is larger than the flame thickness δ_L . The smallest eddies cannot penetrate the reaction zone, and the flame behaves as a thin laminar flamelet, solely wrinkled or stretched by larger turbulent motions.
- 2. For $Ka \approx 1$, the flame thickness becomes comparable to η . Eddies of this scale begin to interact with the flame front: while the reaction layer retains a laminar-like flamelet structure, the preheat zone is noticeably broadened by turbulent diffusion.
- 3. For $Ka \gg 1$, the smallest eddies penetrate into the flame front, transport becomes strongly turbulence-controlled, and the flame enters the so-called distributed-reaction regime.
- 4. For extreme cases Ka > 100, the flamelet assumption breaks down entirely, as the reaction zone itself is disrupted and classical laminar-based models no longer apply.

This classification highlights how vortices of different scales modify the flame. Large turbulent eddies wrinkle and fold the flame front, thereby increasing its effective surface area, while small eddies determine whether the thin reaction layer remains intact or becomes turbulence-dominated. Since combustion occurs only across this thin layer, the global burning rate scales with the available flame surface. This mechanism supports the flamelet concept, according to which a turbulent flame can be regarded as an ensemble of wrinkled laminar flames. The concept is fundamental in combustion science, forming the basis of many modern models and technologies that aim to reduce fuel consumption and pollutant emissions while ensuring safe and controlled operation of exothermic systems.

Building on this idea, several models have been developed to test and extend Peters' formulation, aiming to relate flame structure and turbulence more quantitatively. As highlighted by Shehab et al. [18], recent work has focused on predicting flame surface

properties, which directly control both the global flame front area and S_T . To make the problem tractable, these models often rely on simplifying assumptions, such as reduced chemical mechanisms, single-valued Lewis numbers, or limited spatial resolution, while statistical approaches are used to capture interactions and the formation of isolated flame pockets.

Further refinements have addressed specific cases. For example, Aspden et al. [32] introduced corrections for hydrogen flames, where $Le \neq 1$ and strong thermal–diffusive effects dominate, while Song, et al. [17] extended these to more general conditions. Other studies concentrated on small-scale turbulence–flame interactions: Gülder [33] showed that Taylor-scale eddies mainly enhance transport without strong wrinkling, whereas Minamoto et al. [18] found that such eddies can still increase front corrugation and lead to higher burning velocity. Kulkarni and Bisetti [34, 35] analyzed flame surface morphology and brush thickness, proposing scaling laws that highlight the importance of small-scale structures.

Finally, Driscoll [14, 29] developed a widely adopted framework to clarify the range of turbulence intensities over which different models are valid. His studies on light hydrocarbons (methane, propane) emphasized the role of the integral length scale L_T and the velocity fluctuations u' in defining the dominant interaction regime, especially when $Le \simeq 1$.

2.2. Existing correlation between the burning speed and the flame structure

In this section, the main developments in combustion science concerning the relation between turbulence, burning velocity, and flame structure are discussed. Before addressing the correlations in detail, several fundamental parameters must be introduced.

The first is the flame surface density (FSD), denoted as Σ , which represents the flame surface area per unit volume. Originally introduced in the Bray–Moss–Libby (BML [19]) model described in the Appendix A.1, it is a statistical quantity that characterizes the wrinkling of the flame front induced by turbulence. A higher value of Σ corresponds to a larger effective flame area, which in turn increases the turbulent flame speed.

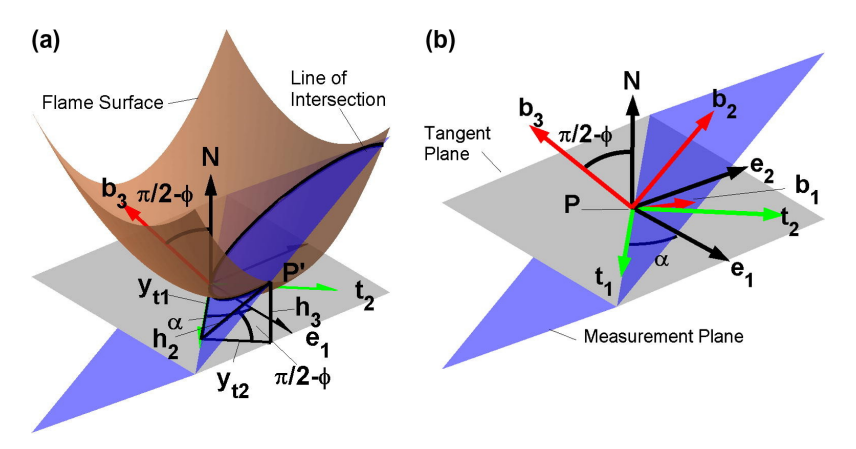


Figure 2.5.: Estimation of the flame surface density (FSD) in three-dimensional space. Reprinted from [36].

Figure 2.5 schematically illustrates the relationship presented by Hawkes et al. [36] between two-dimensional measurements and the true three-dimensional quantities appearing in the

flame surface density (FSD) transport equation. Specifically, the figure displays how strain rate, curvature, and displacement speed can be estimated in a three-dimensional turbulent premixed flame from planar data, under the assumption of isotropic turbulence and scalar fields. Shepherd [36] derived explicit scaling factors or transformation relationships that allow each two-dimensional measurement to be projected or corrected into its three-dimensional counterpart.

A second parameter is the stretch factor I_0 , also known as the Bray-Cant factor. This was introduced by Bray and Cant) [37] as an extension of the BML framework to account for deviations from the Damköhler prediction of the speed–area relation. I_0 depends on the local strain rate, flame curvature, and diffusive-thermal effects, and has therefore not a universal value. The flame strain rate and curvature can be related by defining the stretch rate, as done in [18]. Under weak diffusive-thermal effects, $I_0 \approx 1$, while in general conditions $I_0 \neq 1$. Its derivation is further discussed in the Appendix A.2.

The physical foundation of I_0 is provided by the Markstein number Ma, which establishes a direct link between flame geometry (curvature and strain) and deviations from the predicted speed–area relation. The Markstein number quantifies the sensitivity of the laminar burning velocity to flame stretch. Originally introduced by Markstein in [38], this dimensionless number describes how local heat release modifies the flame topology under curvature or strain. Two forms are generally distinguished: the curvature Markstein number and the flow-strain Markstein number, both defined as a ratio between a characteristic Markstein length and the laminar flame thickness δ_L . A larger Markstein number indicates a stronger influence of local stretch on the flame speed. The formulation of the two related numbers is in the Appendix A.3.

The turbulent burning velocity, S_T , is not uniquely defined in the literature. Instead, several complementary formulations are employed, depending on whether the focus is on global fuel consumption, flame surface wrinkling, or the kinematic displacement of the flame front. The most widely cited definitions are given in Driscoll [14, 29]:

1. Global consumption speed $(S_{T,GC})$.

$$S_{T,GC} = \frac{\dot{m}_R}{\rho_u A_{\bar{c}=0.5}} \tag{2.4}$$

where \dot{m}_R is the global reactant consumption rate, ρ_u is the density of the unburnt mixture, and $A_{\overline{c}=0.5}$ is the projected area of the flame brush defined by the iso-surface at a progressive variable equal to $\overline{c} = 0.5$ [29]. The progressive variable is defined in the paragraph 2.2.4. This definition provides a macroscopic measure of flame propagation, but is sensitive to both the choice of the reference area and the influence of large-scale turbulence.

2. Local consumption speed $(S_{T,LC})$.

$$S_{T,LC} = S_L I_0 \int_{-\infty}^{+\infty} \Sigma \, d\eta_F \tag{2.5}$$

where $S_{L,0}$ is the unstretched laminar burning velocity, I_0 is the Bray-Cant stretch factor, Σ is the flame surface density (surface area per unit volume), and η_F is the coordinate normal to the mean flame brush. The flame brush is defined as the region occupied by the fluctuating turbulent flame front. This formulation emphasizes the local flame structure: the integrated wrinkling of flamelets, expressed as $\int \Sigma d\eta$, governs the effective propagation velocity. It is frequently used in modeling since it connects S_T directly to FSD transport equations, though it requires assumptions on the local definition of the flame front.

3. Local displacement speed $(S_{T,LD})$.

$$S_{T,LD} = (\mathbf{V}_{\text{Flame}} - \mathbf{V}_{\text{Gas}})_{LE} \cdot \mathbf{n}_{LE}$$
 (2.6)

where $\mathbf{V}_{\mathrm{Flame}}$ is the velocity of a chosen flame iso-surface, $\mathbf{V}_{\mathrm{Gas}}$ the local gas velocity, and \mathbf{n}_{LE} the unit normal to the flame front at the leading edge. This kinematic definition represents the relative velocity of the flame front with respect to the flow. In the absence of stretch and heat losses, $S_{T,LD}$ tends to coincide with S_L . Since thermal expansion can artificially increase this quantity, a density-weighted correction is often introduced:

$$S_{T,LD}^* = \frac{\rho}{\rho_u} S_{T,LD}. \tag{2.7}$$

Song, al. [17] demonstrated that the PDF of the local displacement rate over the laminar one is often close to unity, to confirm that locally the flamelet structures are composed of more laminar flames. Additionally they pointed out that these three formulations 2.4, 2.5 and 2.6 are not equivalent but instead capture different aspects of turbulent flame propagation: $S_{T,GC}$ reflects global fuel consumption, but is highly dependent on turbulence intensity and geometry; $S_{T,LC}$ emphasizes the flame surface structure, connecting directly to FSD-based modeling frameworks; $S_{T,LD}$ provides a local kinematic measure, but requires density correction to avoid overestimating the true burning rate.

For hydrogen flames [17], these differences become particularly relevant due to the strong thermal-diffusive effects ($Le \neq 1$). In lean H₂-air flames, Song et al. observed a partial decorrelation between fuel consumption rate and heat release rate, meaning that global measures such as $S_{T,GC}$ may misrepresent actual propagation unless preferential diffusion is properly accounted for. This underlines the importance of carefully selecting the definition of S_T depending on the modeling framework and fuel chemistry.

The correlations for the *flamelet* and *distributed-reaction* regimes are presented in this section. The transition between the two regimes is indicated by the bend in Figure 2.6.

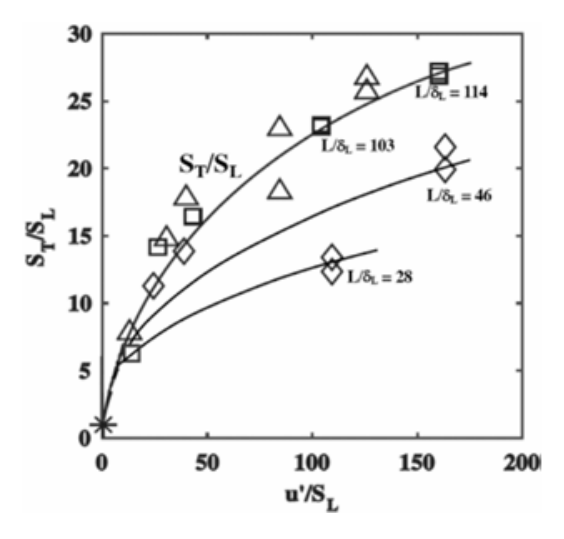


Figure 2.6.: Turbulent burning velocity over laminar burning velocity plotted against the root-mean-square of flow velocity fluctuations in extreme turbulence [29]

Figure 2.6 shows the variation of turbulent burning velocity with turbulence intensity, both normalized by the laminar burning velocity. At low turbulence levels, $S_T = S_L$. As turbulence increases, S_T grows almost linearly with u'/S_L , consistent with the expectation that burning speed scales with flame surface area. Beyond a critical value of u'/S_L , however, the curve bends, indicating that the growth of S_T becomes quadratic. At this stage, flame

geometry alone is no longer sufficient to predict burning velocity. While the flame surface saturates, S_T continues to rise due to enhanced turbulent diffusion.

2.2.1. Flamelet Regime

In the flamelet regime, the relation between flame surface area and burning velocity follows the Damköhler hypothesis. A first compact and empirical formulation, derived from Damköhler and Shchelkin [22], is:

$$\frac{S_T}{S_L} = \left(1 + c_1 \left(\frac{u'}{S_L}\right)^2\right)^{1/2},$$
 (2.8)

where c_1 is often referred to the progressive parameter.

A more general formulation was developed by Bray and Cant [37] within the BML framework for the conservation of the density function:

$$\frac{S_T}{S_L} = I_0 \int_{-\infty}^{+\infty} \Sigma d\eta, \tag{2.9}$$

where Σ is the flame surface density, η is the coordinate normal to the flame brush, and I_0 the Bray-Cant stretch factor. The detailed derivation is in the Appendix A.2. The integral is proportional to the product of the maximum Σ (occurring near $\bar{c} = 0.5$) and the brush thickness δ_T . Figure 2.7 displays the iso-surface identified within the flame brush that represents the advancement of the not-wrinkled surface. Building on this relation,

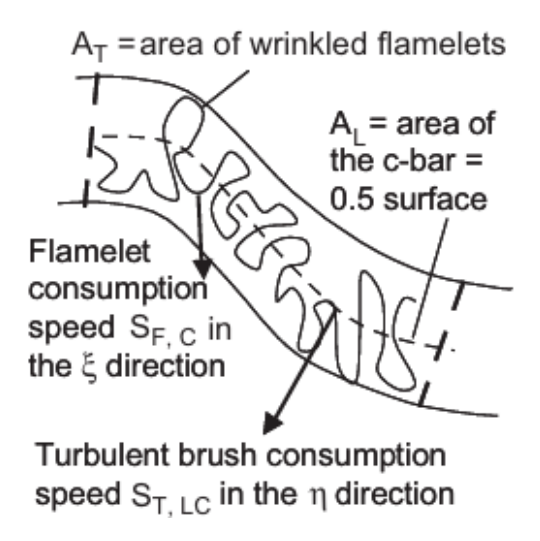


Figure 2.7.: Schematic of the wrinkled flame area (A_T) compared to the $\bar{c} = 0.5$ iso-surface area (A_L) . Also shown are the flamelet consumption speed $(S_{F,C})$ and turbulent brush local consumption speed $(S_{T,LC})$. Reprinted from [14]

further corrections have been introduced to account for turbulence intensity, integral scale, and diffusive-thermal effects. However, at higher turbulence intensities these corrections are insufficient, as stretching and bending of the flame surface become dominant, leading to higher S_T than predicted purely by area scaling.

2.2.2. Distributed-Reaction Regime

When turbulence intensity enters the distributed-reaction regime, S_T is no longer determined primarily by flame surface area but by turbulent diffusion. In this regime, the preheat zone

broadens and the burning velocity accelerates according to:

$$\frac{S_T}{S_L} = \left(\frac{D_{\text{eff}}}{D}\right)^{1/2} = \left(1 + c_2 \frac{u' L_T}{\nu}\right)^{1/2},\tag{2.10}$$

where $D_{\text{eff}} = D + D_t$ is the effective diffusivity, with D the molecular diffusion coefficient and D_t the turbulent diffusivity.

A key observation is that turbulence-induced broadening is generally stronger in the preheat zone than in the reaction zone. The latter is governed primarily by chemical kinetics, whereas the preheat layer is diffusion-dominated and therefore more sensitive to turbulent transport. In practice, the increase of the effective diffusivity $D_{\rm eff}$ enhances heat and mass transport across the front, leading to additional wrinkling and an increase in the local burning velocity of flame segments. This explains why turbulent flames often propagate faster than predicted purely from surface area considerations: enhanced diffusivity increases burning velocity even when the global flame surface approaches saturation.

2.2.3. The Borghi-Williams Diagram

In the combustion literature, several diagrams have been proposed to classify flame structures and to analyze how turbulence modifies flame behavior. Among the most widely used are the *Williams diagram* and the *Borqhi diagram*.

The Williams diagram, which applies to both premixed and diffusion flames, is constructed using the Reynolds number and the Damköhler number defined on the flame thickness scale:

$$Re_{\delta} = \left(\frac{u'}{S_L}\right) \left(\frac{L_T}{\delta_L}\right),$$
 (2.11)

$$Da_{\delta} = \left(\frac{u'}{S_L}\right)^{-1} \left(\frac{L_T}{\delta_L}\right),\tag{2.12}$$

where u' is the rms turbulent velocity fluctuation, L_T the integral turbulence length scale, δ the characteristic flame thickness, and S_L the laminar burning velocity.

The Borghi–Peters diagram, instead, is tailored to premixed flames. It normalizes turbulence parameters by the intrinsic flame properties, plotting the velocity ratio u'/S_L on the vertical axis against the scale ratio L_T/δ_L on the horizontal axis, as shown in Figure 2.8. This representation allows different combustion regimes to be identified within a single framework.

Three main zones are distinguished:

- 1. Laminar flamelet regime: chemical kinetics remain fast and turbulent eddies are unable to penetrate the inner flame structure. Combustion proceeds in thin laminar flamelets, wrinkled and stretched by turbulence. This regime is often subdivided into wrinkled flamelets $(u' < S_L)$ and corrugated flamelets $(u' > S_L)$.
- 2. Thin flames and distributed reaction regime: smaller eddies become comparable to or smaller than the flame thickness, allowing them to disturb the flame structure. As turbulence intensifies, burning takes place in thickened flames, and ultimately distributed reaction zones form when eddies penetrate the inner reaction layer.
- 3. Broken reaction zones: at the highest turbulence intensities, mixing is much faster than chemistry, so the reaction zone is disrupted and stable flames cannot exist.

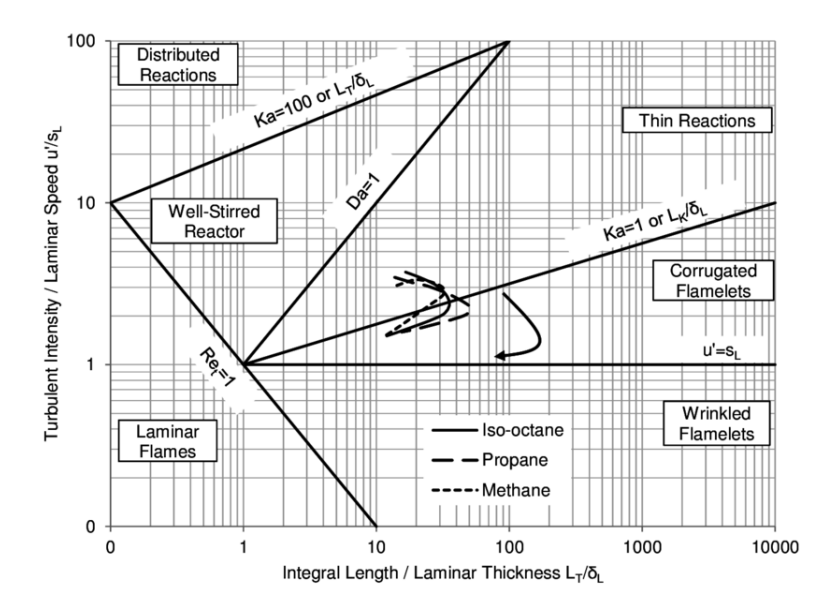


Figure 2.8.: Borghi diagram adapted from [39].

These two schematics illustrate the different premixed flame regimes [16]. In Figure 2.9 on the top, the distinction is made between wrinkled flamelets and corrugated flamelets, which both belong to the laminar flamelet regime. In the wrinkled flamelet case, chemical kinetics are fast enough that turbulent eddies cannot penetrate the inner flame structure. The reaction zone remains thin and intact, while turbulence only wrinkles the preheat layer. This condition occurs when the Karlovitz number is below unity, and the turbulence intensity is weaker than the laminar burning velocity. In the corrugated flamelet case, turbulence is stronger, with velocity fluctuations exceeding the laminar flame speed. As a result, the flame surface becomes highly corrugated and distorted by vortical motions, but the reaction zone itself remains thin and governed by kinetics.

Figure 2.9 on the bottom shows the transition to regimes where turbulence begins to interact with the internal flame structure. When the Karlovitz number exceeds unity, small-scale eddies can penetrate into the preheat layer, broadening the flame brush while the thin reaction zone remains primarily controlled by chemistry. This corresponds to the so-called thin reaction zone regime. At even higher turbulence intensities, when $Ka_{\delta} > 1$, vortices penetrate the reaction layer itself, fragmenting the flame front. In this broken reaction zone regime, turbulent mixing occurs on faster timescales than chemical kinetics, leading to the disruption of the reaction zone into small disconnected flame structures, with local quenching and extinction becoming possible.

Overall, Figure 2.9 provides a clear visualization of how increasing turbulence progressively alters the balance between transport and chemistry: from simple wrinkling of a thin laminar sheet, to broadening of the preheat zone, and ultimately to the complete breakdown of the reaction zone.

2.2.4. The progressive parameter

A fundamental quantity in the Bray–Moss–Libby (BML) model is the *progress variable*, which describes the state of the reaction and its spatial evolution. If the thin–reaction–layer assumption holds, it can be defined using temperature as

$$c(\mathbf{x},t) = \frac{T(\mathbf{x},t) - T_u}{T_b - T_u},\tag{2.13}$$

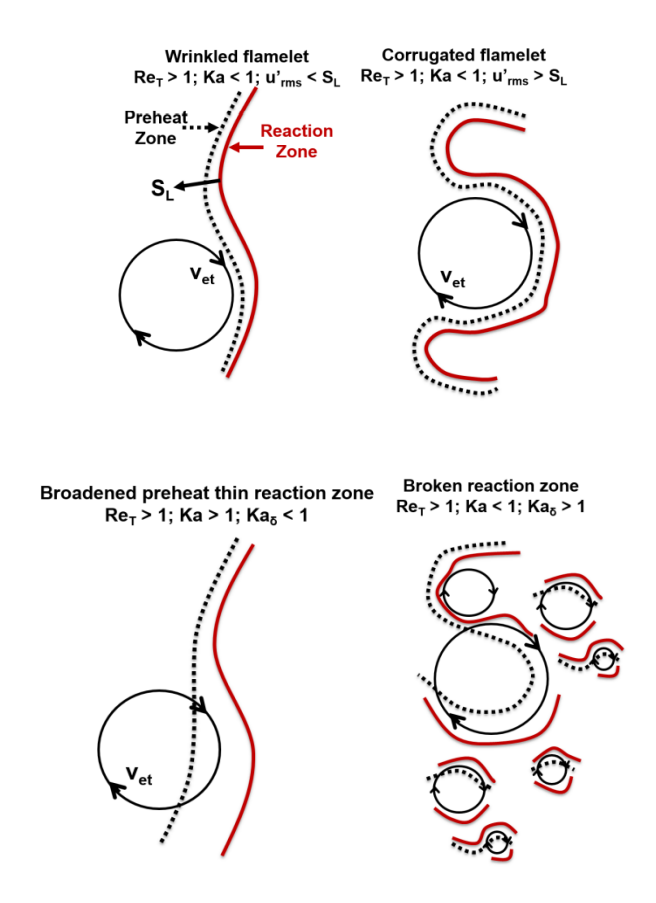


Figure 2.9.: Schematic illustration of premixed flame regimes [16]. The panel on the top shows the distinction between wrinkled and corrugated flamelets, while the one on the bottom illustrates the transition to thin and broken reaction zones.

with T_u and T_b the unburnt and burnt gas temperatures, respectively. In an idealized formulation, c acts as an indicator function:

$$c(\mathbf{x},t) = \begin{cases} 1, & \mathbf{x} \in b(t), \\ 0, & \mathbf{x} \in u(t), \end{cases}$$
 (2.14)

where b(t) and u(t) denote burnt and unburnt regions. Although temperature is commonly used, any monotonic scalar (e.g. a reactant mass fraction) can serve as a definition of c.

In turbulent premixed flames, the flame is broadened into a flame brush, where the thinlayer assumption is not strictly valid. In this case, the mean progress variable $\bar{c}(\eta_F)$, with η the coordinate normal to the brush, provides a convenient way to parameterize the flame structure. In fact, the flame surface density is most often expressed directly as a function of \bar{c} as reported in [14]. Figure 2.10 shows experimental evidence of this correlation in Bunsen flames.

A widely used parametrization of the FSD across the flame brush is

$$\Sigma(\eta_F) = 4 \Sigma_{\text{max}} \bar{c}(\eta_F) (1 - \bar{c}(\eta_F)), \tag{2.15}$$

where Σ_{max} is the peak FSD located at the brush center, i.e. $\bar{c} = 0.5$. The mean progress-variable profile is often approximated by a logistic function,

$$\bar{c}(\eta_F) = \left[1 + \exp\left(\frac{-4(\eta_F - \eta_{F,m})}{\delta_T}\right)\right]^{-1}, \qquad (2.16)$$

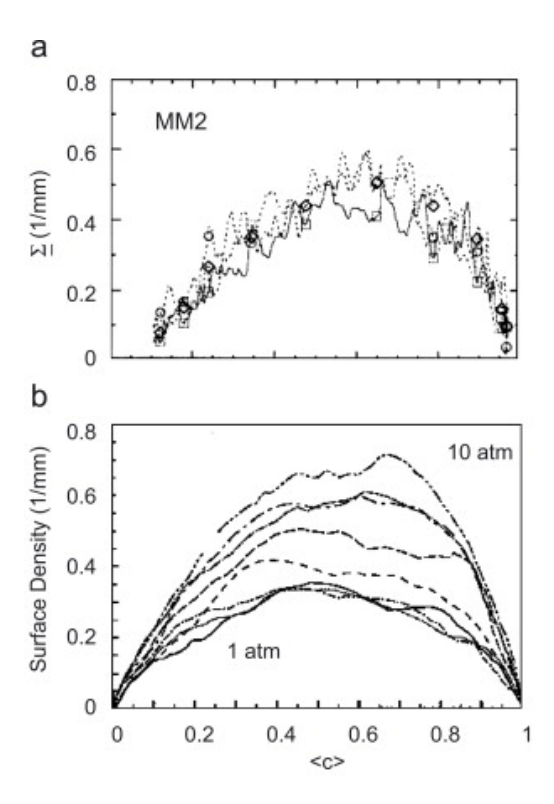


Figure 2.10.: Flame surface density measured in Bunsen flames, plotted against the mean progress variable. Reprinted from [14].

with $\eta_{F,m}$ the position of $\bar{c} = 0.5$ and δ_T the flame brush thickness, defined as the mean distance between the 5% and 95% iso-surfaces of the progress variable \bar{c} . It provides a statistical measure of the average flame thickness under turbulent conditions, in contrast to the laminar flame thickness δ_L .

Inserting Eqs. (2.15)–(2.16) into the equation 2.5 becomes:

$$S_{T,LC} = S_{L,0}I_0 \int_{-\infty}^{+\infty} \Sigma \, d\eta = S_{L,0}I_0 \, \Sigma_{\max} \, \delta_T,$$
 (2.17)

which shows that the product $\Sigma_{\text{max}} \delta_T$ controls the turbulent burning velocity. Equivalently,

$$\Sigma_{\text{max}} = \frac{1}{\delta_T} \frac{A_T}{A_L}, \tag{2.18}$$

where A_T is the wrinkled flame surface and A_L the reference laminar surface.

In practice, the progress variable also serves to identify the flame front within the brush. A common convention [14, 20] is to use the iso-surface $\bar{c} = 0.5$, which best represents the mean flame location in the absence of fluid motion.

2.3. Comparison with the ignition behavior of iron particles in HIT

In summary the previous section shows that, although many studies have shown that existing formulations can reliably capture the influence of turbulence on the structure of premixed flame of both hydrocarbon and hydrogen across a broad range of turbulent intensities, they are not yet universally valid throughout the entire turbulent energy spectrum. Their applicability is strongly affected by additional factors that must be considered, such as

preferential diffusion (Lewis number effects), flame stretch and curvature (Markstein number dependence), heat losses, and differential transport of species. These aspects can significantly alter the local flame structure and, consequently, the predictive accuracy of turbulence–flame interaction models. Based on this observation, the present work aims to identify correlations suitable for the case of iron-particle cloud combustion under homogeneous isotropic turbulence (HIT), as studied through numerical simulation.

Before introducing the adopted methodology, it is important to highlight the main assumptions and differences between the combustion of iron particles clouds and the discussed premixed-flame configurations.

The first fundamental difference lies in the reaction mechanism. In hydrocarbon [14] or hydrogen [17] premixed flames, combustion occurs through homogeneous gas-phase reactions, since both fuel and oxidizer are gaseous. Even in liquid-hydrogen injection studies, evaporation is assumed fast enough for the fuel to participate in the gas phase before reaction. In contrast, iron-particle combustion is governed by heterogeneous kinetics. Oxygen diffuses to the particle surface, oxidizing the solid core and forming a liquid FeO shell that subsequently solidifies. The overall process is therefore controlled by the combined effects of surface chemistry, diffusion through the oxide layer, and phase-change phenomena such as melting and solidification. While the flamelet concept in premixed combustion is characterized by a thin chemical reaction zone embedded in a diffusive preheat layer, in iron combustion the effective reaction zone is confined to the particle surface, and its structure depends on the evolving core–shell dynamics rather than on purely gaseous chemistry.

A second distinction concerns the initial conditions. In premixed flames, fuel and oxidizer are already mixed at the molecular level, forming a single gaseous mixture characterized by a uniform pressure, temperature, and composition (defined by the equivalence ratio). This mixture is initially either quiescent or subjected to a prescribed flow field, so that both fuel and oxidizer share the same thermodynamic and kinematic state. In iron-particle combustion, by contrast, the system is inherently two-phase: solid particles are initially at rest and at ambient temperature, while the oxidizer may be in motion, either laminar or turbulent. The particle velocity is induced by gas drag which is improved by the chemical reaction. As a result, slip velocity between particles and gas develops, and the thermodynamic state of the particles (involving heating, melting, and oxidation) differs from that of the surrounding oxidizer, making the initial configuration more complex than in premixed flames.

A further implication of the two-phase nature of iron-particle combustion is the presence of this particle–fluid slip velocity. In premixed flames, fuel and oxidizer form a single gaseous mixture and are convected together, so no relative motion exists between the reactive species. In contrast, in particle clouds the finite particle inertia leads to different trajectories of particles and fluid. This decoupling strongly influences ignition and flame propagation. DNS [40] further shows that particles with higher Stokes number exhibit larger inertia and therefore higher slip velocity relative to the fluid. This enhances the convective transport of heat from dense particle clusters to surrounding regions of lower particle number density: fluid streams can flow through hot clusters, acquire thermal energy, and carry it downstream, where it preheats and eventually ignites other particles. This mechanism demonstrates that slip velocity not only affects local particle heating but also contributes to the non-local redistribution of heat, thereby reducing the global ignition delay.

A further aspect involves the Lewis number. In hydrogen flames, conditions with Le < 1 are often studied [17], while for hydrocarbon premixed flames, the case Le = 1 is often assumed, as discussed by Driscoll in [14]. In the case of iron particles flame, the combustion is modeled analogously with Le = 1 as initial assumption, which simplifies the analysis by

assuming equal thermal and mass diffusivities. However it should be noted that it depends on the specification of the Prandtl and Schmidt numbers, and may lose validity under high turbulence, where turbulent diffusivity becomes the dominant transport mechanism.

In the presence of solid particles, the coupling between turbulence and reaction is qualitatively different. Under homogeneous isotropic turbulence (HIT), inertial particles exhibit preferential concentration and form clusters—most pronounced for Stokes numbers around unity $(St \approx 1)$ —so combustion proceeds predominantly within these aggregates. By contrast, in gaseous premixed flames the fuel and oxidizer are co-advected as a single mixture, and turbulence enhances their mixing; it wrinkles and stretches the flame front but does not create separate fuel-rich and oxidizer-rich streams. For descriptive clarity, one may still refer to a reaction layer and a surrounding preheat-like region; however, the underlying physics is distinct: in iron-particle combustion the reaction layer is confined to the particle surface, while the gas in and around clusters is modified by particle heat release and oxygen consumption, producing hot, oxygen-depleted pockets that condition neighboring particles. Direct numerical simulations [40] indicate that clustered particles ignite first and generate hot fluid streaks that are convected into more dilute regions, thereby shortening ignition delays; this behavior is best regarded as an analogy to a preheat zone rather than a structural equivalence to premixed flamelets.

As in premixed flames, turbulence enhances the effective diffusivity of heat and species in the gas, which increases mixing efficiency and broadens the preheat zone. This broadening effect accelerates ignition by raising the local burning velocity of flame segments. In premixed systems, however, extinction may occur when turbulence directly interferes with the reaction layer [14]: either through excessive straining of the flame front, which prevents the balance between heat release and diffusion, or when very small vortices penetrate the chemical zone in the thin- or distributed-reaction-zone regimes. In both cases the local flame structure is destroyed and the reaction quenches. In contrast, for iron-particle combustion the reaction layer remains confined to the particle surface and is essentially governed by surface kinetics and mass transfer, so turbulence primarily modifies the preheat zone while leaving the reaction layer largely unaffected. DNS [40] results further indicate that extinction in the classical premixed sense does not occur; instead, local suppression of combustion may arise from oxygen depletion around clusters or from excessive radiative and convective heat losses, which prevent sustained ignition of some particles.

Finally, radiative heat transfer adds another layer of complexity. Hot clusters emit thermal radiation that preheats distant particles, creating a non-local ignition mechanism absent in gaseous premixed systems. Together, clustering, convective transport, and radiation govern the ignition dynamics and global flame propagation of iron-particle clouds.

These differences imply that flame surface density (FSD) models, which successfully capture turbulence—flame interactions in gaseous premixed combustion, cannot be directly applied to heterogeneous iron flames. Instead, new correlations are required that explicitly account for particle-scale dynamics, clustering effects, and radiative transfer when modeling turbulent iron-particle combustion under homogeneous isotropic turbulence.

3. Methodology

This chapter introduces the model used to simulate the combustion of an iron particle cloud, with a more detailed description available in [40, 41]. The simulation setup adopted in this work is then described, together with the procedure developed to detect the flame front in post-processing. Although the detection tool was tested on the present configuration, it is designed to be applied in other scenarios as well.

Additionally the calculations executed to compute flame characteristic quantities as position, area and speed are reported. It must be noted that these calculations are based on one-dimensional propagative flames and thus adaptions are necessary when considering other flame setups.

3.1. Description of the model

The model adopted for simulating the combustion of an iron particle cloud is based on an Euler–Lagrange carrier-phase direct numerical simulation (*CP-DNS*) approach with a point-particle approximation [40]. In this framework, the behavior of a large number of particles is reduced to the solution of ordinary differential equations (ODEs). The *CP-DNS* [41] method couples an Eulerian description of the carrier-phase flow with a Lagrangian approach of the dispersed particles and is widely used for multiphase flows.

After initial ignition, the combustion of the particles proceeds in a homogeneous isotropic turbulent (HIT) flow of air. Since the fluid and the particles are at different velocities and temperatures, the exchange of heat, mass, and momentum is resolved through a two-way coupling: interpolation from the fluid to the particles and spreading from particles back to the fluid. Because the ratio of iron particle density to gas density is greater than 10⁴, the zero-dimensional (point-particle) assumption is justified.

This model relies on the hypothesis that the pressure is homogeneous in the space at each instant of time, low fluid Mach number, and the pressure oscillations due to momentum changes are much smaller than the thermodynamic pressure. Consequently:

$$p(\mathbf{x},t) = p_0(t) + \pi(\mathbf{x},t) \simeq p_0(t) \tag{3.1}$$

Here $p_0(t)$ is the thermodynamic pressure and $\pi(\mathbf{x}, t)$ denotes the fluid momentum-induced pressure oscillations, which are negligible with respect to the thermodynamic term.

3.1.1. Fluid phase model

The continuous fluid phase is composed by air flow, that is, an ideal gas mixture of oxygen and nitrogen in the characteristic molar fraction, O_2 at 23% and nitrogen N_2 at 77%. The molar fraction of oxygen in the fluid is a function of space and time $(Y_{O_2}(\vec{x},t))$ The ideal equation of state is used:

$$p_0 = \rho(\vec{x}, t) R_M T(\vec{x}, t) \tag{3.2}$$

where the gas constant $R_M(\vec{x},t) = Y_{\rm O_2}R_{\rm O_2} + Y_{\rm N_2}R_{\rm N_2}$ with $Y_{\rm O_2}(\vec{x},t)$ and $Y_{\rm N_2}(\vec{x},t)$ the local mass fraction. The governing equations are the conservation of mass, oxygen mass fraction, momentum, and enthalpy. Including the source terms from particle coupling, they read:

$$\frac{\partial \rho}{\partial t} + \frac{\partial (\rho u_i)}{\partial x_i} = S_{O_2},\tag{3.3a}$$

$$\frac{\partial(\rho Y_{O_2})}{\partial t} + \frac{\partial(\rho u_i Y_{O_2})}{\partial x_i} = \frac{\partial}{\partial x_i} \left(\rho D_{O_2} \frac{\partial Y_{O_2}}{\partial x_i}\right) + S_{O_2},\tag{3.3b}$$

$$\frac{\partial(\rho u_i)}{\partial t} + \frac{\partial(\rho u_i u_j)}{\partial x_j} = -\frac{\partial \pi}{\partial x_i} + \frac{\partial \tau_{ij}}{\partial x_j} + S_{i,u} + f_i, \tag{3.3c}$$

$$\frac{\partial H}{\partial t} + \frac{\partial (u_i H)}{\partial x_i} = \frac{\partial}{\partial x_i} \left(\lambda \frac{\partial T}{\partial x_i} \right) + \frac{dp_0}{dt} + S_H. \tag{3.3d}$$

where $u_i(\mathbf{x},t)$ denote the Cartesian components of the velocity of the fluid, with repeated indices implying summation. The quantity $H(\mathbf{x},t)$ represents the volumetric enthalpy, expressed in units of J m⁻³. The external forcing term $f_i(\vec{x},t)$ injects energy into the large-scale motions of the flow, thereby compensating for small-scale dissipation and maintaining a statistically steady turbulent state. Since a two-way coupling mass, momentum and heat transfer is used, the particles influence on the fluid is represented by means of the source terms of mass S_{O_2} , momentum $S_{i,u}$ and enthalpy S_H . The term τ_{ij} is the stress tensor. The equations are solved on a periodic domain using a Fourier pseudo-spectral method, with linear terms advanced in Fourier space, nonlinear terms computed in physical space, and time integration carried out with a second-order Runge-Kutta scheme. Further formulations of these terms are in the Appendix B.

3.1.2. Particle phase

Combustion occurs at the particle surface. As the Fe core reacts with oxygen, it shrinks and an FeO shell develops and grows inward. The process is modeled using a first-order surface kinetics (FOSK) model [42], which assumes a single-step oxidation:

$$Fe + \frac{1}{2}O_2 \longrightarrow FeO$$
 (3.4)

This choice is consistent with experimental evidence showing FeO as the primary oxidation product. While higher oxides (Fe₃O₄, Fe₂O₃) may form at later stages, previous studies [41] demonstrated that limiting the kinetics to FeO provides better agreement with experiments under turbulent conditions.

Several experiments on single iron particles have been carried out to investigate their combustion behavior and to analyze the resulting oxidation products [43, 44]. These studies indicate that oxygen is transported to the particle surface through Stefan flow, where it reacts with the metallic core. The particle develops a layered structure, consisting of a shrinking Fe core surrounded by an FeO shell. Further oxidation may proceed through the sequence FeO \longrightarrow Fe₃O₄ \longrightarrow Fe₂O₃. However, in the present work only the first step of oxidation to FeO is considered.

The thermodynamic properties inside each particle are assumed spatially uniform, justified by the low Biot number. The Biot number is a dimensionless quantity used in heat transfer that compares the internal thermal resistance of a solid to the external convective thermal resistance at its surface. Values lower than Bi < 0.1 indicates that conduction resistance

within the body is negligible, allowing for a nearly uniform temperature distribution. Both melting and solidification plateaus are accounted for.

The governing equations for particle mass, iron mass, enthalpy and momentum in the dispersed particles phase are:

$$\frac{dm_p}{dt} = \rho_f Y_{O_2} \big|_{\vec{x}_p} A_d k_d D a^*, \tag{3.5a}$$

$$\frac{dm_{p,\text{Fe}}}{dt} = -\frac{1}{s} \frac{dm_p}{dt},\tag{3.5b}$$

$$\frac{dH_p}{dt} = \dot{Q}_{\text{conv}} + \dot{Q}_{\text{rad}} + \dot{Q}_{dm_p/dt}, \tag{3.5c}$$

$$\frac{du_{i,p}}{dt} = \frac{F_{i,\text{drag}} + F_{i,dm_p/dt}}{m_p}.$$
(3.5d)

where $\dot{Q}_{\rm conv} = -k_c A_p (T_p - T | \mathbf{x}_p)$ is the convective heat flux, $\dot{Q}_{\rm rad} = -\epsilon_{rad} \sigma A_P T_p^4$ is the radiative heat loss, $\dot{Q}_{dm_p/dt} = \frac{dm_p}{dt} h_{\rm O_2}(T_p)$ is the enthalpy flux associated to the oxygen mass flow. It might be useful to underline the role of the Damköhler number. Generally, it is defined as the ratio between the characteristic time of the reaction over the residence time of the particle in the fluid. In the continuity equation 3.5a the normalized form Da^* is considered to limit the kinetics in the case of low particles temperature.

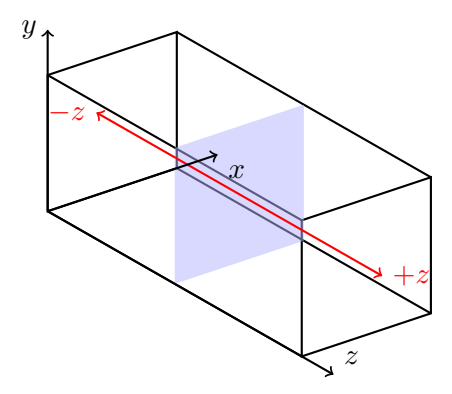
$$Da^* = \frac{A_r k_r}{A_r k_r + A_d k_d} \tag{3.6}$$

Where $k_r = k_{\infty} exp(-T_a/T)$ is the Arrhenius kinetic constant while $k_d = Sh^*D_{O_2,f}/d_p$ is the diffusive transfer coefficient that follows the Sherwood correlation specified in the Appendix B.

3.2. Simulation setup: one-dimensional homogeneous propagating flame

In this section, the simulation setup is presented. As a first step, only a one-dimensional homogeneous flame is considered in order to study the interaction between flame structure and turbulent flow in a simplified framework. This setup allows to track the progressive development of the flame in the initial absence of fluid motion and, therefore, to verify the correctness of the adopted method.

A sketch of the simulations domain is shown. The computational domain measures 0.02 m along the x-axis, 0.02 m along the y-axis, and 0.04 m along the z-axis. The boundaries are periodic in all directions. At the beginning of the simulation, a central x-y plane (at $z = L_z/2$) is heated for 4 ms, activating the oxidation reaction. The flame then propagates in both the positive and negative z-directions until it reaches the ends of the domain.



The number of particles inside the domain is set such that a prescribed equivalence ratio Φ is achieved by the end of the simulation. The equivalence ratio is defined as the fuel-air mass ratio in the unburnt mixture normalized by the stoichiometric value:

$$N_{part} = \Phi \frac{m_{O_2}}{m_p} \frac{1}{s} \tag{3.7}$$

where m_p is the single-particle mass, m_{O_2} the mass of oxygen in the fluid and s the stoichiometric ratio.

The particle and oxygen masses are computed as:

$$m_p = \frac{4}{3}\pi\rho_{Fe} \left(\frac{d_p}{2}\right)^3,\tag{3.8a}$$

$$m_{O_2} = \rho Y_{O_2} L_x L_y L_z,$$
 (3.8b)
 $H = \rho_{O_2} h_{O_2},$ (3.8c)

$$H = \rho_{O_2} h_{O_2},$$
 (3.8c)

where d_p the particles initial diameter, ρ_{Fe} the iron density, Y_{O_2} the oxygen molar fraction in the fluid, ρ_{O_2} is the oxygen partial density in the fluid and h_{O_2} is the oxygen specific enthalpy, obtained from NASA polynomial fits as a function of T and p [40].

These quantities, together with the initial conditions for the fluid, are listed in Table 3.1.

Table 3.1.: Initial conditions for particles and fluid, the subscript ⁰ stands for initial.

Parameter	Value	Parameter	Value
d_p^0	$1\times 10^{-5}\mathrm{m}$	p_0	1 bar
\hat{T}_{p}^{0}	$500\mathrm{K}$	$Y_{O_2}^0$	0.23
T_f^0	$500\mathrm{K}$	$ ho_{Fe,0}$	$7801 kg m^{-3}$

The turbulence intensity of the fluid phase is prescribed through the mean dissipation rate ϵ , defined as

$$\epsilon = \frac{1}{\langle \rho \rangle} \langle \frac{\partial u_i}{\partial x_i} \tau_{ij} \rangle \tag{3.9}$$

The computation of the dissipation is computed on the dimensionless Stokes number, defined as the ratio of the particle inertia timescale $\tau_p = m_p/(3\pi\mu d_p)$ to the fluid characteristic timescale τ_f . In turbulent flow, τ_f is close to the Kolmogorov timescale $\tau_{\eta} = \sqrt{\langle \nu \rangle / \epsilon}$, where $\langle \nu \rangle$ is the average kinematic viscosity. Hence,

$$St = \frac{m_p}{3\pi\mu d_p} \sqrt{\frac{\epsilon}{\langle \nu \rangle}}.$$
 (3.10)

The properties used are calculated at the initial conditions reported. In the laminar case, no input forcing is set, as no turbulent motion is imposed.

To illustrate the evolution of the system, instantaneous z-y slices of the simulation domain are reported in Figures 3.1, 3.2. Each visualization is organized in four panels that provide complementary information on both the thermal–chemical and fluid-dynamic state of the system. The left column highlights the progress of the reaction: the top panel reports the gas-phase temperature, while the bottom one shows the oxygen mass fraction, both used as indicators of flame propagation. Additionally, the particles are plotted as Superimposed markers. Their color encodes the thermochemical state: dark blue corresponds to pure iron, yellow to fully oxidized FeO, and a more intense red indicates higher particle temperature. This representation highlights the coupling between fluid and dispersed phases, showing at once heat release, oxygen consumption, flow structures, and particle conversion. The right column focuses instead on the carrier flow: the top panel displays the y-component of fluid velocity, while the bottom one shows z-component of fluid velocity, which allows to identify regions of compression and expansion associated with heat release.

Two cases are considered:

- 1. Absence of fluid motion (laminar condition);
- 2. Fluid motion at different initial dissipation energies (turbulent condition).

3.2.1. Laminar case

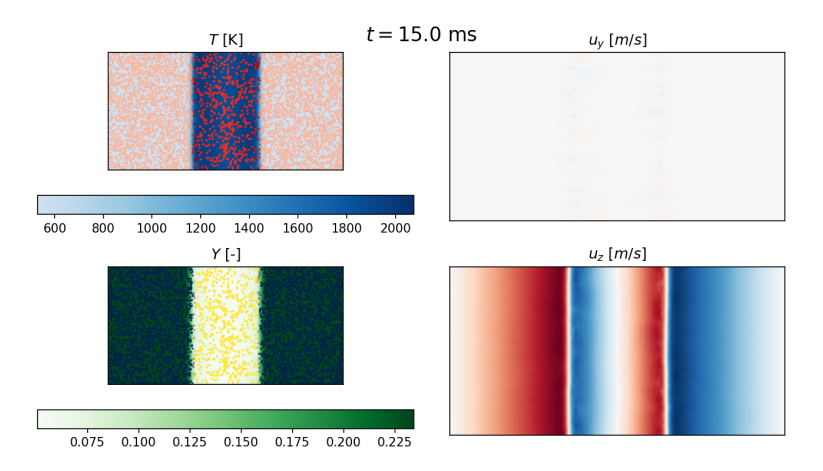


Figure 3.1.: Instantaneous y-z slices of laminar case at t=15 ms.

The slice in 3.1 shows the progression of the combustion after 15 ms from the beginning of the simulation. In the laminar configuration, the flame front propagates as a nearly planar sheet along the z-direction. A distinctive feature visible in this case is the concept of preheat layer in iron flames: particles located ahead of the front transfer heat to the surrounding gas, which gradually warms up until ignition occurs in the neighboring particles. This mechanism is particularly evident here, where the fluid temperature in the preheat region is already increasing while the dispersed phase still consists predominantly of pure iron. As the hot gas expands across the flame front, a local redistribution of particles becomes evident: they tend to concentrate in the still non-oxidized region, while their

concentration decreases within the flame zone, where combustion is consuming and the gas temperature reaches its maximum. Concerning the flow fields, the velocity in y-direction panel is identically zero, as expected one-dimensional propagation. In contrast, the velocity in z-direction panel highlights the expansion induced by heat release: near the flame front, blue regions correspond to flow directed toward the positive z-axis, while symmetric red region indicate flow directed in the opposite direction. This pattern reflects the bidirectional expansion of the hot gas across the flame sheet and confirms the local volumetric effects associated with combustion. These observations provide a clear qualitative picture of the particle—fluid coupling and highlight the physical role of the preheat layer in sustaining the flame propagation.

3.2.2. Turbulent case

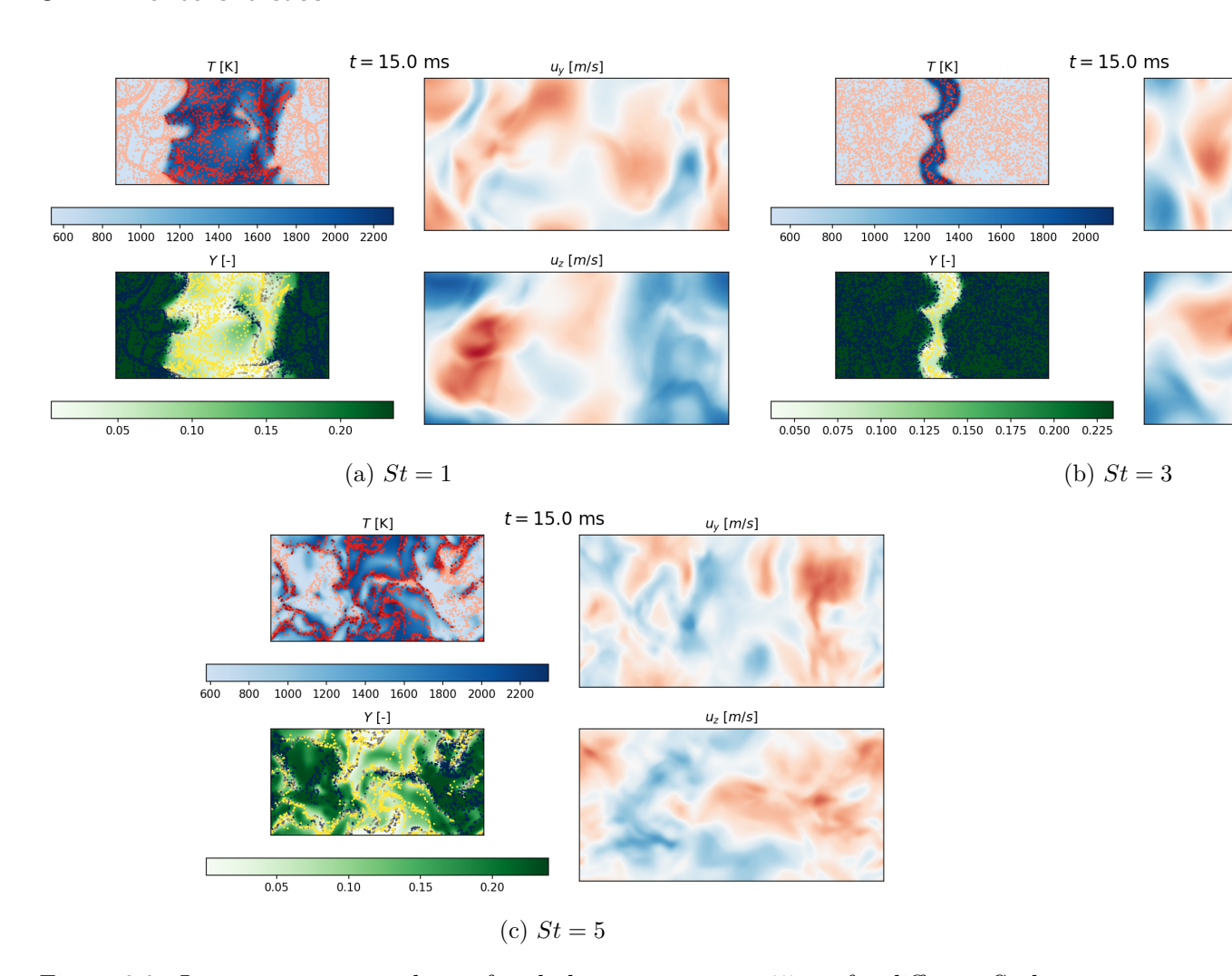


Figure 3.2.: Instantaneous y–z slices of turbulent cases at t=15 ms for different Stokes numbers. Increasing the Stokes number leads to stronger particle clustering, enhanced flame wrinkling, and broader flame brushes, resulting in faster iron consumption and extended oxygen depletion.

In the turbulent configurations, reported in Figures 3.2, the flame structure differs markedly from the laminar reference case. Turbulence broadens the reaction zone and promotes heterogeneous particle distributions due to inertia. Since the particles cannot exactly follow the turbulent eddies, they tend to concentrate in specific regions, producing clusters that act as localized sites of enhanced combustion when St > 1, consistently with previous

observations [40]. The dissipation rate of the carrier phase controls the intensity of these interactions: higher energy input generates smaller and more intense vortical structures, which interact more effectively with particle inertia and imprint significant corrugation on the front.

From the flow fields, the u_y panels reveal the not null velocity fluctuations in all directions that are responsible for flame wrinkling and folding, in sharp contrast with the null ones of the laminar case.

The velocity in z-direction panel highlights the strong expansion induced by heat release, now distributed in a highly irregular manner across the flame brush, with alternating regions of compression and expansion that follow the local turbulent fluctuations.

At St = 1, the extent of the flame is already considerably thickened compared to the laminar sheet, and the reaction extends across a larger fraction of the domain. Particle clusters of different sizes are visible within the flame, accelerating local oxidation and resulting in a faster overall consumption of iron.

At St = 3, the morphology changes drastically: strong vortices induce intense wrinkling, and the flame sheet begins to fold and embed into itself. The flame brush loses its homogeneity, becoming characterized by corrugated reaction zones interspersed with particle-rich regions.

At St = 5, the wrinkling is even more pronounced, and oxygen depletion appears across wide areas of the domain. Combustion is markedly accelerated, and the flame brush becomes fragmented and highly irregular. The combination of enhanced wrinkling and preferential particle clustering substantially enlarges the effective flame surface, anticipating a significant rise in the turbulent burning velocity.

Overall, these visualizations demonstrate the progressive transition from a thin and uniform laminar sheet to a broad and highly corrugated turbulent flame brush. Increasing the Stokes number amplifies clustering, front folding, and oxygen depletion, while the dissipation rate of the carrier flow governs the scale and intensity of these effects. Together, these mechanisms explain the expected increase in turbulent burning velocity S_T with turbulence intensity and particle inertia.

3.3. Postprocessing routine: flame front detection

This section presents the methodology developed to identify and reconstruct the flame surface from a three-dimensional cloud of points. Different approaches could be adopted for this purpose; however, the present work focuses on the Volume-of-Fluid (VOF) method, originally formulated within the finite volume framework. A brief introduction to its principles and context of application is provided first. Afterwards, more details are given on the post-processing routine used to visualize and define the flame front, with particular emphasis on the algorithm employed for surface reconstruction.

3.3.1. Geometric VOF: reconstructor step

The Volume-of-Fluid (VOF) method [45, 46, 47, 48], first proposed by Hirt and Nichols, is one of the most widely used interface-capturing techniques for incompressible multiphase flows in an Eulerian framework. In general, a fixed computational mesh is used, and the interface location is determined implicitly through the volume fraction α of one phase in

each computational cell. The volume fraction is defined as the cell-average of an indicator function which takes the value 1 inside one phase and 0 inside the other. Accordingly,

$$\alpha = \begin{cases} 0, & \text{for a point inside fluid A,} \\ 0 < \alpha < 1, & \text{for a point in the interfacial region,} \\ 1, & \text{for a point inside fluid B.} \end{cases}$$
 (3.11)

The volume fraction is transported with the flow according to the advection equation

$$\frac{\partial \alpha}{\partial t} + \nabla \cdot (\alpha \mathbf{u}) = 0, \tag{3.12}$$

so that the interface is implicitly convected by the velocity field.

Two main formulations of the VOF method are commonly distinguished: algebraic and geometric. In algebraic approaches, the volume fraction is updated directly using high-resolution advection schemes. These methods are relatively simple and efficient on arbitrary meshes, but they tend to suffer from numerical diffusion, which produces a smeared interface. [47] In geometric approaches, by contrast, the interface is explicitly reconstructed within each mixed cell, typically using planar segments as in the piecewise-linear interface calculation (PLIC) [49]. This reconstruction yields a sharper and more accurate description of the interface, at the expense of additional geometric computations.

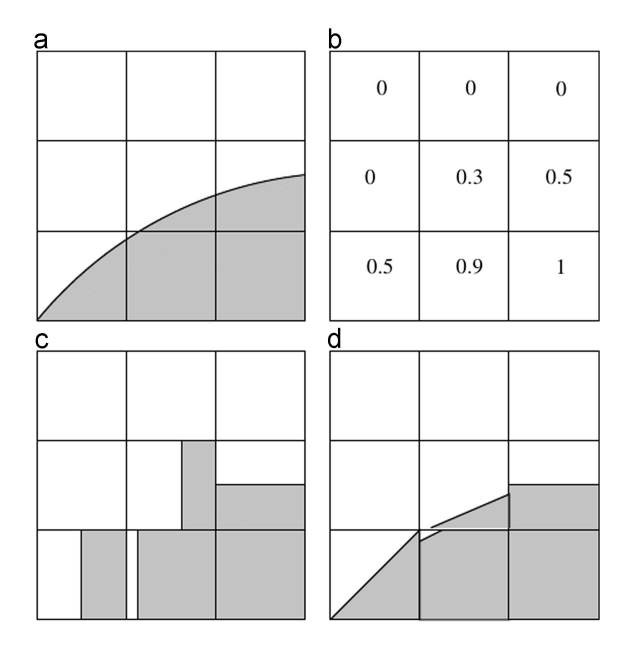


Figure 3.3.: Comparison of geometric reconstruction methods in the VOF framework. Panel (a) shows the exact interface, while panel (b) represents the corresponding volume fractions. Panel (c) illustrates the simple line interface construction (SLIC), where the interface is approximated by segments aligned with the grid. Panel (d) shows the piecewise-linear interface construction (PLIC), in which segments can be arbitrarily oriented, yielding a sharper and more accurate representation. Reprinted from [45].

Figure 3.3 illustrates the difference between two geometric reconstruction strategies commonly employed in the VOF framework. In the simple line interface construction (SLIC), the iso-surface is approximated by grid-aligned segments, which leads to a rather crude representation. The piecewise-linear interface construction (PLIC), instead, reconstructs the interface using arbitrarily oriented segments or planes, resulting in a much sharper and

more accurate description. For this reason, PLIC has become the most widely adopted geometric reconstruction method.

The geometric VOF scheme can be conceptually divided into two steps. The first is the reconstruction step, in which the iso-surface at a chosen volume fraction level is built inside all interface cells with $0 < \alpha < 1$. The second is the advection step, in which the reconstructed interface is transported according to the velocity field. In the present work, only the reconstruction step is deepened, since the flame front detection is done in the post-processing.

According to the analysis of López [50], the accuracy of VOF simulations depends on several factors. The reconstruction step must be sufficiently precise to minimize geometric errors within each interface cell. The advection of the volume fraction should be carried out with conservative, high-order schemes to preserve mass and maintain interface sharpness. Furthermore, mesh refinement is necessary in regions of complex interface topology in order to capture small-scale features. The study also emphasizes that although finer grids reduce numerical error, the overall convergence rate depends on the interplay between reconstruction and advection. In practice, second-order convergence of the interface position can be achieved only if both steps are treated with sufficient numerical rigor.

3.3.2. Marching cubes algorithm

A similar purpose to the reconstruction step of the geometric VOF method is achieved with the Marching Cubes (MC) algorithm. The *Marching Cubes* algorithm, originally proposed by Lorensen and Cline, is a widely used technique to extract an iso-surface from volumetric datasets defined on a structured three-dimensional grid [51]. It stands out for its efficiency and its ability to produce high-quality triangulated surfaces.

The MC algorithm operates on a volumetric dataset represented as a three-dimensional grid of voxels, each associated with a scalar value. The domain can be viewed as a stack of logical cubes, where each cube is defined by eight neighboring voxels. Given a prescribed iso-value f^* , the objective is to reconstruct the surface corresponding to the set of points that satisfy

$$f(\mathbf{x}) = f^*. \tag{3.13}$$

The algorithm iterates, i.e. marches, through all cubes in the grid. Each vertex of a cube is classified as either inside $(f > f^*)$ or outside $(f \le f^*)$, producing a binary pattern that distinguishes the local configuration of the surface. Since each cube has eight vertices, $2^8 = 256$ possible patterns exist, which, exploiting symmetries, reduce to 15 unique topological cases which are shown in Fig. 3.4.

In order to generate a structured volumetric grid from irregular data, a midpoint comparison strategy can be adopted. Each point within a cube is projected onto the coordinate axes and classified with respect to the cube midpoint. Depending on this classification, binary values are assigned to the cube vertices, which are then used to define whether they lie inside or outside the iso-surface. Figure 3.5 schematically illustrates this procedure, showing how a consistent binary representation allows the construction of a regular three-dimensional grid suitable for surface reconstruction [51].

For each configuration, a precomputed lookup table defines which cube edges are intersected and how the corresponding points are connected to form triangular facets. This ensures consistency and avoids ambiguity in the surface generation. The exact position of the intersection point \mathbf{x}_{cut} along an edge between two vertices \mathbf{p}_k and \mathbf{p}_l is obtained by linear

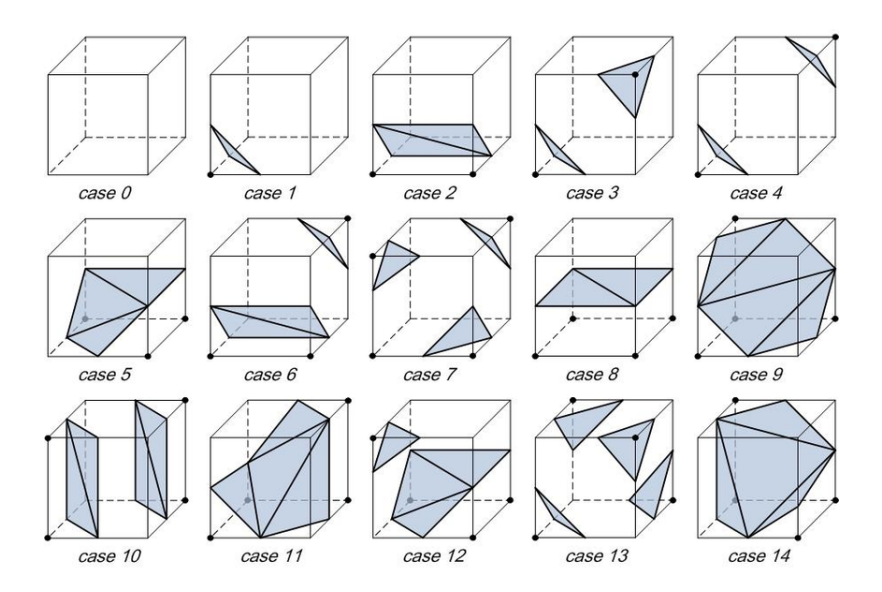


Figure 3.4.: Type of surface combinations for the Marching Cubes algorithm. The black circles mean that the vertices inside the surface. Reprinted from [51].

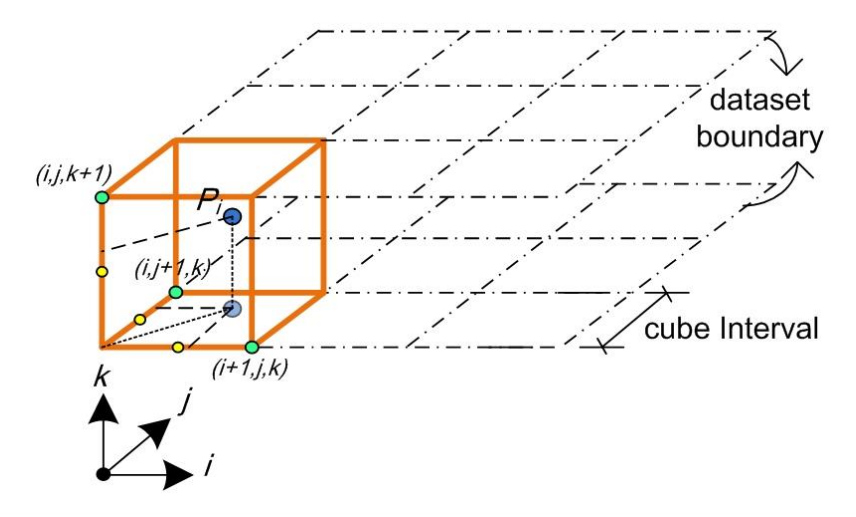


Figure 3.5.: Grid arrangement. Yellow points denote the midpoint of each edge. The vertex will be highlighted if it receives a binary one. Printed from [51].

interpolation:

$$\mathbf{x}_{\text{cut}} = \mathbf{p}_k + \frac{f^* - f_k}{f_l - f_k} \left(\mathbf{p}_l - \mathbf{p}_k \right), \tag{3.14}$$

where f_k and f_l are the scalar values at the vertices.

The MC algorithm produces a continuous mesh of the iso-surface. Surface normals are also computed as the normalized gradient of the scalar field:

$$\mathbf{n} = \frac{\nabla f}{\|\nabla f\|},\tag{3.15}$$

It must be noted that this procedure is inherently local, since each cube is processed independently based only on its eight vertices. As a result, iso-surfaces may be generated even when the average scalar value within a cell lies entirely above or below the threshold, provided that at least one edge connects vertices on opposite sides of the iso-value. This

can produce fragmented or inconsistent surfaces in regions with weak gradients or noisy data. Kobbelt et al. [52] show that the standard piecewise trilinear interpolation fails to capture directional information near sharp features, leading to large errors in the estimated intersection points. Newman and Yi [53] also highlight that standard MC iso-surfaces often exhibit visible faceting artifacts, particularly when the grid resolution is coarse or non-uniform, since the linear interpolation in each cube cannot recover smooth variations across larger scales. They suggest that higher-order iso-surface representations or enriched data structures are required to reduce these artifacts and improve the accuracy of the reconstruction.

Within this framework, the role of the volume fraction is played by a progressive variable that accounts for the combustion reaction state in space and distinguishes between oxidized and non-oxidized regions, whose concept was already introduced in Section 2.2.4. In the case of iron particle cloud flames, the FeO mass fraction is used instead as the analogue of the volume fraction: cells containing mostly pure iron correspond to values close to zero, while fully oxidized regions correspond to values close to one. The iso-surface extracted at an intermediate value therefore represents the interface between burnt and unburnt states, which in this work is identified as the flame front. The mass fraction of iron oxide $\omega_{\rm FeO}$, here referred to as the oxidation fraction $C_{ox}(\mathbf{x},t)$, is defined as:

$$C_{ox,p}(\mathbf{x},t) = \left(1 - \frac{m_{Fe,p}(\mathbf{x},t)}{m_{part,p}(\mathbf{x},t)}\right), \text{ with } p = 0, \dots, N_{part} - 1$$
(3.16)

where $m_{Fe,p}$ is the mass of the iron core of particle p, and $m_{part,p}$ is the total particle mass at position \mathbf{x} and time t. Consistently with the definition in Section 2.2.4:

$$c_{ox}(\mathbf{x},t) = \frac{C_{ox}(\mathbf{x},t) - C_{ox,u}}{C_{ox,b} - C_{ox,u}}$$
(3.17)

Since $C_{ox,u} = 0$ and $C_{ox,b} = 1$, this expression simply reduces to $c_{ox}(\mathbf{x},t) = C_{ox}(\mathbf{x},t)$.

Given the output data of the simulation, the particle-based information must first be reformulated into a structured volumetric dataset suitable as input for the Marching Cubes algorithm. At each time step, the available data consist of the particle spatial coordinates $\mathbf{x}_p(t)$, the corresponding oxidation fraction $C_{ox,p}(t)$, and the particle temperature $T_p(t)$, with $p = 0, \ldots, N_{part} - 1$.

To transform these scattered data into a volumetric representation, a box-counting procedure is applied. The computational domain is discretized into a structured Cartesian grid with different spacing, where the number of divisions along each axis can be independently specified (e.g. $N_x \neq N_y \neq N_z$). The resolution of this grid, i.e. the number of cells along each direction, is a user-defined parameter that directly determines the spatial detail of the reconstructed surface. In this work, a resolution of $N_b = (10, 10, 100)$ is employed, while alternative choices are discussed in Section 4.1.2.

For each grid cell (i, j, k), where $i = 0, \dots, N_{b,x} - 1, j = 0, \dots, N_{b,y} - 1$ and $k = 0, \dots, N_{b,z} - 1$, all particles located within its spatial bounds are identified, yielding a local count $N_{part}^{(i,j,k)}$. Cell-averaged values of oxidation fraction and temperature are then computed through a Voronoi-based weighting of the particle contributions:

$$\overline{\omega}_{ox}^{(i,j,k)} = \frac{\sum_{p=1}^{N_{\text{part}}^{(i,j,k)}} \omega_{ox,p}^{(i,j,k)} v_p^{(i,j,k)}}{\sum_{p=1}^{N_{\text{part}}^{(i,j,k)}} v_p^{(i,j,k)}},$$
(3.18)

$$\overline{T}^{(i,j,k)} = \frac{\sum_{p=1}^{N_{\text{part}}^{(i,j,k)}} T_p^{(i,j,k)} v_p^{(i,j,k)}}{\sum_{p=1}^{N_{\text{part}}^{(i,j,k)}} v_p^{(i,j,k)}},$$
(3.19)

where v_p denotes the normalized Voronoi volume associated with each particle, defined with respect to the mean particle volume $\langle v \rangle$

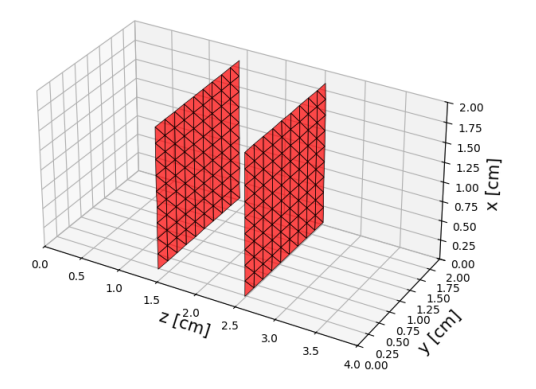
$$\langle v \rangle = \sum_{p=1}^{N_{part}} v_p = \frac{L^3}{N_{part}} \tag{3.20}$$

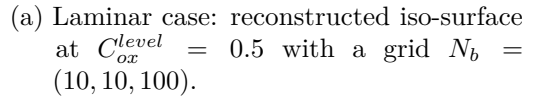
This procedure defines two volumetric datasets, $\overline{C}_{ox}^{(i,j,k)}$ and $\overline{T}^{(i,j,k)}$, located at the grid cell centers and readable by the Marching Cubes algorithm. A simpler arithmetic mean was initially tested, but it resulted in significant inaccuracies in the flame propagation. The Voronoi tessellation was therefore introduced to ensure a more consistent representation of the front. Further discussion of its impact is provided in Section 4.1.

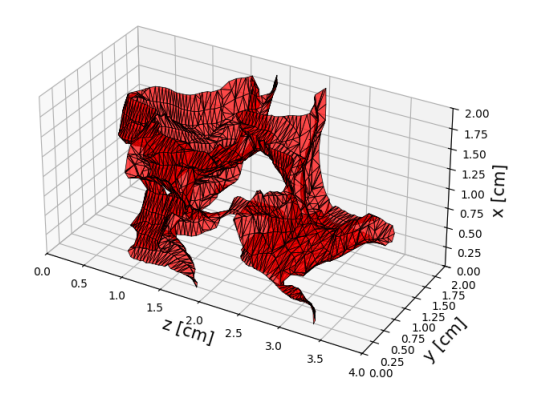
Once the volumetric dataset has been constructed, the Marching Cubes algorithm is applied to extract the iso-surface corresponding to the flame front. In this work, the oxidation fraction field $\overline{C}_{ox}^{(i,j,k)}$ is selected as the input variable, with the iso-value fixed at $C_{ox}^{level}=0.5$ to separate burnt and unburnt regions. The temperature volume data $\overline{T}^{(i,j,k)}$ could also be used for the same purpose, yielding comparable results, though the choice of C_{ox}^{level} is more consistent with the combustion progress variable definition introduced earlier.

The algorithm processes the grid cell by cell and, for each configuration, reconstructs the triangular facets that approximate the flame front. The output consists of: the coordinates of the iso-surface vertices, the triangular faces that connect them, the normals to each facet, and the values interpolated at the vertices. All coordinates are expressed in the physical reference frame of the simulation, with spacing given by the Cartesian grid.

Figure 3.6 shows the three-dimensional iso-surfaces reconstructed with the Marching Cubes algorithm for the laminar case (Fig. 3.6a) and for the turbulent configuration at St=1 (Fig. 3.6b). In the laminar case, the flame front is reconstructed as an almost planar surface, so that only two triangular facets per cell are sufficient to represent its progression. Conversely, in the turbulent case, a much larger number of triangular elements is required to capture the pronounced wrinkling and broadening of the front.







(b) Turbulent case at St = 1: reconstructed iso-surface at $C_{ox}^{level} = 0.5$ with a grid $N_b = (10, 10, 100)$.

Figure 3.6.: Three-dimensional plots of the iso-surfaces reconstructed with the Marching Cubes algorithm in laminar and turbulent conditions. Additional plots are reported in C.3.

In both cases, a sharp interface is obtained from volumetric data through linear interpolation along grid edges. However, reconstruction errors may still occur due to limited grid resolution, the inherent linear interpolation of the algorithm, and the choice of iso-value used to define the front. In particular, when the oxidation field becomes nearly homogeneous along the propagation direction, i.e. laminar case, the interface location becomes increasingly sensitive to numerical noise and threshold selection [52, 53].

The flame properties, such as position, velocity and area, are then computed for the one-dimensional flame propagation. From the reconstructed mesh, quantitative flame properties can be derived. Two key observables are considered: the flame surface area, which measures the instantaneous wrinkling and spatial development of the front, and the flame propagation velocity.

The flame surface area is obtained by summing the contributions of all triangular facets:

$$A_{\text{front}} = \sum_{t=1}^{N_{\text{tri}}} A_t, \tag{3.21}$$

with each triangular area A_t computed from its three vertices coordinates $\mathbf{v_1}$, $\mathbf{v_2}$ and $\mathbf{v_3}$ using the vector cross product:

$$A_t = \frac{1}{2} \left| (\mathbf{v}_2 - \mathbf{v}_1) \times (\mathbf{v}_3 - \mathbf{v}_1) \right|. \tag{3.22}$$

To evaluate the propagation velocity of the flame, the position of the front is first determined from the reconstructed iso-surface. At each time step, the centroid of every triangular facet is computed and an area-weighted average is used to identify the representative front location. The flame speed is then calculated as the instantaneous displacement of this averaged position:

$$\vec{v}_{\text{front}}(t) \approx \frac{\mathbf{c}_{\text{mid}}(t + \Delta t) - \mathbf{c}_{\text{mid}}(t)}{\Delta t}.$$
 (3.23)

where \mathbf{c}_{mid} expresses the average midpoint coordinates. Since two distinct flame fronts develop along the z-axis, one propagating in the positive direction and the other in the negative direction, the global flame velocity is defined as the average of their respective speeds. The mean of v_{front}^+ and v_{front}^- will be referred to as S_L or S_T depending on the case, respectively laminar or turbulent flow.

Laminar flame speed

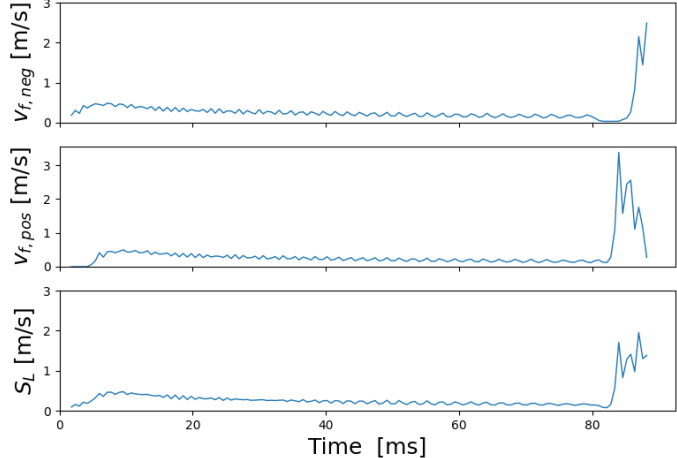


Figure 3.7.: Laminar flame speed for the simulation case with $N_b = (10, 10, 100)$.

Figure 3.7 reports the temporal evolution of the front velocity in the laminar configuration, showing separately the positive front, the negative front, and their mean. It can be

observed that the oscillations of the two fronts tend to compensate in the mean, producing an artificially smoother velocity curve. For this reason, the analysis presented in Section 4.1 will primarily rely on the position of the flame front rather than on the averaged velocity.

This methodology thus allows to relate the geometric reconstruction provided by Marching Cubes with physically relevant flame descriptors, enabling the analysis of both instantaneous structure and temporal dynamics of the front.

4. Results and evaluations

In this chapter, the results of the analysis are presented together with their evaluation and interpretation. The main objective is to investigate whether a correlation exists between flame velocity, flame surface area, and turbulence intensity. The discussion is carried out in the context of the existing literature on turbulent premixed flames introduced in Section 2.2.

Several challenges were encountered, particularly regarding the determination of the burning velocity. The reliability of the adopted methodology to detect the flame described in Section 3.3.2 revealed certain limitations. While the Marching Cubes algorithm itself introduces numerical inaccuracies, as already discussed in Section 3.3.2, these inaccuracies are also influenced by the quality of the input data produced by the box-counting step.

A parametric study was performed to optimize the procedure over the laminar simulation. The analysis relies on three types of diagnostic plots: flame position, burning velocity, and flame surface area. These quantities allow one to evaluate how the outcomes change with the variation of the analysis parameters. The laminar case is used for this kind of analysis due to the predictability of its behavior. It should be noted that the Marching Cubes algorithm can reconstruct the interface only when the chosen threshold lies within the actual range of values; therefore, the very first stages of the simulation, when the reaction has just started, are excluded from the analysis.

Finally, the outcomes of different simulation setups are compared. First, the effect of the particle number on the reconstruction procedure is analyzed. Then, the sensitivity of the flame structure to turbulence is investigated, with reference to the available literature on premixed flames.

4.1. Iso-surface reconstruction: inaccuracies and influencing parameters

In order to evaluate the accuracy of the reconstructed flame front, it is essential to first examine the procedure that generates the volumetric input data for the Marching Cubes algorithm. This step, defined as box-counting procedure in 3.3.2, is critical because any inaccuracy introduced at this stage inevitably propagates into the final iso-surface reconstruction. The aim of this section is therefore twofold: first, to assess how much of the discrepancy observed in the reconstructed flame front originates from the MC algorithm itself, and second, to highlight the limitations of the box-counting procedure. To this end, two complementary analyses are presented. On one side, the reliability of MC is tested using fluid temperature fields, which allow a direct evaluation of the algorithm's intrinsic accuracy. On the other, the effect of box-counting is investigated by comparing simple particle averaging with a Voronoi-weighted approach. Together, these tests provide insight into the origin of the inaccuracies and guide the choice of the most suitable post-processing strategy.

The reliability of the MC algorithm has therefore been tested by providing as input the fluid temperature field instead of particle-based quantities. In this way, the reconstruction

is independent of the box-counting procedure and only reflects the intrinsic accuracy of MC. The isothermal iso-surface was extracted at

$$T^{level} = \frac{T_{high} + T_{low}}{2},$$

where T_{high} and T_{low} represent the peak and initial fluid temperatures, respectively. Figure 4.1 shows that, in laminar conditions, the expected linear propagation of the front is well represented by the isothermal iso-surface reconstructed by MC. Conversely, when particlebased quantities are used as input, the flame front appears less regular and significantly less accurate. This indicates that most of the bias arises from the box-counting procedure rather than the MC algorithm itself. In contrast, when the same analysis is performed using the oxidation fraction reconstructed with the box-counting procedure, significant discrepancies appear. Figure 4.1 highlights this comparison: the red line represents the flame position obtained from the isothermal approach, while the black and blue lines show the result using the oxidation fraction mapped through box-counting, computed either as the mean value either with the Voronoi volumes weighted average. Two issues become evident. First, at the beginning of the simulation MC does not detect any vertices. This happens because the selected iso-value does not lie within the range of minimum and maximum values of the dataset, so the algorithm cannot reconstruct a surface. Second, once the flame develops, oscillations appear in the box-counting result, leading to a less smooth and less accurate representation of the flame propagation. Furthermore, it is shown the modest increase in resolution gained by using the weighted average rather than the mean value. However an improvement of the resolution is necessary.

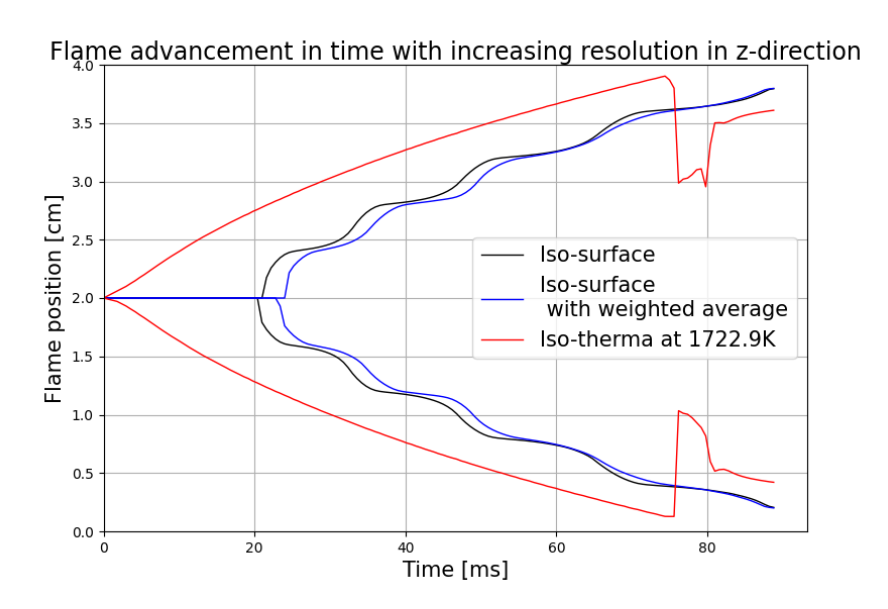


Figure 4.1.: Comparison between the flame position computed with the isothermal approach (red curve) and with the oxidation fraction values at the nodes of the grid, computed either as the mean value (black curve) either as the Voronoi volumes weighted average (blue curve). An uniform number of boxes of 10 is here selected in all directions.

The final deviation of the ref curves representing the fluid isothermal curves is justified by the progression of combustion once the flame reaches the end of the domain. Hot-spots and cooling due to the particles might be present since a $\Phi=0.8$ is set to be reached. Additional analysis done for the isothermal line are reported in the Appendix C.1.

This comparison clarifies that the core of the problem lies not in the Marching Cubes reconstruction itself, but in the pre-processing step that reformulates particle-based information into gridded volumetric data. The box-counting approach, in its basic form, introduces inaccuracies that propagate into the MC output.

The box-counting procedure was originally introduced to transform particle-based quantities, such as temperature or oxidation fraction, into values defined at the nodes of a regular grid. In its simplest form, this is achieved by averaging the properties of the particles contained within each box.

$$\overline{\omega}_{ox}^{(i,j,k)} = \frac{\sum_{p=1}^{N_{\text{part}}^{(i,j,k)}} \omega_{ox,p}^{(i,j,k)}}{N_{\text{part}}^{(i,j,k)}},$$
(4.1)

$$\overline{T}^{(i,j,k)} = \frac{\sum_{p=1}^{N_{\text{part}}^{(i,j,k)}} T_p^{(i,j,k)}}{N_{\text{part}}^{(i,j,k)}},$$
(4.2)

Where
$$i = 0, \dots, N_{b,x} - 1, j = 0, \dots, N_{b,y} - 1 \text{ and } k = 0, \dots, N_{b,z} - 1.$$

However, this approach introduces a systematic error that becomes particularly evident in the cells partially traversed by the flame front.

To further illustrate this problem, a simplified scenario is shown in Fig. 4.2. The figure represents a control volume (CV) partially traversed by the flame front. In this configuration, burnt particles (red points, $C_{ox,p} = 1$) are concentrated in the already reacted region, while unburnt particles ($C_{ox,p} < 1$) occupy the remaining part of the cell.

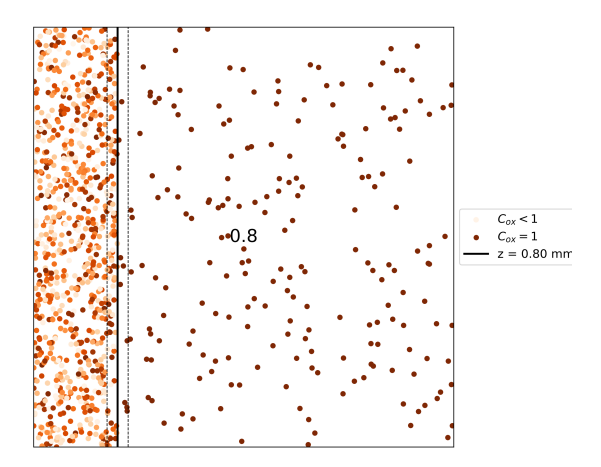


Figure 4.2.: Random reproduced data to evidence the issue with *box-counting*. On the abscissa is plotted the z-axis, i.e. direction of propagation of the front, positive towards right, and on the ordinate the y-axis.

The plot corresponds to a slice of the domain in the z-y plane, where the flame propagates along the negative z-direction. The global setup consists of a uniform grid with $N_b = (10, 10, 10)$ and a total particle number $N_{part} = 1768667$.

Since the pressure is assumed to be spatially uniform, the combustion reaction, through heat release from the reacting particles to the surrounding fluid, leads to a local temperature rise at the flame front. Under constant pressure, this temperature increase causes the fluid to expand, generating a flow field directed outward from the burnt region. The particles follow the fluid displacement induced by thermal expansion, resulting in their redistribution away from the reaction zone.

In the illustrative case of Fig. 4.2, however, only 1030 particles are found in the selected control volume, which corresponds to a cell partially crossed by the flame front with an average oxidation fraction of $\overline{C}_{ox}=0.8$. This number is significantly lower than the ~ 1768 particles expected under uniform distribution, underlining how the expansion-driven motion of the fluid alters the particle distribution across the domain.

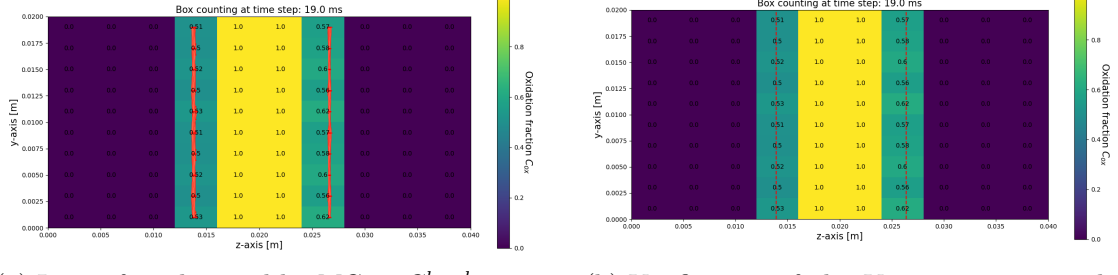
As a consequence, when computing the average oxidation fraction over the control volume, the contribution of the unburnt particles is overrepresented, and the resulting mean value underestimates the actual advancement of the flame front. This explains why the boxcounting approach does not provide a faithful representation of the real flame progression.

This simplified example highlights the main limitation of the box-counting procedure: whenever a cell is only partially crossed by the flame front, the uneven particle distribution biases the averaged values and leads to an underestimation of the actual flame progression.

Consequently, a different strategy is required. To mitigate this error, a weighted average based on the Voronoi volume is adopted. A post-processing tool performs the Voronoi tessellation on the three-dimensional particle distribution, assigning each particle a representative volume. The size of this volume reflects local clustering: smaller Voronoi cells indicate higher particle concentrations, while larger cells correspond to more dilute regions [40]. These volumes are then used as weights in the averaging process, providing a more consistent description of temperature and oxidation levels across the grid.

This approach improves the reconstruction, since burnt particles—characterized by higher Voronoi volumes due to fluid expansion—contribute appropriately to the average, reducing the bias observed with simple box-counting.

Nonetheless, the accuracy of the outcome still depends strongly on grid resolution. If the boxes are too large relative to the number of particles inside, the weighted mean cannot reliably represent the underlying dynamics. Grid refinement is therefore essential to capture the flame front propagation and its temporal development.



- (a) Iso-surface detected by MC at $C_{ox}^{level} = 0.5$ with a grid $N_b = (10, 10, 10)$.
- (b) Verification of the Voronoi average value with the same grid $N_b = (10, 10, 10)$.

Figure 4.3.: Comparison of the laminar simulation setup: (a) MC reconstruction, (b) expected result from Voronoi averaging.

Figure 4.3 compares the flame front reconstruction obtained with the Marching Cubes algorithm and the expected front position derived from the Voronoi-averaged oxidation fraction. Both plots show the background field of box-averaged oxidation fraction.

In the left panel, the iso-surface extracted by Marching Cubes at $C_{ox}^{level} = 0.5$ is shown in red, with the red dots marking the vertices identified by the algorithm.

In the right panel, the expected front position is plotted instead, computed as the percentage of the control volume already oxidized within each box.

The discrepancy between the two plots is evident: in the Marching Cubes reconstruction the flame front does not coincide with the expected fraction of oxidized volume, which highlights the bias introduced by the box-counting procedure. This deviation is particularly pronounced in cells partially traversed by the flame, where the particle distribution is not uniform.

The limitations discussed above are not unique to the present case and have already been addressed in the literature. A well-known numerical strategy to treat large particle systems is the *Particle-in-Cell* (PIC) method, originally introduced by Harlow [54] and Dawson [55] in the context of nuclear physics. This hybrid approach combines Lagrangian and Eulerian descriptions but is known to suffer from particle—noise issues when the particle distribution is not uniform, as in the present study.

To alleviate this problem, alternative refinements such as the *Sparse Grid Method* [56] have been proposed. The core idea is to concentrate resolution only where strong gradients or sharp transitions occur, thereby reducing computational cost while retaining accuracy. Although not implemented here, the same philosophy could be applied in post-processing, refining the grid only in regions traversed by the flame front.

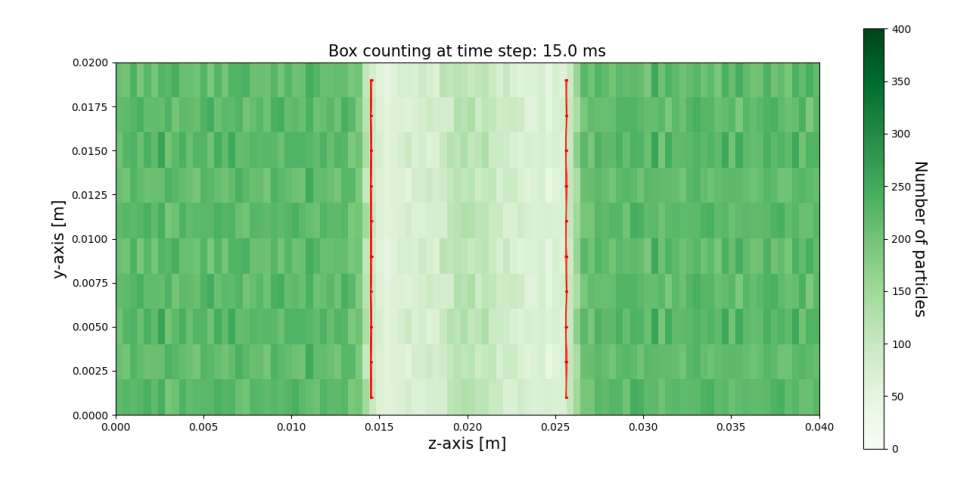
4.1.1. Flame Front Visualization

The following figures illustrate the reconstructed flame front at a representative instant of the simulation for both laminar and turbulent configurations. The analysis is performed on a two-dimensional z-y slice of the domain at x=0. Each figure reports three scalar fields obtained from the box-counting procedure: the number of particles, the Voronoi-weighted oxidation fraction, and the Voronoi-weighted temperature. The corresponding ranges are shown by the colorbars. The red iso-surface represents the front detected by the marching cubes algorithm with $N_b = (10, 10, 100)$ and $C_{ox}^{level} = 0.5$, while the red dots indicate the vertices computed by the algorithm.

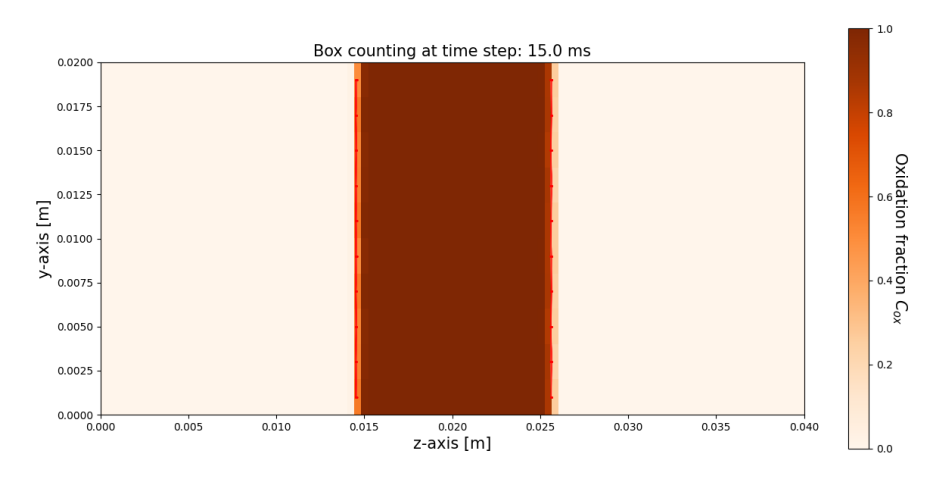
In the laminar case (Fig. 4.4), the reconstructed iso-surface is planar and aligned with the x-y direction. On the z-y slice this appears as a vertical line that advances steadily along the propagation axis z. This linear progression confirms the ability of the chosen resolution to capture the expected one-dimensional flame motion. The Voronoi-weighted fields show sharp gradients of oxidation fraction and temperature across the front, with unburned particles in the upstream region and oxidized ones downstream. The number of particles is lower in the boxes intersected by the flame front compared to the fresh region, since particle displacement is governed by the expansion of the fluid during combustion.

In the turbulent case (Fig. 4.5), the flame surface appears strongly wrinkled due to the action of turbulent eddies, in contrast to the planar structure observed in the laminar setup. The Voronoi-averaged oxidation fraction and temperature fields highlight the complex local gradients produced by turbulence, and the particle number distribution shows a tendency of the iron particles to form clusters, consistent with preferential concentration induced by inertia.

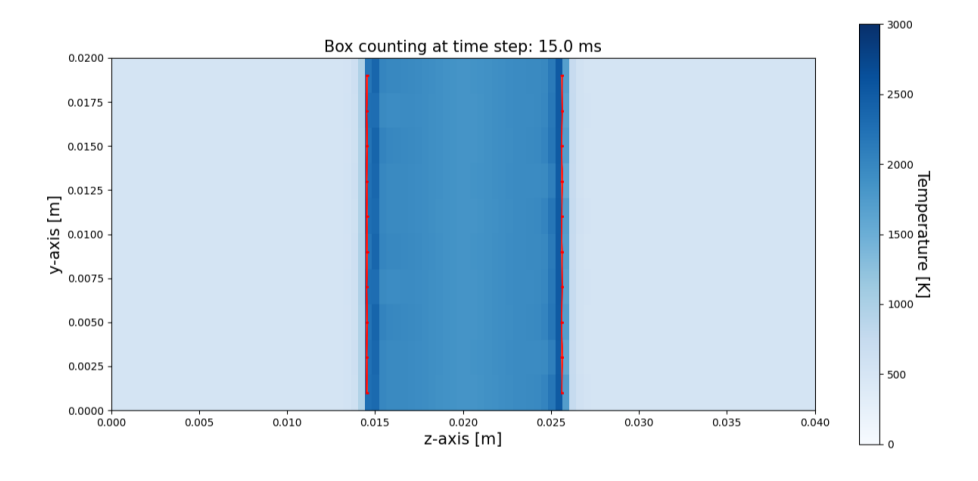
4.1.1.1. Laminar case



(a) Number of particles in the grid cells.



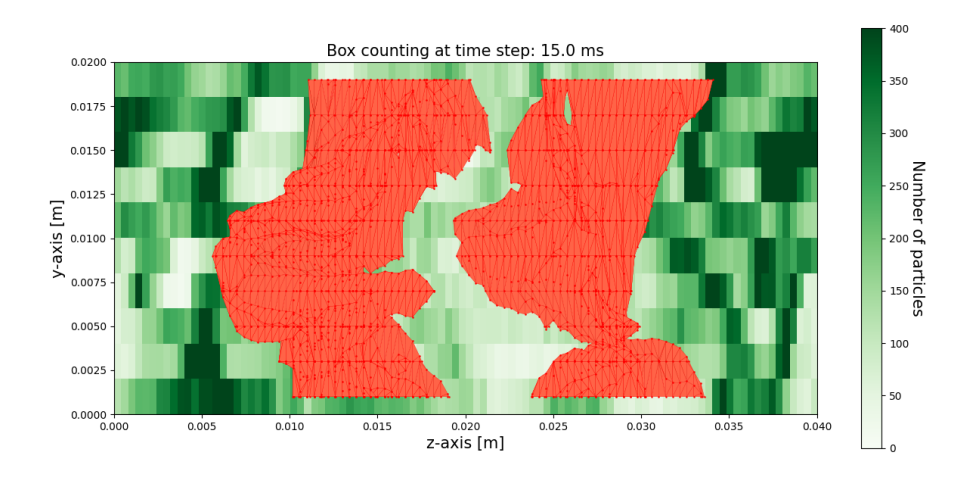
(b) Voronoi-weighted box average of the oxidation fraction.



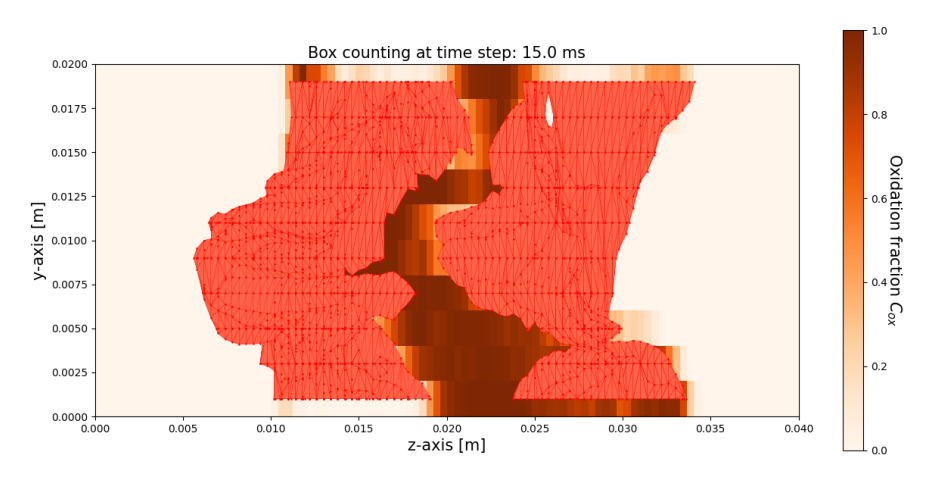
(c) Voronoi-weighted box average of the temperature.

Figure 4.4.: Laminar setup: z-y slice at x=0 after t=75 ms. The red line is the flame front at $C_{ox}^{level}=0.5$, grid $N_b=(10,10,100)$.

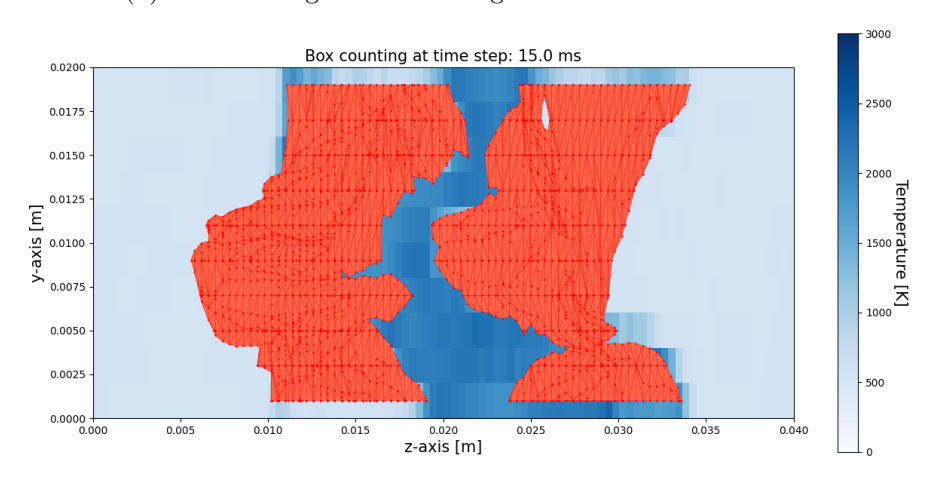
4.1.1.2. Turbulent case



(a) Number of particles in the grid cells.



(b) Voronoi-weighted box average of the oxidation fraction.



(c) Voronoi-weighted box average of the temperature.

Figure 4.5.: Turbulent setup at St=1: z-y slice at x=0 after t=75 ms. The red surface is the flame front at $C_{ox}^{level}=0.5$, grid $N_b=(10,10,100)$.

4.1.2. Number of boxes N_b

The first parameter investigated in the sensitivity analysis is the number of boxes N_b used in the box-counting procedure. The grid resolution strongly affects the capability of the algorithm to correctly capture the flame front. In order to limit the computational cost, the refinement is applied only along the propagation direction (z-axis), while the transverse directions are kept rough. Preliminary tests with uniform refinement in all directions showed no significant improvement compared to refining only along z, but with a considerably higher computational expense.

Figure 4.6 shows the position of the two flame fronts, one propagating in the positive z-direction (solid line) and the other in the negative z-direction (dashed line), for different values of N_b with $C_{ox}^{level} = 0.5$. An uniform grid is used in all directions in this comparison.

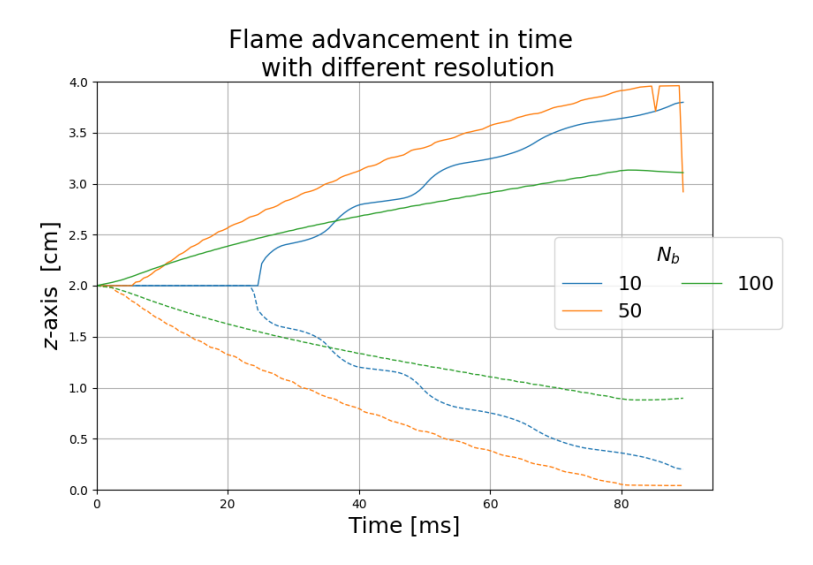


Figure 4.6.: Flame position over time for different values of N_b , all at $C_{ox}^{level} = 0.5$. In particular an uniform grid is used here in all directions.

At a coarse resolution of $N_b = (10, 10, 10)$, the algorithm is not able to properly capture the propagation of the flame front in the laminar setup. The marching cubes procedure frequently fails to detect iso-surface vertices, which results in long intervals where the front position appears to remain constant, followed by abrupt jumps. This behaviour produces an irregular and unrealistic description of the front advancement. Increasing the resolution to $N_b = (50, 50, 50)$ improves the accuracy, but residual oscillations and discontinuities are still present, indicating that the procedure has not yet reached convergence. A further refinement to $N_b = (100, 100, 100)$ leads to a nearly linear evolution of the flame position in time, consistent with the expected laminar propagation. However, the front position is slightly underestimated: the flame does not reach the end of the computational domain and the curve eventually saturates at a constant value. The results obtained with a uniform refinement in all directions suggest that refining the grid isotropically increases the computational cost without providing a substantial improvement in the description of the flame dynamics compared to a refinement restricted to the z-direction.

Based on these considerations, the parametric analysis is therefore restricted to grid refinement along the z-direction only, which corresponds to the main propagation axis of the flame front. To assess the influence of $N_{b,z}$, the evolution in time of three quantities are examined: the flame front position (Fig. 4.7a), the instantaneous burning velocity (Fig. 4.7b), and the flame surface area (Fig. 4.7c). These quantities are evaluated using the procedure described in Section 3.3.2.

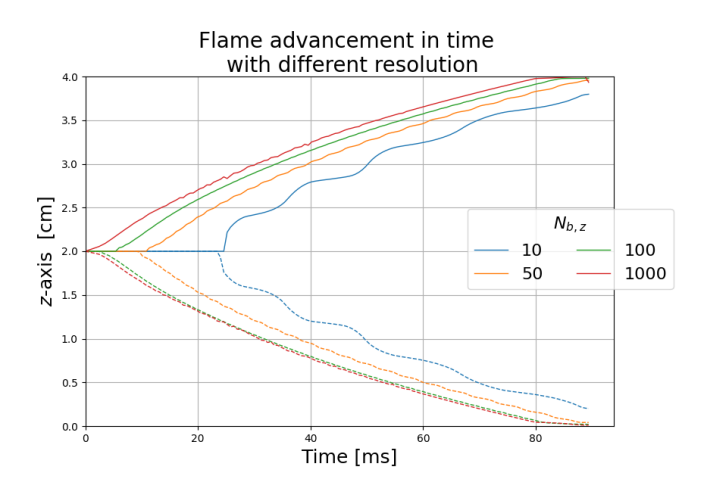
It should be noted that, in the velocity plots, the very first instants of the simulation are omitted since they do not represent the actual physical behavior of the flame. In this initial phase, the velocity shows an artificial peak due to the first displacement of the front that produces unrealistically high values.

At first, a rectilinear grid with $N_{b,z}=10$ was considered. At this very coarse resolution, the box size is too large to capture the spatial distribution of the burning iron particles and, consequently, the linear progression of the flame front. The marching cubes algorithm frequently fails to identify iso-surface vertices during the first time steps, producing long intervals with no detected propagation followed by abrupt jumps. This explains the highly irregular behavior observed in the position curve. The same effect is even more pronounced in the velocity, which is computed as the temporal derivative of the position over equal time intervals. Any abrupt change in the detected position therefore translates into strong fluctuations in the velocity signal, which are purely numerical and not representative of the flame dynamics. The flame surface area also shows an unrealistic evolution: the initial peak corresponds to the delayed detection of the iso-surface, and the convergence to the expected cross-sectional value $L_x L_y$ occurs later than at finer resolutions, again because the algorithm initially fails to identify vertices. Even after convergence, residual oscillations remain visible.

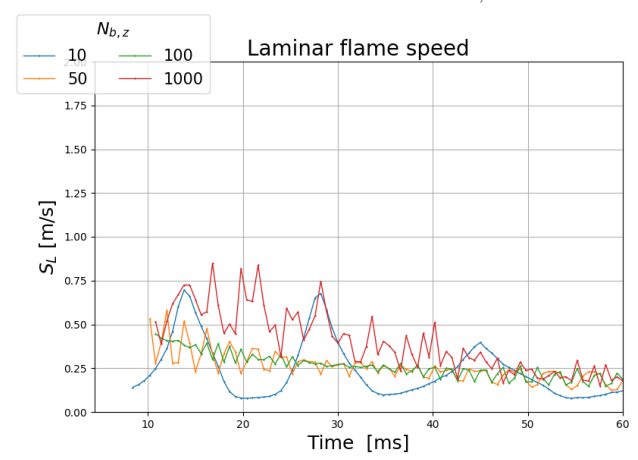
Increasing the resolution to $N_{b,z}=50$ reduces these artifacts. The position curve becomes noticeably more linear, although small oscillations are still present. This indicates that the flame front is captured more consistently, but not yet with full accuracy. The velocity curve confirms this observation: while the fluctuations are less severe than at $N_{b,z}=10$, they are still too large to describe the expected smooth propagation of the laminar front. Similarly, the flame surface area converges to the correct cross-sectional value but with a delay compared to higher resolutions. Once convergence is reached, the curve remains relatively constant, although the transient behavior demonstrates that this resolution is still insufficient.

A further refinement to $N_{b,z} = 100$ produces a much more reliable description. The flame position evolves almost linearly in time until the front reaches the end of the domain, after which the curve becomes constant as no further propagation occurs. The velocity curve initially exhibits a very sharp increase. This behavior is not physical but results from the discrete computation of the derivative, where the displacement is divided by the first time interval. For this reason, the first instants of the simulation are not shown in the velocity plot, since they do not reflect the actual flame behavior. After this artificial transient, the velocity decreases smoothly as oxygen is progressively consumed in the unburnt mixture. A further increase in the velocity is observed near the end of the simulation. This is not related to a physical acceleration of the flame front, but to the setup of the case itself: the simulation is designed to reach a global equivalence ratio of $\Phi = 0.8$ at extinction, which implies that some particles are not fully oxidized when the flame dies out. If, in the final time steps, the average oxidant concentration in a grid cell falls below the threshold value, the marching cubes algorithm still detects iso-surface vertices. This results in an apparent front displacement and a spurious rise in the velocity, although no effective propagation takes place. The flame surface area at $N_{b,z} = 100$ converges almost immediately to the expected value and remains stable throughout most of the simulation. The sharp drop at the end corresponds to the complete consumption of the iron and the extinction of the flame.

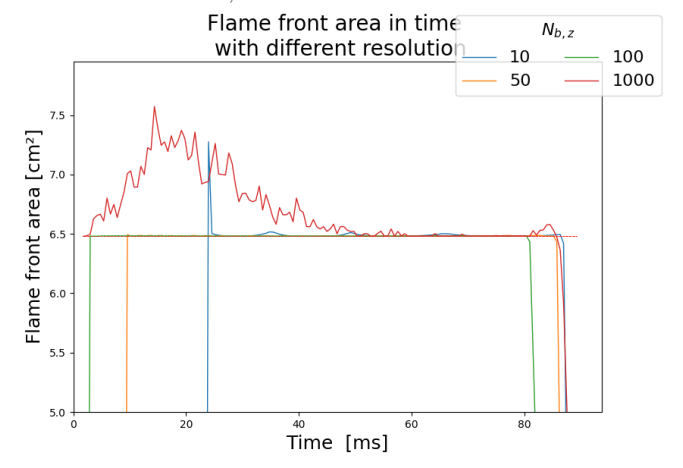
Further refinement to $N_{b,z} = 1000$ does not yield improvements. On the contrary, the box size becomes so small that each cell contains only a limited number of particles, and the MC algorithm reconstructs the interface with a large number of surfaces. As a result, the position curve develops irregular oscillations after an initially linear phase, and



(a) Evolution over time of the flame position along the z-direction evaluated with different $N_{b,z}$.



(b) Trend of the laminar flame speed S_L in time computed with different $N_{b,z}.$



(c) Evolution in time of the iso-surface representative of the flame area at different $N_{b,z}$.

Figure 4.7.: Laminar simulation setup: comparison of (a) flame position, (b) flame speed, and (c) flame surface area for different values of $N_{b,z}$, all at $C_{ox}^{level} = 0.5$.

the velocity signal is dominated by unrealistically high fluctuations. The surface area is heavily overestimated because the algorithm interprets weak gradients in the scalar field as multiple iso-surfaces, artificially wrinkling and corrugating the front. These effects are purely numerical artifacts, as the flame remains planar in reality.

From this analysis, a resolution of $N_{b,z} = 100$ emerges as the best compromise between computational cost and physical accuracy. Coarser grids fail to capture the continuous propagation of the front and introduce large numerical artifacts, while finer grids amplify noise and lead to an artificial overestimation of the flame surface. With $N_{b,z} = 100$, the algorithm provides a sufficiently accurate and physically consistent representation of the flame propagation, while keeping the computational effort manageable for the subsequent parametric analysis.

4.1.3. Iso-value C_{ox}^{level}

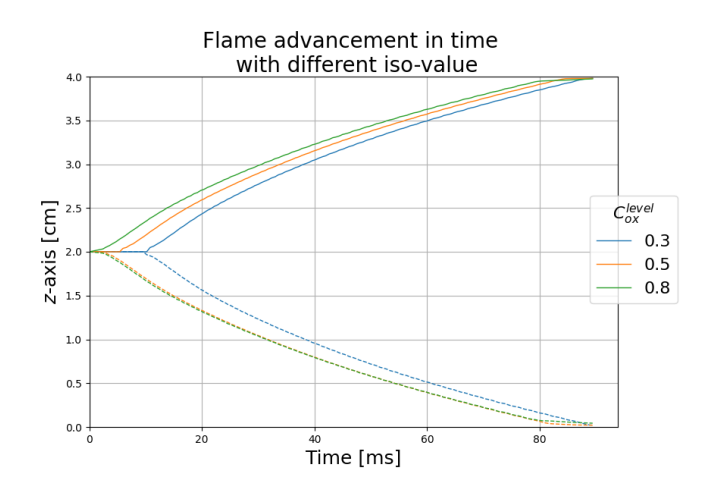
The second parameter investigated in the parametric analysis is the choice of the iso-value used in the MC algorithm. In this case, the algorithm is applied to the oxidation fraction volume data, and the threshold determines which grid values are selected to construct the flame surface, as described in Sec. 3.3.2. The choice of C_{ox}^{level} has a direct impact on the geometry of the reconstructed front: lower thresholds capture the earlier stages of oxidation, whereas higher thresholds identify regions closer to the fully oxidized products. Although its influence is less pronounced than that of the grid resolution, the iso-value remains crucial for the smoothness of the propagation curves and for the amplitude of the oscillations in the computed quantities.

Figure 4.8 compares the temporal evolution of three characteristic quantities for different iso-values at fixed resolution $N_{b,z} = 100$: the flame front position (4.8a), the instantaneous burning velocity (4.8b), and the flame surface area (4.8c).

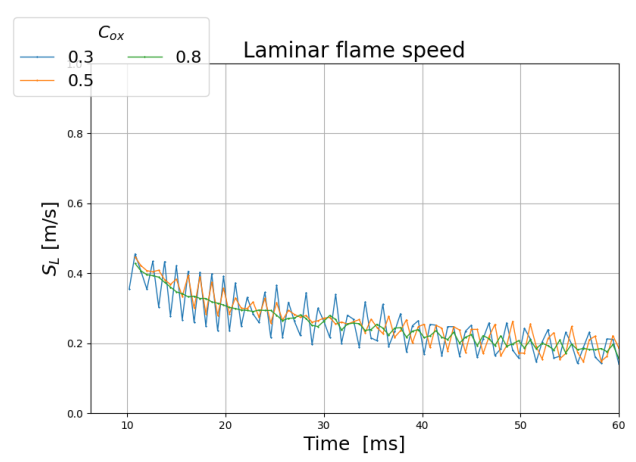
At $C_{ox}^{level} = 0.3$, the position curve is relatively smooth and almost linear, with only small deviations. The corresponding velocity shows a monotonic decay with limited oscillations, consistent with the expected behaviour of a laminar flame. The flame surface area converges quickly to the expected cross-sectional value $L_x L_y$, remaining stable until extinction. However, towards the end of the simulation some grid cells still contain particles with oxidation levels below the threshold, and the algorithm continues to detect isolated iso-surface vertices. This explains both the peak in the velocity curve and the delay of the surface area at extinction. It can also be noticed that the detection of the iso-surface is slightly delayed compared to higher thresholds, so that the position curve progresses with a small offset.

At $C_{ox}^{level}=0.5$, the behaviour improves further. The position curve is smooth and highly linear until the flame reaches the end of the domain. The velocity exhibits the initial artificial peak due to the discrete derivative definition, but then decreases monotonically with fewer oscillations than at 0.3. The flame surface area converges almost immediately and remains constant until extinction, with only a sharp drop at the end. This threshold therefore provides a robust and physically consistent representation of the front.

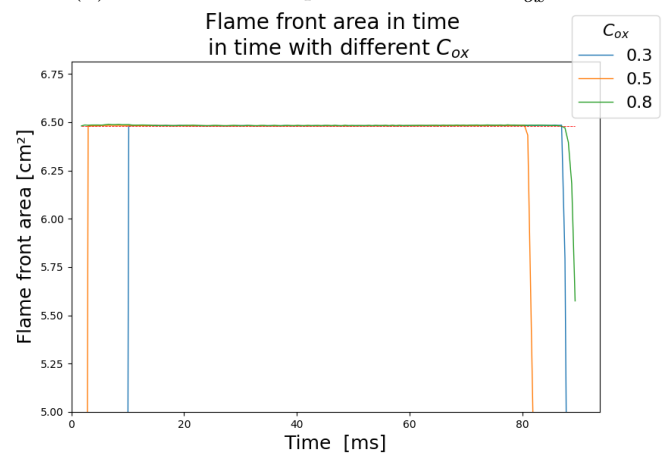
At $C_{ox}^{level} = 0.8$, the limitations of the method become more evident. The position curve still follows an approximately linear trend, but stronger local oscillations appear compared to lower thresholds. This is consistent with the fact that the iso-surface is defined deeper in the oxidized region, where steeper gradients and stronger local fluctuations are present. The velocity curve shows more pronounced oscillations, as any fluctuation in the detected position is amplified by the derivative operation. Similarly, the surface area is noisier



(a) Flame position over time at different C_{ox}^{level} with $N_{b,z} = 100$.



(b) Laminar flame speed at different C_{ox}^{level} .



(c) Flame surface area at different C_{ox}^{level} .

Figure 4.8.: Laminar simulation setup with $N_{b,z}=100$: comparison of (a) flame position, (b) flame speed, and (c) flame surface area for different values of C_{ox}^{level} .

and exhibits stronger oscillations, reflecting the irregular geometry reconstructed by the algorithm in these regions.

From these observations, an iso-value of $C_{ox}^{level}=0.5$ emerges as the most suitable choice. It minimizes oscillations, ensures rapid convergence of the surface area, and provides a smooth and linear description of the flame position. This result is consistent with the literature on premixed flames, where the progressive parameter is commonly adopted to identify the location of the laminar flame front, treated in Section 2.2.4.

4.1.4. Iso-value T^{level}

Although the oxidation fraction was ultimately selected as the most reliable progressive parameter, an additional analysis can be performed by evaluating the temperature volume data as input to the marching cubes algorithm. Following the classical analogy with premixed flames [15, 18, 29], a temperature-based progress variable is defined for each grid cell as

$$c_T^{(i,j,k)}(t) = \frac{\overline{T}^{(i,j,k)}(t) - T_u}{T_b - T_u},$$
(4.3)

where $T_u = 500 \,\mathrm{K}$ is the initial particle temperature and $T_b = 2150 \,\mathrm{K}$ is the peak particle temperature recorded during combustion in the laminar case setup. The marching cubes algorithm is then applied to this normalized temperature volume data.

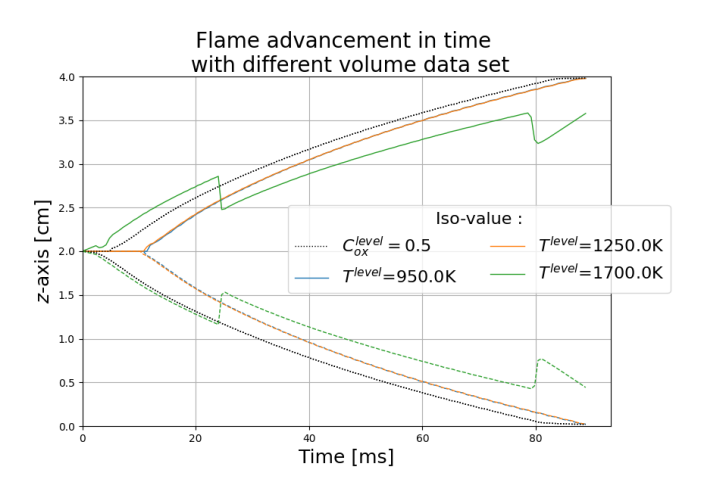
In analogy with the previous analysis on the oxidation fraction, a parametric loop is performed over the iso-value c_T^{level} . Three representative values are considered: $c_T^{level} = 0.3$, 0.5, and 0.8, which correspond to absolute temperature thresholds of approximately $T^{level} = 950 \,\mathrm{K}$, 1250 K, and 1700 K, respectively.

Figure 4.9 shows the results of this analysis: flame front position (4.9a), burning velocity (4.9b), and flame surface area (4.9c), obtained from the temperature-based definition. For direct comparison, the reference case with $C_{ox}^{level} = 0.5$ is also included in each plot.

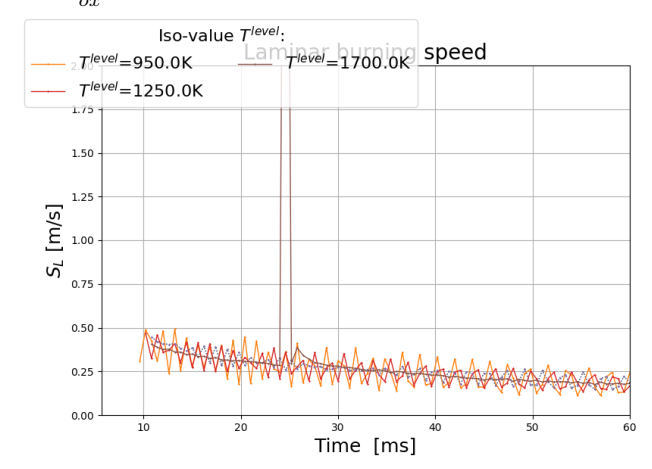
The results obtained with different temperature iso-values highlight distinct behaviors. When the threshold is set at $T^{level} = 950\,\mathrm{K}$, the flame position (Fig. 4.9a) evolves almost linearly and closely follows the curve at 1250 K, although residual oscillations are present. The corresponding velocity (Fig. 4.9b) shows slightly larger fluctuations than at 1250 K, reflecting a stronger sensitivity of the marching cubes reconstruction at lower thresholds. The surface area (Fig. 4.9c) converges with a short delay but then remains stable with negligible variability.

At the intermediate value of $T^{level}=1250\,\mathrm{K}$, which corresponds to $c_T^{level}=0.5$, the overall behavior is more consistent. The flame position is smooth and nearly linear, though oscillations remain visible and are particularly evident in the velocity signal. The surface area converges almost immediately to the cross-sectional value and remains close to it for the entire simulation. This case provides the most balanced outcome among the tested thresholds and is therefore chosen as the reference for comparison with the oxidation fraction.

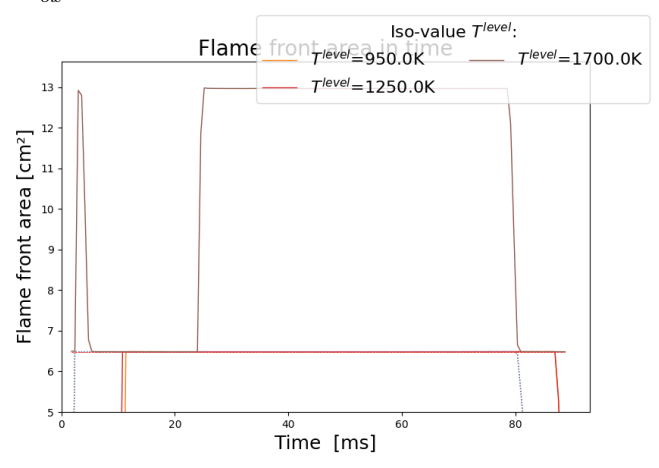
When the threshold is increased to $T^{level}=1700\,\mathrm{K}$, the reconstructed front exhibits clear discontinuities. In this case, the iso-surface is detected almost immediately, since particle temperatures rapidly exceed this value during the initial heating phase. Once ignition occurs, particles release heat to the fluid and subsequently cool down, leading to intermittent detection of the iso-surface. This produces piecewise linear behavior in the position curve, where long linear-like segments are divided by sharp discontinuities. The velocity signal mirrors this behavior, displaying strong peaks between otherwise smooth



(a) Flame position in time with $N_{b,z}=100,$ comparing $C_{ox}^{level}=0.5$ and different $T^{level}.$



(b) Flame speed in time with $N_{b,z}=100,$ comparing $C_{ox}^{level}=0.5$ and different $T^{level}.$



(c) Flame surface area in time with $N_{b,z}=100$, comparing $C_{ox}^{level}=0.5$ and different T^{level} .

Figure 4.9.: Laminar simulation setup with $N_{b,z}=100$: comparison of (a) flame position, (b) flame speed, and (c) flame surface area using either $C_{ox}^{level}=0.5$ or $T^{level}=950,\,1250\,\mathrm{or}\,1700\,\mathrm{K}.$

intervals. The surface area is strongly overestimated: marching cubes identifies multiple fragmented patches around the isotherm, leading to inflated and highly irregular values.

For direct comparison, Fig. 4.9 also includes the oxidation-based definition with $C_{ox}^{level}=0.5$ (dotted line). The temperature-based curves reproduce a similar global propagation, but systematic differences are evident. In particular, the position curve shows a small delay because marching cubes cannot detect edges that cross the threshold during the first steps of the simulation. The velocity is noisier, with stronger oscillations, and the surface area converges less smoothly. Overall, while the intermediate threshold at $T^{level}=1250\,\mathrm{K}$ provides the most consistent description among the temperature cases, the oxidation fraction remains the more robust and physically reliable definition of the flame front.

4.2. Comparing different simulation setups: one-direction propagating flames

In this section, different simulations of one-direction propagating flames are compared. Two aspects are examined: the sensitivity of the post-processing analysis to the number of particles in the domain, and the possible correlation between the flame structure and turbulence intensity. The key parameters that are varied are:

- the equivalence ratio Φ , which determines the number of particles in the domain;
- the Stokes number St, which controls the input dissipation energy of the turbulent flow.

Each parameter is varied individually while keeping the rest of the setup unchanged. The equivalence ratio is reduced to assess the dependence of accuracy on the particle count, while the Stokes number is increased to investigate the influence of turbulence on the flame structure and for a direct comparison to the studied high turbulent premixed flame.

4.2.1. Different N_{part}

In this subsection, two simulations with identical setups but different numbers of particles are compared, with N_{part} computed according to Eq. 3.7. The objective is to assess how the marching cubes (MC) algorithm responds to different particle densities. Although the algorithm processes scalar values on a fixed grid, the local particle density directly affects the averaged box quantities, and thus indirectly the accuracy of the reconstructed iso-surface.

This is a common issue in particle-based simulations: when the distribution of particles is not uniform, the averaged values assigned to neighboring boxes may exhibit artificial gradients. The consequence is that the reconstructed iso-surface becomes more sensitive to statistical fluctuations rather than reflecting the underlying flame structure.

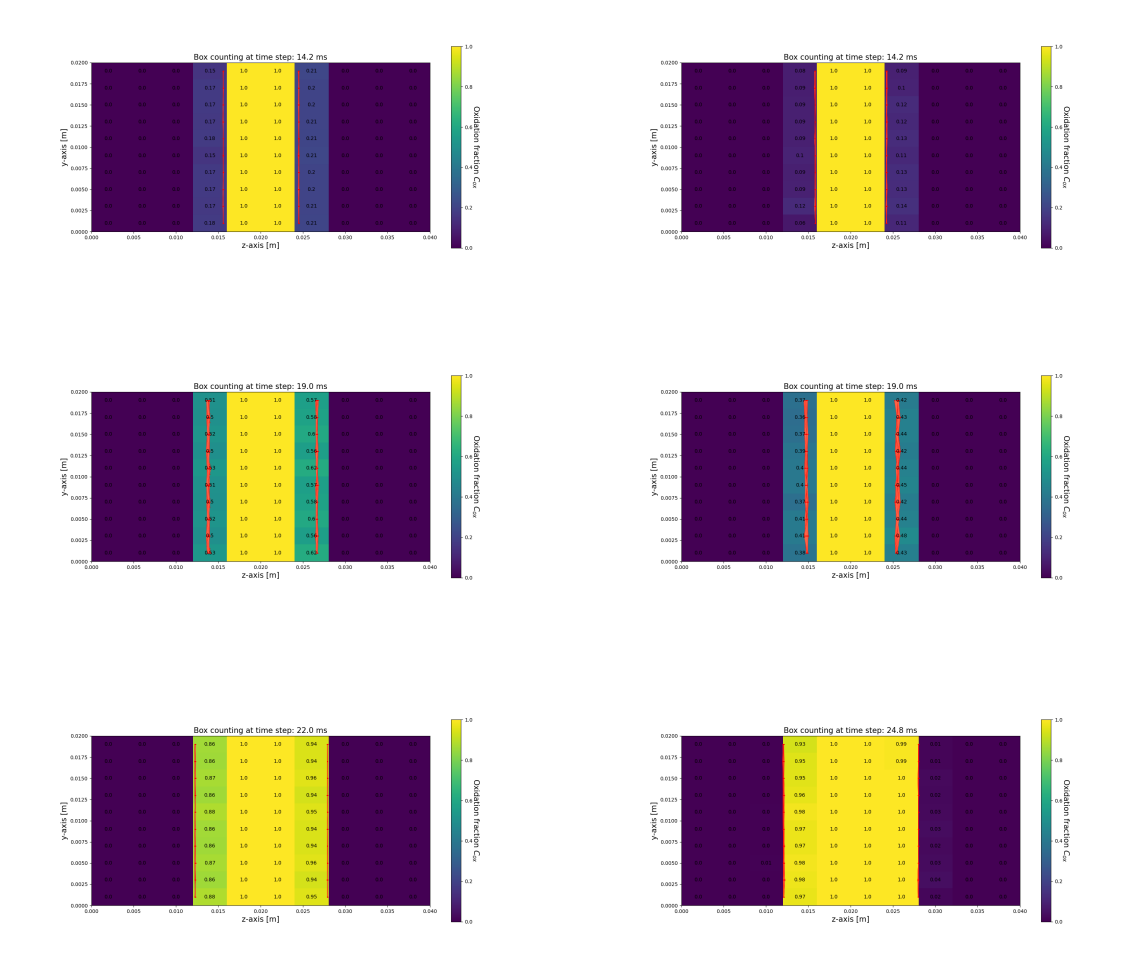
The input data of the two simulations are reported in Table 4.1 together with the averge number of vertices and faces found by the MC algorithm.

	Φ_{obb}	N_{part}	\overline{N}_{verts}	\overline{N}_{faces}
Simulation (a)	0.8	1768667	203	330
Simulation (b)	0.5	1105417	204	484

Table 4.1.: Calculation of the input quantities N_{part} and H_{in} .

The effect of particle distribution is evident. With a higher particle density (simulation \mathbf{a}), and despite the relatively fine grid resolution, boxes partially crossed by the flame front often contain fewer particles than their neighbors. This introduces strong local gradients, which are further amplified when fluid motion causes particle clustering, enhancing variability between adjacent boxes.

Conversely, in the case with fewer particles (simulation **b**), gradients between neighboring boxes appear less steep, especially under laminar conditions. As a result, the reconstructed flame front seems smoother in terms of position and velocity. At first glance this may appear advantageous; however, closer inspection of the MC output reveals that the reconstructed surface is less representative of the actual flame dynamics. With fewer particles per box, the algorithm generates a larger number of small triangular facets, producing artificial wrinkling of the iso-surface. This contradicts the expected smooth planar structure of the laminar flame.



Simulation (a): transition inside a box of the front detected with MC.

Simulation (b): transition inside a box of the front detected with MC.

Figure 4.10.: Transition inside a box of the flame position. A resolution of $N_{b,z} = 10$ and a threshold value $C_{ox}^{level} = 0.5$ are used.

A complementary statistical comparison is reported in Fig. 4.11. Here the instantaneous burning speed for the same box transition is shown together with a moving average and the corresponding fluctuation band $(\pm 1\sigma)$. The results highlight that, although

both simulations follow the same overall trend, the case with fewer particles exhibits smoother curves but larger fluctuations around the mean. This indicates that apparent smoothness in the position plot does not necessarily correspond to a more reliable iso-surface reconstruction; rather, it may hide stronger local variability at the cell level.

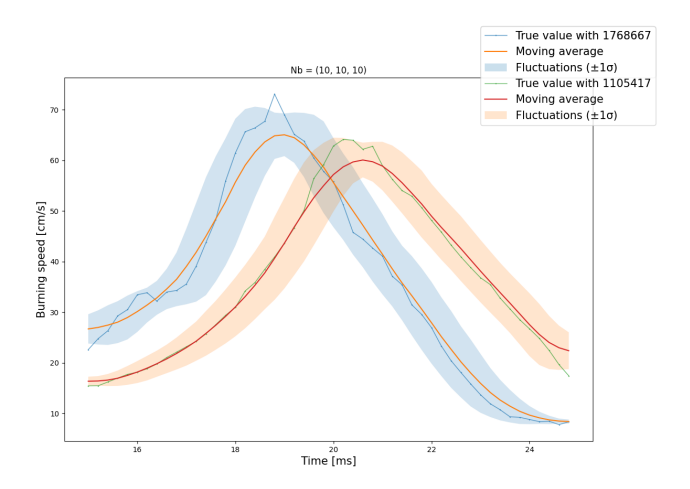


Figure 4.11.: Flame front speed in time for two different simulations, respectively at $\Phi = 0.8$ and $\Phi = 0.5$. A resolution of $N_{b,z} = 10$ and a threshold value $C_{ox}^{level} = 0.5$ are used.

In conclusion, a higher particle count per box leads to a more reliable detection of the laminar flame front. While simulations with fewer particles may produce apparently smoother velocity—time profiles, the underlying iso-surface reconstruction is less representative of the physical flame structure. Therefore, higher particle counts remain essential for accurately capturing the homogeneous flame propagation along the z-direction.

4.2.2. Different ϵ : relation between flame speed and flame surface

This subsection investigates whether a relationship exists between flame speed and flame surface in the presence of turbulence. Insights from the literature on hydrocarbon flames [14, 29] and hydrogen premixed flames [17, 18] indicate that no universal correlation applies across all turbulence scales. For this reason, different turbulent intensities were analyzed. The Stokes number, which controls the input dissipation energy of the flow, was varied across three simulations.

It must be noted that the plots shown here are results got with a partially not correct simulation setup due to a too small frig refinement. Yet their utility in the discussion is still valid since they represent the expected behavior with the turbulence increase.

	St	Re_T	Re_{λ}	l	η	u'
Simulation (A)	1	19.4	1.31	0.0042	0.0011	0.325
Simulation (B)	3	80.1	66.3	0.0043	0.0034	0.72
Simulation (C)	5	87.5	70.8	0.0043	0.0035	0.80

Table 4.2.: Turbulent properties at the initial step for the three simulations considered.

To analyze the turbulent flame behavior, several variables must first be defined. The turbulent burning velocity, S_T , is commonly defined in premixed flames as the local displacement burning speed defined by Eqn.(2.6) and here reported:

$$S_T \equiv S_{T,LD} = (\mathbf{V}_{Flame} - \mathbf{V}_{Gas})_{LE} \cdot \mathbf{n}_{LE},$$

where the subscript LE refers to the leading edge of the flame brush, identified as the location where the progress variable reaches 0.5. In premixed flames, this definition is often adopted for comparison with turbulence [17]. In our case, S_T is computed following the methodology described in Section 3.3.2, namely as the displacement of the weighted centroid of the triangular facets forming the iso-surface at $C_{ox}^{level} = 0.5$. This ensures consistency with the flame front reconstruction method. A similarity can thus be drawn with the premixed case, since both approaches rely on the iso-surface at $C_{ox}^{level} = 0.5$ as a reference for the flame position.

In counter-flow flames, Driscoll [14] notes that $\mathbf{V}_{Flame} \simeq 0$, so the burning speed can be approximated from the incoming gas velocity \mathbf{V}_{Gas} . This assumption does not hold here, since the flow consists of a turbulent carrier phase and a dispersed phase of inertial reactive particles, which do not perfectly follow the fluid motion. In this configuration, the difference between gas velocity and flame velocity becomes significant: the flame speed is influenced by particle inertia, while the gas velocity is governed by the turbulent eddies. In the analysis on iron flames, this is resolved by using the particles coordinates. The simulation itself takes into account for this slip-velcity between the fluid and the particles so in the post-processing based it is not necessary to account for the gas field. Consequently, the turbulent flame speed is computed as the temporal advancement of the iso-surface at $C_{ox}^{level} = 0.5$, detected via the marching cubes algorithm, assuming initially quiescent particles.

Although a time-averaged laminar speed S_L , as the reference one in the premixed flames, could be computed using the same procedure for the laminar setup, this quantity exhibits strong fluctuations. For this reason, the unwrinkled flame speed is here calculated as the velocity the flame would advance if a linear propagation from the center of the domain, where ignition starts, to the end of the domain, i.e. L_z for the positive-propagating front and the origin (z = 0) for the negative one, by the end of the simulation interval of time.

The temporal evolution of both the normalized turbulent flame speed S_T/S_L and the normalized flame surface A_T/A_L is reported in Fig. 4.12, plotted against the simulation time normalized by the eddy timescale $\tau_{eddy} = \eta/u'$. These two quantities are widely employed in premixed combustion studies to assess the link between flame structure and propagation rate. According to classical flamelet theory, a proportionality between S_T/S_L and A_T/A_L can be expected in the thin-reaction-zone and corrugated-flamelet regimes, since the increase in propagation speed is directly related to the enlargement of the flame surface [14].

At low turbulence intensity, St = 1 (Fig.4.12a), the normalized turbulent flame velocity S_T/S_L fluctuates around a nearly constant mean value, while the normalized flame surface A_T/A_L exhibits a steadily increasing trend over time. This indicates that the flame front quickly reaches a quasi-stationary propagation speed, but its surface continues to wrinkle and fold under the action of turbulent eddies. The lack of convergence between S_T/S_L and A_T/A_L suggests that, at this turbulence level, geometric wrinkling persists beyond the stabilization of the burning velocity, delaying the proportionality typically observed in premixed flames.

At intermediate turbulence, St = 3 (Fig. 4.12b), the behavior is more consistent with flamelet theory. Both S_T/S_L and A_T/A_L exhibit an initial transient phase marked by a strong rise, followed by a quasi-steady regime where the two quantities fluctuate around comparable values. Although perfect overlap is not achieved, their correlated evolution supports the hypothesis that turbulent velocity enhancement is primarily governed by the

increase in flame surface area. This scenario resembles the corrugated-flamelet regime known from premixed flames, where large-scale eddies wrinkle the flame front but do not penetrate the reaction zone.

At high turbulence intensity St = 5 (Fig. 4.12c), the proportionality between S_T/S_L and A_T/A_L breaks down. The flame surface initially grows rapidly but soon stabilizes at an approximately constant value. In contrast, S_T/S_L continues to rise with pronounced fluctuations, indicating that other mechanisms, beyond surface wrinkling, dominate the flame propagation. This behavior reflects the transition toward a broadened-reaction-zone regime, where enhanced mixing and particle-fluid interactions increasingly control the burning velocity. The strong variability of S_T/S_L further underlines the sensitivity of the flame front to turbulent eddy interactions at this regime.

An additional analysis was performed to compare the simulations against the Damköhler prediction, as introduced in Section 2.2. In this analysis, the ratio between the dimensionless turbulent burning velocity and the normalized flame surface area, $\frac{S_T/S_L}{A_T/A_L}$, was evaluated over time. Figure 4.13 reports this ratio with the simulation time step on the abscissa, while the ordinate shows its instantaneous value. The dashed blue line represents Damköhler's original prediction for premixed flames [21], according to which the turbulent burning velocity scales linearly with the wrinkled flame surface area.

In premixed combustion, this proportionality has often been verified experimentally, although not exactly equal to unity. A correction factor, referred to as a stretch factor or Bray-Cant parameter [57], is typically introduced. More recent extensions of Damköhler's theory [57, 58] interpret this correction as a flame wrinkling parameter, I_0 , which accounts for deviations from the ideal linear scaling. Importantly, I_0 is not constant in time, as shown also in hydrogen flame modeling studies [17], since several unsteady processes such as flame stretch, local extinction, and re-ignition contribute to turbulent flame dynamics.

The simulations presented here show that the validity of Damköhler scaling strongly depends on the turbulence intensity. For St=1, the ratio fluctuates around a stable mean slightly below unity, indicating that the flame speed is largely governed by surface wrinkling, although the geometric effect contributes more strongly than direct propagation. At St=3, the fluctuations are reduced and the ratio remains close to the Damköhler line, suggesting that the balance between surface wrinkling and turbulent transport is consistent with the corrugated-flamelet regime. In contrast, the case at St=5 diverges rapidly after the initial transient: the ratio increases significantly above unity with pronounced oscillations, showing that at high turbulence intensities the turbulent burning velocity decouples from the flame surface area. In this regime, additional mechanisms such as turbulent mixing, particle–fluid momentum exchange, and local quenching dominate the flame dynamics.

These observations indicate that Damköhler's proportionality provides a good approximation only at moderate turbulence intensities, whereas at high turbulence levels its validity breaks down, in agreement with the general findings from premixed flame studies.

Another analysis has been carried out to characterize the flame structure through its geometric thickness. The definition of this quantity is widely discussed in the literature, as reported in Section 2.2. In the present study, two approaches were tested, with detailed results provided in Appendix C.2. The first approach, based on the distance between the most advanced and the most retarded flame-front vertices along z, is meaningful only for strictly planar flames propagating homogeneously in one direction and was therefore discarded here. Instead, the following definition, already employed in the literature [18], was adopted.

The instantaneous flame thickness is defined as

$$\delta_L = \frac{C_{ox,b} - C_{ox,u}}{(\partial C_{ox}/\partial z)|_{max}} = \left(\frac{\partial C_{ox}}{\partial z}|_{max}\right)^{-1}.$$
(4.4)

The maximum gradient of C_{ox} is estimated from the standard deviation of the oxidation fraction of the particles within each box, normalized by the box length in the z direction, $L_{b,z}$. The standard deviation is defined as

$$\sigma_{ox}^{i,j,k} = \sqrt{\frac{\sum_{p}^{N_{part}^{i,j,k}} (C_p^{i,j,k} - \overline{C}^{i,j,k})^2}{N_{part}^{i,j,k}}},$$
(4.5)

which is nonzero only in boxes partially traversed by the flame front, where $0 < \overline{C}^{i,j,k} < 1$.

The flame thickness plays a central role in diagrams such as the Borghi–Williams diagram [18, 30, 39], which are commonly used to represent how turbulence modifies flame regimes. Figure 4.14 shows a reconstruction of the Borghi–Williams diagram adapted to the present case. The horizontal axis reports the integral turbulent length scale normalized by the flame thickness, L_T/δ_L , while the vertical axis reports the normalized turbulent intensity, u'/S_L .

This framework highlights the competing influence of turbulence and chemistry: the scale ratio L_T/δ_L expresses the relative size of eddies compared to the flame thickness, while the velocity ratio u'/S_L compares turbulent fluctuations to the laminar flame speed. The three markers represent the time-averaged values of L_T/δ_L and u'/S_L . It should also be noted that in this plot l_x denotes the turbulent integral length scale, while $\delta_{L,P}$ represents the laminar flame thickness as defined according to Peters.

For iron flames, comparing these quantities also implicitly compares fluid properties to particle-related properties, and this must be interpreted with caution. The turbulent integral length scale L_T and the rms turbulent velocity fluctuations u' are properties of the carrier flow. In contrast, δ_L is computed as in Eq. 4.4 and is therefore related to particle oxidation values with respect to grid quantities (i.e., box length and box-averaged values). The laminar flame speed S_L , on the other hand, is independent of both the fluid and the particles, since it is derived from the geometric properties of the simulation domain.

The information provided by this plot is therefore mainly qualitative compared to the plots 3.2. All simulations fall within the corrugated-flamelet regime. In particular, the case at St=1 lies closer to the Reynolds boundary limit: the flame is thicker than the turbulence length scale, and the turbulent intensity is only slightly higher than the laminar flame speed. The case at St=3 shows a higher ratio of turbulent length scale to flame thickness, resulting in a more broadened flame, closer to the Damköhler limit. Finally, the case at St=5 exhibits a flame thickness comparable to the turbulent length scale, but with turbulent intensities clearly exceeding the laminar flame speed. This suggests that the flow evolves faster than the chemistry, which can also be visualized in Fig. 3.2c, where clusters of burning particles are distributed across the domain.

Table 4.3 reports the corresponding quantities for the three simulations. It can be seen that while the normalized turbulent intensity u'/S_L increases with St, the scale ratio L_T/δ_L does not follow a monotonic trend. In fact, the case at St=5 shows a slightly smaller L_T/δ_L than St=3. This may be explained either by enhanced dissipation producing smaller eddies, or by a thickening of the flame front itself. The latter interpretation is supported by the ratios L_z/δ_L and $\delta_L/L_{b,z}$: in the St=3 case the flame is thinner relative to the box length, while for St=5 it is thicker. At the lowest turbulence intensity (St=1), the

	St	u'/S_L	L_T/δ_L	L_z/δ_L	$\delta_L/L_{b,z}$
Simulation (A)	1	0.01	14.5	136	0.7
Simulation (B)	3	0.7	10.2	97.2	1.0
Simulation (C)	5	0.8	10.3	96.6	1.0

Table 4.3.: Parameters of simulations at initial time step at P = 1 atm, $T_u = 500$ K, and $\Phi = 0.8$, under the grid system $N_b = (10, 10, 100)$.

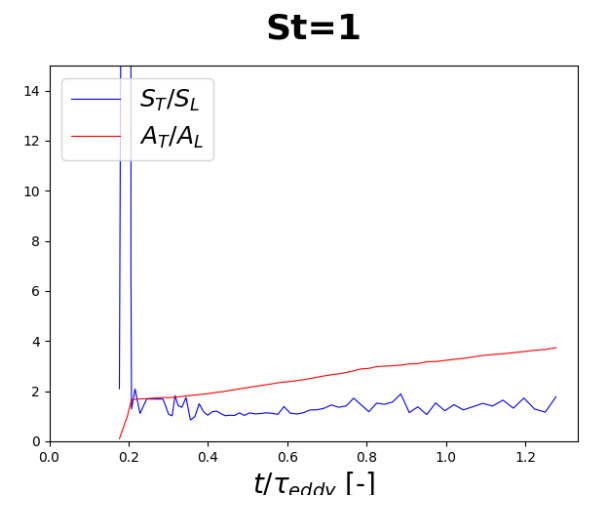
ratios show the extreme values of the trend, confirming that flame thickness first decreases with turbulence and then increases again at higher intensity.

A complementary view is provided by the dimensionless numbers in Table 4.4. Here, Ka_{δ} has been computed according to Eqn. (2.3), while Re_{δ} and Da_{δ} follow the definitions in Eqs. 2.11. The results confirm that all cases fall within the turbulent regime ($Re_{\delta} \gg 1$). All the three simulations fall in the flamelet regime with $Ka_{\delta} < 1$.

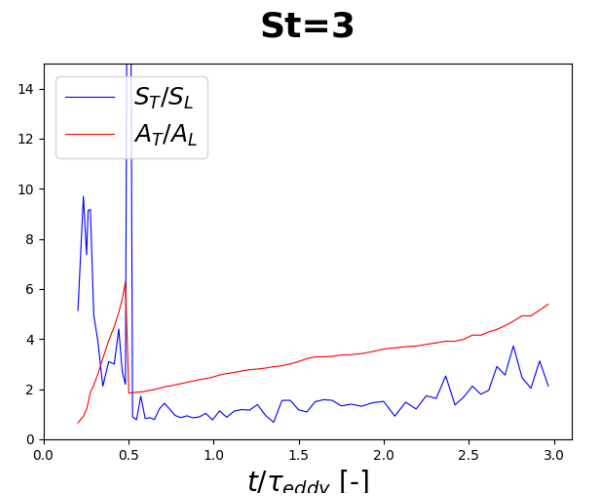
	St	Re_{δ}	Da_{δ}	Ka_{δ}
Simulation (A)	1	12.5	9	0.05
Simulation (B)	3	12.0	8.7	0.3
Simulation (C)	5	13.8	7.7	0.2

Table 4.4.: Dimensionless numbers at initial time step for the three simulations at P=1 atm, $T_u=500$ K, and $\Phi=0.8$, under the grid system $N_b=(10,10,100)$.

Overall, these results show that although iron flames do not strictly obey the scaling relations established for premixed flames, qualitative similarities can still be identified. In particular, the variation of flame thickness with turbulence intensity and the classification of regimes in the Borghi–Williams diagram reflect trends known from hydrocarbon and hydrogen premixed flames. A noteworthy aspect is the behavior of the St=1 case: if the mean values are computed including the initial transient steps where the flame is still under development, a shift towards the broadened region is expected. This sensitivity to the treatment of transients is consistent with observations reported in premixed flame studies [14, 29], where the early nonstationary phase strongly affects the classification in such diagrams.



(a) Turbulent simulation at Stokes number St = 1.



(b) Turbulent simulation at Stokes number St = 3.

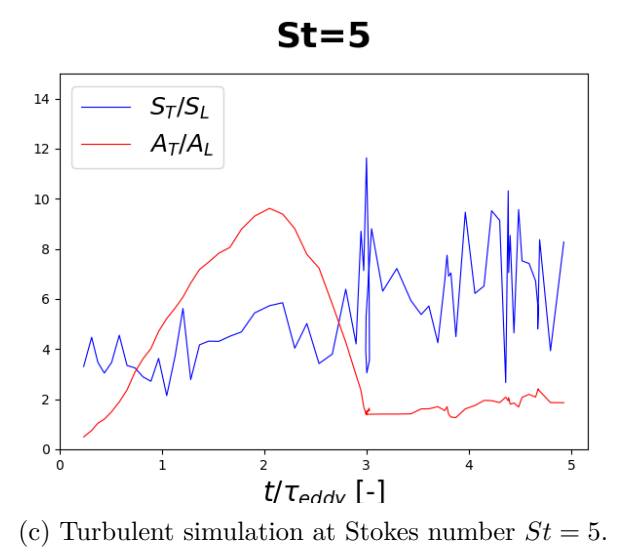


Figure 4.12.: Normalized flame surface area A_T/A_L and turbulent burning speed $S_T/S_{L,0}$ over time, for three turbulent simulations at increasing Stokes numbers. The x-axis represents the simulation time normalized by the eddy time scale $\tau_{\rm eddy}$.

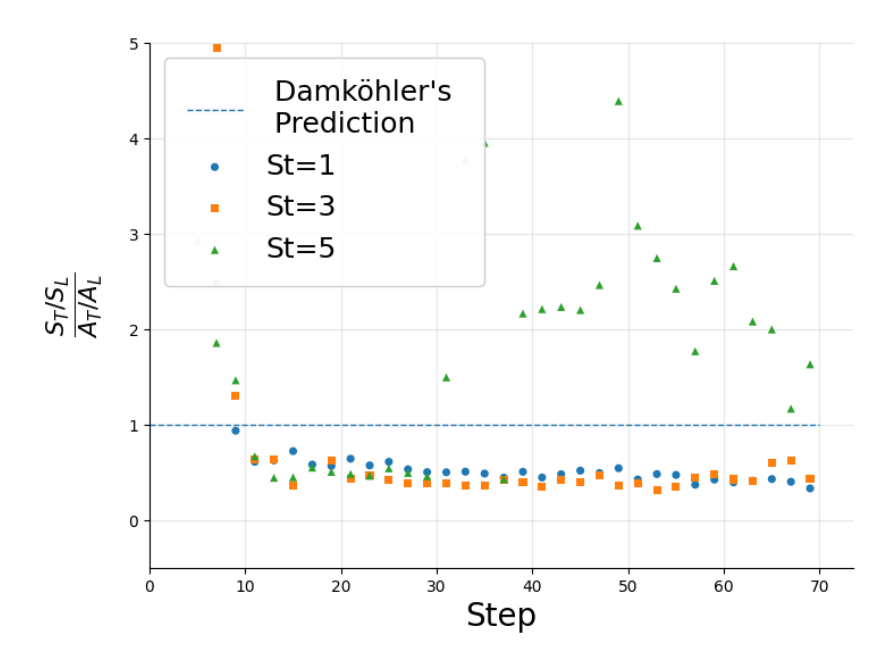


Figure 4.13.: Ratio $(S_T/S_L)/(A_T/A_L)$ plotted over simulation time step. The dashed line represents Damköhler's prediction for premixed flames.

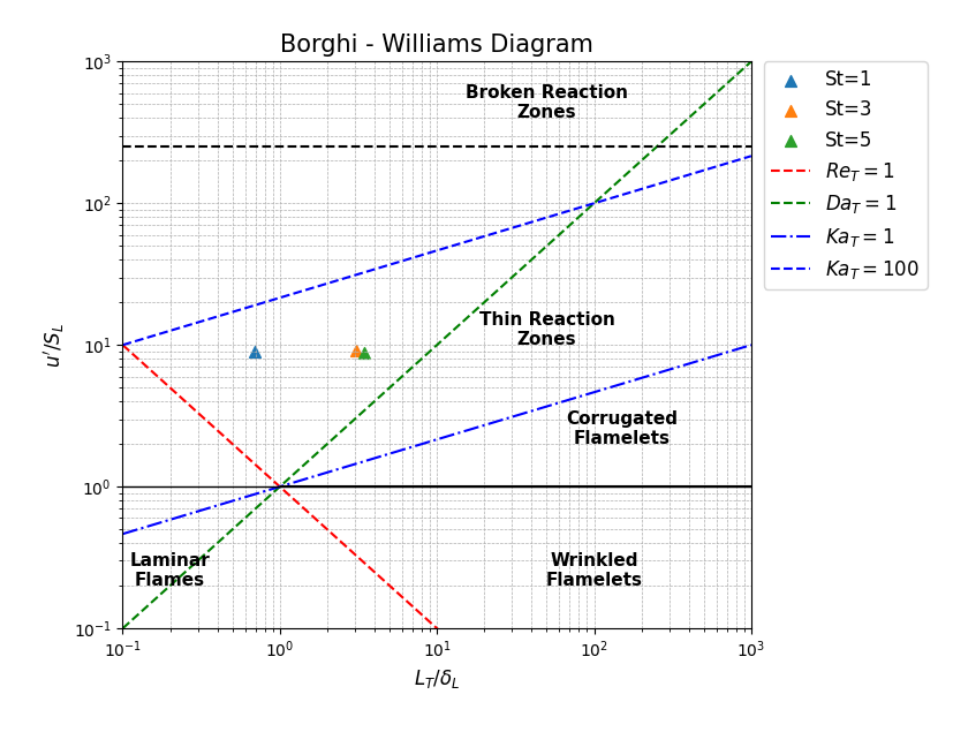


Figure 4.14.: Borghi–Williams diagram reconstructed from [39]. Each marker corresponds to the mean value over the first ten simulation steps for the three cases at different Stokes numbers.

5. Conclusion

This thesis has addressed the challenge of extending classical premixed-flame theory to the heterogeneous case of iron particle clouds, with particular attention to the correlation between turbulent flame propagation speed and flame surface area. The motivation stemmed from the need to understand whether the well-established frameworks developed for gaseous premixed flames can be applied, or at least adapted, to heterogeneous combustion systems that are of increasing relevance in energy applications. The first question concerned the applicability of premixed-flame theories to heterogeneous particle-cloud combustion. The results show that the general trend observed in gaseous flames, namely that turbulent flame speed scales with the increase of flame surface area, can indeed be extended to iron flames under moderate turbulence. At low Stokes numbers, the Damköhler relation was approximately verified, with a proportionality factor below unity, which can be interpreted in analogy with the Bray-Cant stretching factor. However, at higher turbulence intensities this correlation breaks down, as the burning velocity rises more steeply than the flame area. This behavior mirrors observations in gaseous premixed flames, where at sufficiently high Karlovitz numbers the simple surface-based scaling ceases to hold.

The second question focused on how established models should be modified to reflect the heterogeneous nature of iron flames. Here, the analogy with premixed flames holds only for the gas-phase preheat zone, which behaves in a comparable way and responds strongly to turbulence. By contrast, the reaction layer is located at particle surfaces and is controlled by oxide formation and surface kinetics rather than by molecular transport. This duality means that models built for gaseous flames cannot be transferred directly but require new terms to capture the coupling between particle-scale reactions and the surrounding gas flow.

The third question addressed how the flame front can be consistently defined in iron particle-cloud simulations. A robust procedure was developed based on Voronoi-weighted remapping of particle data followed by iso-surface reconstruction using the Marching Cubes algorithm. The parametric analysis for laminar iron flames showed that selecting the oxidation fraction threshold at $C_{ox}^{level} = 0.5$ and adopting a resolution of 100 boxes along the propagation direction provided the most consistent results, characterized by linear position—time curves, rapid convergence of the flame surface, and relatively stable velocity values. Nevertheless, this approach presents some limitations. The accuracy of the reconstruction remains sensitive to the local distribution of particles, and in particular, in cells partially crossed by the flame front the not uniform particles distribution induced by fluid expansion may produce under-sampling and introduce bias, even when Voronoi weighting is used. The choice of resolution also represents a delicate trade-off: low resolution grids tend to wrinkle the front and generate artificial jumps in propagation, while overly fine grids amplify numerical noise and lead to fragmented iso-surfaces and overestimation of the flame area due to spurious corrugations. Furthermore, the adoption of $C_{ox}^{level} = 0.5$, although consistent with the literature on premixed flames, remains a conventional choice that may not fully capture the complexity of heterogeneous flames, where a gaseous preheat region coexists with surface oxidation processes. In summary, the proposed method provides a solid basis for the definition of the flame front and allows coherent comparisons across cases, but its numerical and conceptual limitations must be carefully considered when aiming at quantitative analysis or extensions to more complex turbulent configurations.

The fourth question asked how turbulence intensity modifies flame propagation and internal structure in iron combustion. The analysis revealed that turbulence primarily broadens the gas-phase preheat layer through enhanced transport, while the particle-bound reaction layer remains governed by local kinetics and oxide growth. At moderate turbulence levels this broadening increases the effective burning velocity by accelerating ignition and sustaining front propagation. At higher intensities, however, the direct correlation between flame surface and burning velocity no longer holds, as transport-driven effects dominate and fluctuations lead to irregular flame dynamics. These findings were further analyzed within the framework of classical premixed-flame diagrams, such as the Borghi-Williams representation. While the exact scaling laws are not directly applicable, qualitative similarities were observed, particularly in the sensitivity of flame thickness to turbulence and in the classification of different regimes. The allocation of the simulations in diagram such as the Borghi-Williams strongly depends on the transient considered. This sensitivity recalls similar behavior documented in premixed-flame literature, where the early nonstationary phase can significantly affect classification in turbulence-flame interaction diagrams.

Overall, the study demonstrates both the opportunities and the limits of extending premixed-flame theory to heterogeneous combustion. While the analogy offers useful insights, especially at moderate turbulence intensities, a complete description of iron flames requires models that explicitly account for their heterogeneous nature. The comparison with premixed flames shows that turbulence acts on the gas-phase preheat region in broadly similar ways, enhancing transport and broadening the thermal layer, but the particle-surface reaction zone remains fundamentally different. Extinction phenomena typical of premixed systems are absent, and instead local suppression arises from oxygen depletion or heat-loss effects. This duality underscores the need for dedicated modeling approaches. Nevertheless, the parallels identified here suggest that heterogeneous flames share some features with gaseous premixed systems, especially regarding the role of turbulence in controlling front broadening and in shaping the global burning velocity.

List of Figures

1.1.	Volumetric and gravimetric energy densities of possible metal fuels, coal, ammonia and hydrogen reprinted from [6]	2
1.2.	Schematic of an iron reduction–oxidation cycle for a $\rm CO_2$ -free energy supply . Reprinted from [10]	4
2.1.	Laminar case: premixed and diffusive flames. Reprinted from [22]	5
2.2.	Template for 1D laminar premixed flame profiles (temperature T , reactant mass fraction Y_{fuel} , oxidizer mass fraction $Y_{oxidizer}$, reaction rate). Reprinted	
2.3.	from [25]	6
	from [14]	8
2.4.	Schematic flamelet structures for hydrocarbons flame. Reprinted from [14] .	9
2.5.	Estimation of the flame surface density (FSD) in three-dimensional space. Reprinted from [36]	11
2.6.	Turbulent burning velocity over laminar burning velocity plotted against	
	the root-mean-square of flow velocity fluctuations in extreme turbulence [29]	13
2.7.	Schematic of the wrinkled flame area (A_T) compared to the $\bar{c} = 0.5$ isosurface area (A_L) . Also shown are the flamelet consumption speed $(S_{F,C})$	1.4
20	and turbulent brush local consumption speed $(S_{T,LC})$. Reprinted from [14]	14
2.8.2.9.	Borghi diagram adapted from [39]	16
	one on the bottom illustrates the transition to thin and broken reaction zones. $$	17
2.10.	Flame surface density measured in Bunsen flames, plotted against the mean progress variable. Reprinted from [14]	18
	progress variable. Reprinted from [11]	10
3.1. 3.2.	Instantaneous $y-z$ slices of laminar case at $t=15$ ms	25
3.3.	iron consumption and extended oxygen depletion	26
	(PLIC), in which segments can be arbitrarily oriented, yielding a sharper	
	and more accurate representation. Reprinted from [45]	28
3.4.	Type of surface combinations for the Marching Cubes algorithm. The black circles mean that the vertices inside the surface. Reprinted from [51]	30
3.5.	Grid arrangement. Yellow points denote the midpoint of each edge. The vertex will be highlighted if it receives a binary one. Printed from [51]	30

3.6.	Three-dimensional plots of the iso-surfaces reconstructed with the Marching Cubes algorithm in laminar and turbulent conditions. Additional plots are reported in C.3	32
3.7.	Laminar flame speed for the simulation case with $N_b = (10, 10, 100)$	33
4.1.	Comparison between the flame position computed with the isothermal approach (red curve) and with the oxidation fraction values at the nodes of the grid, computed either as the mean value (black curve) either as the Voronoi volumes weighted average (blue curve). An uniform number of boxes of 10 is here selected in all directions	36
4.2.	Random reproduced data to evidence the issue with box -counting. On the abscissa is plotted the z -axis, i.e. direction of propagation of the front, positive towards right, and on the ordinate the y -axis	37
4.3.	Comparison of the laminar simulation setup: (a) MC reconstruction, (b) expected result from Voronoi averaging	38
4.4.	Laminar setup: $z-y$ slice at $x=0$ after $t=75$ ms. The red line is the flame front at $C_{ox}^{level}=0.5$, grid $N_b=(10,10,100)$	40
4.5.	Turbulent setup at $St = 1$: $z-y$ slice at $x = 0$ after $t = 75$ ms. The red surface is the flame front at $C_{ox}^{level} = 0.5$, grid $N_b = (10, 10, 100)$	41
	Flame position over time for different values of N_b , all at $C_{ox}^{level} = 0.5$. In particular an uniform grid is used here in all directions	42
	Laminar simulation setup: comparison of (a) flame position, (b) flame speed, and (c) flame surface area for different values of $N_{b,z}$, all at $C_{ox}^{level} = 0.5$	44
4.8.	Laminar simulation setup with $N_{b,z} = 100$: comparison of (a) flame position, (b) flame speed, and (c) flame surface area for different values of C_{ox}^{level}	46
4.9.	Laminar simulation setup with $N_{b,z} = 100$: comparison of (a) flame position, (b) flame speed, and (c) flame surface area using either $C_{ox}^{level} = 0.5$ or $T^{level} = 950, 1250 \text{ or } 1700 \text{ K}. \dots \dots$	48
4.10.	Transition inside a box of the flame position. A resolution of $N_{b,z}=10$ and a threshold value $C_{ox}^{level}=0.5$ are used	50
4.11.	Flame front speed in time for two different simulations, respectively at $\Phi = 0.8$ and $\Phi = 0.5$. A resolution of $N_{b,z} = 10$ and a threshold value $C_{ox}^{level} = 0.5$ are used	51
4.12.	Normalized flame surface area A_T/A_L and turbulent burning speed $S_T/S_{L,0}$ over time, for three turbulent simulations at increasing Stokes numbers. The	
4.13.	x -axis represents the simulation time normalized by the eddy time scale $\tau_{\rm eddy}$. Ratio $(S_T/S_L)/(A_T/A_L)$ plotted over simulation time step. The dashed line	
4.14.	represents Damköhler's prediction for premixed flames	57
	to the mean value over the first ten simulation steps for the three cases at different Stokes numbers	57
C.1.	Flame position over time computed as the fluid iso-thermal curves at different temperature	75
	Laminar flame speed over time computed with the iso-l line Laminar case of simulation setup with $\Phi=0.5$. Flame position evolution in time with isothermal, mean value and weighted average approach. Resolution	75
C.4.	of $N_{b,z} = 10$ and $C_{ox}^{level} = 0.5$	76
C.5.	and $C_{ox}^{level} = 0.5$	76
	grid $N_b = (10, 10, 100)$	77

C.6.	Turbulent of	case at $St = 5$: reconstructed	iso-surface at	$C_{ox}^{level} = 0.5$ with a	\mathbf{a}
	grid $N_b = ($	(10, 10, 100).				78

List of Tables

1.1.	Properties of iron, iron oxides, and different coal ranks. Adapted from [10].	3
3.1.	Initial conditions for particles and fluid, the subscript 0 stands for initial. $\;$.	24
4.2.	Calculation of the input quantities N_{part} and H_{in}	
4 4	and $\Phi = 0.8$, under the grid system $N_b = (10, 10, 100)$ Dimensionless numbers at initial time step for the three simulations at $P = 1$	55
1.1.	atm, $T_u = 500$ K, and $\Phi = 0.8$, under the grid system $N_b = (10, 10, 100)$.	55

Bibliography

- [1] International Energy Agency, "Energy efficiency 2024", IEA, Paris, Tech. Rep., 2024, Licence: CC BY 4.0. [Online]. Available: https://www.iea.org/reports/energy-efficiency-2024.
- [2] IEA Energy End-uses and Efficiency Indicators database (EEI), "Energy end-uses and efficiency indicators data explorer", IEA, Tech. Rep., 2025, Licence: CC BY 4.0.
- [3] J. M. Bergthorson, "Recyclable metal fuels for clean and compact zero-carbon power", *Progress in Energy and Combustion Science*, vol. 68, pp. 169–196, 2018, DOI: 10.1016/j.pecs.2018.05.001.
- [4] P. Julien and J. M. Bergthorson, "Enabling the metal fuel economy: Green recycling of metal fuels", *Sustainable Energy Fuels*, vol. 1, pp. 615–625, 3 2017, DOI: 10.1039/C7SE00004A.
- [5] W. M. Budzianowski, "Value-added carbon management technologies for low co2 intensive carbon-based energy vectors", *Energy*, vol. 41, no. 1, pp. 280–297, 2012, 23rd International Conference on Efficiency, Cost, Optimization, Simulation and Environmental Impact of Energy Systems, ECOS 2010, DOI: https://doi.org/10.1016/j.energy.2012.03.008.
- [6] C. Kuhn et al., "Iron as recyclable energy carrier: Feasibility study and kinetic analysis of iron oxide reduction", *Applications in Energy and Combustion Science*, vol. 9, p. 100096, 2022, DOI: 10.1016/j.jaecs.2022.100096.
- [7] N. Auner and S. Holl, "Silicon as energy carrier—facts and perspectives", *Energy*, vol. 31, no. 10, pp. 1395–1402, 2006, DOI: 10.1016/j.energy.2005.12.001.
- [8] K. A. Trowell et al., "Aluminum and its role as a recyclable, sustainable carrier of renewable energy", *Applied Energy*, vol. 275, p. 115112, 2020, DOI: 10.1016/j.apen ergy.2020.115112.
- [9] S. Buchheiser et al., "Particle and phase analysis of combusted iron particle for energy storage and release", *Materials*, vol. 16, no. 5, p. 2009, 2023, DOI: 10.3390/m a16052009.
- [10] P. Debiagi et al., "Iron as a sustainable chemical carrier of renewable energy: Analysis of opportunities and challenges for retrofitting coal-fired power plants", *Renewable and Sustainable Energy Reviews*, vol. 165, p. 112579, 2022, DOI: 10.1016/j.rser.2022.112579.
- [11] K. R. Ngoy et al., "Lithium-ion batteries and the future of sustainable energy: A comprehensive review", *Renewable and Sustainable Energy Reviews*, vol. 223, p. 115 971, 2025, DOI: 10.1016/j.rser.2025.115971.
- [12] M. Gao et al., "A redox-mediated iron-air fuel cell for sustainable and scalable power generation", *Advanced Energy Materials*, vol. 13, no. 38, p. 2301868, 2023, DOI: https://doi.org/10.1002/aenm.202301868, eprint: https://advanced.onlinelibrary.wiley.com/doi/pdf/10.1002/aenm.202301868.
- [13] T. Lachaux et al., "Flame front analysis of high-pressure turbulent lean premixed methane—air flames", *Proceedings of the Combustion Institute*, vol. 30, no. 1, pp. 819–826, 2005, DOI: https://doi.org/10.1016/j.proci.2004.08.191.

- [14] J. F. Driscoll, "Turbulent premixed combustion: Flamelet structure and its effect on turbulent burning velocities", *Progress in Energy and Combustion Science*, vol. 34, no. 1, pp. 91–134, 2007, DOI: 10.1016/j.pecs.2007.04.002.
- [15] F. T. C. Yuen and Ö. L. Gülder, "Premixed turbulent flame front structure investigation by rayleigh scattering in the thin reaction zone regime", *Proceedings of the Combustion Institute*, vol. 32, no. 2, pp. 1747–1754, 2009, DOI: 10.1016/j.proci.20 08.08.005.
- [16] S. Ranganathan, "Influence of dusts on premixed methane-air flames", Ph.D. dissertation, Worcester Polytechnic Institute, 2018.
- [17] W. Song, F. E. Hernández Pérez, and H. G. Im, "Turbulent hydrogen flames: Physics and modeling implications", in *Green Energy and Technology*, Springer, 2023.
- [18] H. Shehab et al., "Morphology and structure of spherically propagating premixed turbulent hydrogen—air flames", *Combustion and Flame*, vol. 238, p. 111888, 2022, DOI: 10.1016/j.combustflame.2021.111888.
- [19] K. N. C. Bray, P. A. Libby, and J. B. Moss, "Unified modeling approach for premixed turbulent combustion—part i: General formulation", Combustion and Flame, vol. 61, no. 1, pp. 87–102, 1985, DOI: 10.1016/0010-2180(85)90075-6.
- [20] P. A. Libby, "Theory of normal premixed turbulent flames revisited", Progress in Energy and Combustion Science, vol. 11, no. 1, pp. 1–30, 1985, DOI: 10.1016/0360– 1285(85)90014-0.
- [21] G. Damköhler, "Der einfluss der turbulenz auf die flammengeschwindigkeit in gasgemischen", Zeitschrift für Elektrochemie und angewandte physikalische Chemie, vol. 46, no. 11, pp. 601–626, 1940.
- [22] N. Peters, Turbulent Combustion. Cambridge University Press, Aug. 2000, DOI: 10.1017/CB09780511840531.
- [23] N. N. Semenov, "Some problems relating to chain reactions and to the theory of combustion", in *Nobel Lecture*, 1956.
- [24] Y. B. Zeldovich, "Theory of flame propagation", National Advisory Committee for Aeronautics, 1951.
- [25] T. Poinsot and D. Veynante, "Theoretical and numerical combustion", *Prog. Energy Combust. Sci.*, vol. 28, Jan. 2005.
- [26] Z. Tian et al., "Spatially resolved laser-induced breakdown spectroscopy in laminar premixed methane—air flames", Spectrochimica Acta Part B: Atomic Spectroscopy, vol. 136, Aug. 2017, DOI: 10.1016/j.sab.2017.08.001.
- [27] N. Peters, Fifteen Lectures on Laminar and Turbulent Combustion. Aachen: RWTH Aachen, 1992.
- [28] G. von Elbe and B. Lewis, "Theory of ignition, quenching and stabilization of flames of nonturbulent gas mixtures", *Symposium on Combustion and Flame, and Explosion Phenomena*, vol. 3, no. 1, pp. 68–79, 1948, DOI: 10.1016/S1062-2896(49)80009-2.
- [29] Skiba et al., "Premixed flames subjected to extreme levels of turbulence part ii: Surface characteristics and scalar dissipation rates", *Combustion and Flame*, vol. 239, p. 111703, Sep. 2021, DOI: 10.1016/j.combustflame.2021.111703.
- [30] F. A. Williams, Combustion Theory: The Fundamental Theory of Chemically Reacting Flow Systems, 2nd ed. CRC Press, 2018, DOI: 10.1201/9780429494055.
- [31] M. Liberman, Combustion Physics: Flames, Detonations, Explosions, Astrophysical Combustion and Inertial Confinement Fusion. Springer, 2021, DOI: 10.1007/978-3-030-85139-2.

- [32] A. J. Aspden, M. S. Day, and J. B. Bell, "Turbulence-chemistry interaction in lean premixed hydrogen combustion", *Proceedings of the Combustion Institute*, vol. 35, no. 2, pp. 1321–1329, 2015, DOI: 10.1016/j.proci.2014.08.012.
- [33] Ö. L. Gülder, "Contribution of small scale turbulence to burning velocity of flamelets in the thin reaction zone regime", *Proceedings of the Combustion Institute*, vol. 31, no. 1, pp. 1369–1375, 2007, DOI: 10.1016/j.proci.2006.07.189.
- [34] T. Kulkarni and F. Bisetti, "Surface morphology and inner fractal cutoff scale of spherical turbulent premixed flames in decaying isotropic turbulence", *Proceedings of the Combustion Institute*, vol. 38, no. 2, pp. 2861–2868, 2021, DOI: 10.1016/j.proci.2020.06.117.
- [35] T. Kulkarni et al., "Reynolds number scaling of burning rates in spherical turbulent premixed flames", *Journal of Fluid Mechanics*, vol. 906, 2021, DOI: 10.1017/jfm.2020.784.
- [36] E. R. Hawkes, R. Sankaran, and J. H. Chen, "Estimates of the three-dimensional flame surface density and every term in its transport equation from two-dimensional measurements", *Proceedings of the Combustion Institute*, vol. 33, no. 1, pp. 1447–1454, 2011, DOI: https://doi.org/10.1016/j.proci.2010.06.019.
- [37] K. N. C. Bray and R. S. Cant, "Some applications of kolmogorov's turbulence research in the field of combustion", Proceedings of the Royal Society of London A, vol. 434, no. 1890, pp. 217–240, 1991.
- [38] G. H. Markstein, "Experimental and theoretical studies of flame-front stability", Journal of the Aeronautical Sciences, vol. 18, no. 3, pp. 199–209, 1951, DOI: 10.2514 /8.1900.
- [39] S. Demesoukasa et al., "0d modeling aspects of flame stretch in spark ignition engines and comparison with experimental results", *Applied Energy*, 2016, In press at time of citation.
- [40] G. Thäter et al., "The influence of clustering in homogeneous isotropic turbulence on the ignition behavior of iron particles", *Proceedings of the Combustion Institute*, 2024, In press.
- [41] T. Luu et al., "Carrier-phase dns of ignition and combustion of iron particles in a turbulent mixing layer", Flow, Turbulence and Combustion, vol. 112, pp. 1083–1103, 2024, DOI: 10.1007/s10494-023-00526-y.
- [42] J. Mich et al., "A comparison of mechanistic models for the combustion of iron microparticles and their application to polydisperse iron-air suspensions", *Combustion and Flame*, Apr. 2023, DOI: 10.48550/arXiv.2304.14927.
- [43] A. Panahi et al., "Combustion behavior of single iron particles—part i: An experimental study in a drop-tube furnace under high heating rates and high temperatures", *Applications in Energy and Combustion Science*, vol. 13, p. 100 097, 2023, DOI: 10.1016/j.jaecs.2022.100097.
- [44] A. Fujinawa et al., "Combustion behavior of single iron particles, part ii: A theoretical analysis based on a zero-dimensional model", *Applications in Energy and Combustion Science*, vol. 14, p. 100145, 2023, DOI: 10.1016/j.jaecs.2023.100145.
- [45] M. A. Benitz, M. A. Lackner, and D. P. Schmidt, "Hydrodynamics of offshore structures with specific focus on wind energy applications", *Renewable and Sustainable Energy Reviews*, vol. 44, pp. 591–604, 2015. [Online]. Available: https://www.sciencedirect.com/journal/renewable-and-sustainable-energy-reviews.

- [46] J. Roenby, H. Bredmose, and H. Jasak, "A computational method for sharp interface advection", Royal Society Open Science, vol. 3, p. 160405, 2016, DOI: 10.1098/rsos .160405.
- [47] E. Olsson, "A description of isoadvector—a numerical method for improved surface sharpness in two-phase flows", in *Proceedings of CFD with OpenSource Software*, H. Nilsson, Ed., 2017, DOI: 10.17196/OS_CFD.
- [48] Q. Chen et al., "Recent progress of gas diffusion layer in proton exchange membrane fuel cell: Two-phase flow and material properties", *International Journal of Hydrogen Energy*, vol. 46, no. 12, pp. 8640–8671, 2021, DOI: 10.1016/j.ijhydene.2020.12.0 76.
- [49] J. López, "Isosurface extraction for piecewise-linear reconstruction of complex interfaces on arbitrary grids", Computer Methods in Applied Mechanics and Engineering, vol. 427, p. 116951, 2024, DOI: 10.1016/j.cma.2024.116951.
- [50] J. López et al., "A new volume of fluid method in three dimensions—part ii: Piecewise-planar interface reconstruction with cubic-bézier fit", *International Journal for Numerical Methods in Fluids*, vol. 58, no. 8, pp. 923–944, 2008, DOI: 10.1002/fld.1 775.
- [51] Z. Long and K. Nagamune, "A marching cubes algorithm: Application for three-dimensional surface reconstruction based on endoscope and optical fiber", *Information (Japan)*, vol. 18, pp. 1425–1437, Apr. 2015.
- [52] Kobbelt et al., "Feature sensitive surface extraction from volume data", Proceedings of the ACM SIGGRAPH Conference on Computer Graphics, Aug. 2001, DOI: 10.114 5/383259.383265.
- [53] T. S. Newman and H. Yi, "A survey of the marching cubes algorithm", Computers & Graphics, vol. 30, no. 5, pp. 854-879, 2006, DOI: https://doi.org/10.1016/j.cag.2006.07.021.
- [54] F. H. Harlow, "Pic and its progeny", Computer Physics Communications, vol. 48, no. 1, pp. 1–10, 1988, DOI: 10.1016/0010-4655(88)90017-3.
- [55] J. M. Dawson, "C", Reviews of Modern Physics, vol. 55, no. 2, pp. 403–447, 1983, DOI: 10.1103/RevModPhys.55.403.
- [56] L. F. Ricketson and A. J. Cerfon, "Sparse grid techniques for particle-in-cell schemes", arXiv preprint, 2016, eprint: arXiv:1607.07452 (physics.comp-ph).
- [57] U. Ahmed, N. Chakraborty, and M. Klein, "Assessment of bray—moss—libby formulation for premixed flame-wall interaction within turbulent boundary layers: Influence of flow configuration", *Combustion and Flame*, 2021, www.elsevier.com/locate/combustflame.
- [58] U. Ahmed et al., "On the validity of damköhler's second hypothesis in statistically planar turbulent premixed flames in the thin reaction zones regime", *Proceedings of the Combustion Institute*, vol. 38, no. 2, pp. 3039–3047, 2021, DOI: 10.1016/j.proci.2020.07.128.
- [59] W. K. Blake, Mechanics of Flow-Induced Sound and Vibration, Volume 2, 2nd ed. Academic Press, 2017.

Appendix

A. Premixed Flames

A.1. Bray-Moss-Libby model

In premixed turbulent combustion, the Bray-Moss-Libby (BML) model is a closure model for a scalar field, built on the assumption that the reaction sheet is infinitely thin compared with the turbulent scales, so that the scalar can be found either at the state of burnt gas or unburnt gas. When the reaction layer is not thin, a density function is built. This probabilistic framework allows a statistical description of the turbulent flame.

A.2. Bray-Cant Formulation Derivation

Starting from Damköhler's prediction, Bray and Cant developed the relation introducing the Flame Surface Density (FSD) and the stretch factor I_0 . In particular, they considered each point of the flame front to propagate in space at the local value of the turbulent flame speed $S_{T,F}$, which has a time-averaged value $\overline{S}_{F,T}$. Balancing the mass flux of reactants across the wrinkled surface and across the corresponding laminar front:

$$\rho_R \overline{S}_{F,T} A_T = \rho_R S_{F,T} A_L, \tag{5.1}$$

where ρ_R is the mass of reactants. It follows:

$$\frac{S_T}{S_{L,0}} = \frac{A_T}{A_L} \frac{\overline{S}_{F,C}}{S_{L,0}} = \frac{A_T}{A_L} I_0. \tag{5.2}$$

Bray and Cant defined the stretch factor I_0 and the flamelet consumption speed:

$$I_0 = \frac{\overline{S}_{F,C}}{S_{L,0}}, \qquad S_{F,C} = \frac{1}{\rho_R} \int \omega_R \, d\xi,$$

where ω_R is the reaction rate and ξ is the coordinate normal to the reaction layer. In a slice dV, the wrinkled area is

$$A_T = \int_{-\infty}^{+\infty} \Sigma \, dV = \int_{-\infty}^{+\infty} \Sigma (A_L \, d\eta).$$

Substituting this definition of A_T into the expression for $S_T/S_{L,0}$ yields the Bray-Cant relation.

A.3. Markstein Number

This expression appears in the equation of conservation of the FSD. Due to thermal expansion, the value of $S_{T,LD}$ changes significantly and to minimize this enhancement the density weighted form is defined as $S_{T,LD}^* = \rho S_{T,LD}/\rho_u$. He introduced then a probability density function (PDF) for selected iso-surfaces that propagates at $S_{T,LD}^*$.

Perez demonstrated that the PDF of the local displacement rate over the laminar one is often close to unity, to confirm that locally the flamelet structures are composed of more laminar flames. The distribution of the PDF shows that $S_{T,LD}^*$ is influenced by the local flame strain rate. Thus it is possible to find a relation with the flame curvature and the stretch rate, by means of the Markstein numbers. The resulting expression is a generalized form of the flame speed for the entire iso-surface, known also as Giannakopoulos model:

$$S_d^*(\theta^*) = S_L - L_K(\theta^*) \, \mathcal{K} - L_\kappa(\theta^*) \, S_L \kappa, \tag{5.3}$$

Where $L_{\mathcal{K}}$ is the stretch Markestein length, L_K is the curvature Markstein length, \mathcal{K} tangential strain rate and $\kappa = \nabla \cdot \mathbf{n}$, the flame curvature with $\mathbf{n} = -\nabla T/|\nabla T|$ and $\theta^* = T_0/T_u$ with T_0 is the temperature of the iso-surface. For a laminar flame, the effect of stretch is expressed as:

$$\frac{S_L}{S_{L,0}} = 1 - Ma_L K \left(\frac{S_{L,0}^2}{\alpha} \right), \tag{5.4}$$

where Ma_L is the laminar Markstein number, K the stretch rate, and α the thermal diffusivity. For turbulent flames, two additional forms are often introduced:

$$\frac{S_{F,C}}{S_{L,0}} = 1 - Ma_F K \left(\frac{S_{L,0}^2}{\alpha_0}\right),\tag{5.5}$$

$$I_0 = \frac{S_{F,C}}{S_{L,0}} = 1 - Ma_T \frac{u'}{l} \left(\frac{S_{L,0}^2}{\alpha_0} \right), \tag{5.6}$$

with Ma_F the flamelet Markstein number and Ma_T the turbulent Markstein number.

B. Further developments of model equations

In this appendix, additional relations used in the iron-particle DNS model are collected. They complement the main governing equations presented in the methodology chapter, providing the explicit formulation of fluid stresses, particle–fluid exchange terms, and closure correlations for heat and mass transfer.

The viscous stress tensor that appears in the mean dissipation rate 3.9 is expressed in the usual Newtonian form:

$$\tau_{ij} = \mu \left(\frac{\partial u_i}{\partial x_j} + \frac{\partial u_j}{\partial x_i} - \frac{2}{3} \delta_{ij} \frac{\partial u_k}{\partial x_k} \right). \tag{5.7}$$

Where u_i , u_j and u_k are the three Cartesian components of fluid velocity expressed in $[\text{m s}^{-1}]$, μ the fluid viscosity in [Pas] and δ_{ij} the Kronecker delta (= 1 if i = j, = 0 otherwise).

Particle—fluid interactions are introduced through point-wise source terms appearing in the gas-phase mass, momentum and enthalpy balances, respectively 3.3a, 3.3c and 3.3d:

$$S_{O_2} = -\sum_{p=1}^{N_P} \frac{dm_{O_2}}{dt} \,\delta\left(\vec{x} - \vec{x}_p\right),\tag{5.8}$$

$$S_{i,u} = -\sum_{p=1}^{N_P} \left(F_{i,\text{drag}} + \frac{dm_{O_2}}{dt} u_i \right) \delta(\vec{x} - \vec{x}_p), \qquad (5.9)$$

$$S_H = -\sum_{p=1}^{N_P} \left(\dot{Q}_{\text{conv}} + \dot{Q}_{\text{rad}} \right) \delta \left(\vec{x} - \vec{x}_p \right). \tag{5.10}$$

where $\dot{Q}_{\rm rad}$ and $\dot{Q}_{\rm conv}$ are the radiative and convective heat flux respectively in [W]. $\delta(\vec{x}-\vec{x}_p)$ is the Dirac delta (localization) and $F_{i,\rm drag}$ the drag force on particle expressed in [N]. Here S_{O_2} represents the local sink of oxygen, $S_{i,u}$ the momentum exchange through drag and mass transfer, and S_H the enthalpy source due to convective and radiative heat release from particles.

The temporal evolution of particle properties is governed by momentum, mass and energy balances, respectively 3.5d, 3.5a, 3.5b and 3.5c. The particle enthalpy variation reads:

$$\frac{dH_p}{dt} = -k_c A_p \left(T_p - T|_{\vec{x}_p} \right) + \dot{Q}_{\text{rad}} + \frac{dm_p}{dt} h_{O_2}(T_p), \tag{5.11}$$

where convective heat transfer (k_c convective heat transfer coefficient [W/(m²K)]) over particle surface A_p , radiation $\dot{Q}_{\rm rad}$ and specific enthalpy of oxygen fluxes at particle temperature $h_{O_2}(T_p)$ [J kg⁻¹] are included.

The particle velocity obeys:

$$\frac{du_{i,p}}{dt} = \frac{u_i|_{\vec{x}_p} - u_{i,p}}{m_p} \left[3\pi\mu d_p \left(1 + 0.15 Re_p^{0.687} \right) + \frac{dm_p}{dt} \right], \tag{5.12}$$

which incorporates Stokes drag corrected for finite Reynolds number and momentum variation due to surface mass flux.

The particle temperature is assumed uniform (small Biot number, $Bi \approx 0.001$ –0.01). Its balance is given by:

$$\frac{dT_p}{dt} = \frac{1}{\tau_{\text{conv}}} (T_g - T_p) + \frac{\varepsilon_p A_p \sigma}{m_p c_{p,p}} \left(\Theta_r^4 - T_p^4 \right) + \frac{\dot{Q}_{\text{FeO}}}{m_p c_{p,p}} + \frac{\dot{Q}_{O_2}}{m_p c_{p,p}}.$$
 (5.13)

Where \dot{Q}_{FeO} , \dot{Q}_{O_2} are the heat release from oxidation [W], Θ_r the radiative reference temperature [K], ε_p the particle emissivity [-] and T_g the has temperature [K]. τ_{conv} is the convective timescale [s], expressed as:

$$\tau_{\text{conv}} = \frac{1}{6} Pr \frac{Nu \, c_{p,p}}{c_{p,f}} \cdot \frac{\rho_p d_p^2}{\mu_f}$$
 (5.14)

where Nu is the Nusselt dimensionless number and follows the Ranz–Marshall correlation [40], and Pr is the Prandtl dimensionless number. Finally, the total particle mass and momentum balances are:

$$\frac{dm_p}{dt} = \frac{dm_{p,\text{Fe}}}{dt} + \frac{dm_{p,\text{FeO}}}{dt},\tag{5.15}$$

$$\frac{d\mathbf{u}_p}{dt} = \frac{\mathbf{u}_g - \mathbf{u}_p}{\tau_p}.\tag{5.16}$$

The particle relaxation time is expressed as:

$$\tau_p = \frac{\rho_p d_p^2}{18\mu_f} \cdot \frac{1}{\left(1 + 0.15Re_p^{2/3}\right)},\tag{5.17}$$

The heterogeneous surface reaction is described by a competition between a kinetic and a diffusive rate:

$$k_r = k_\infty \, \exp\left(-\frac{E_a}{R_u T_p}\right),\tag{5.18}$$

$$k_d = \frac{Sh \, D_{O_2, f}}{d_p}.\tag{5.19}$$

Here k_r is the Arrhenius kinetic rate, k_d the diffusive transfer rate, and Sh the Sherwood number:

$$Sh = 2 + 0.552 Re_p^{1/2} Sc^{1/3}. (5.20)$$

Where Sc is the Schimdt number. The Reynolds number of a particle is defined as

$$Re_p = \frac{\rho_f |\mathbf{u}_g - \mathbf{u}_p| d_p}{\mu_f},\tag{5.21}$$

while the film temperature is evaluated by the one-third rule:

$$T_f = T_p + \frac{1}{3} (T_g - T_p).$$
 (5.22)

The stoichiometric ratio s refers to the oxidation of iron to iron oxide (Fe \rightarrow FeO). Corrected transfer numbers are obtained through the Spalding [40] formulation:

$$Sh^* = Sh \frac{\ln(1 + B_M)}{B_M}, \qquad Nu^* = Nu \frac{\ln(1 + B_T)}{B_T},$$
 (5.23)

where B_M and B_T are the Spalding mass and heat transfer numbers, respectively.

B.1. Voronoi Tesselation

The Voronoi tessellation is a geometric partition of space around a set of points: each particle is assigned a polyhedral cell containing all locations closer to that particle than to any other. In three dimensions, the cell volume provides a local measure of concentration: small volumes indicate clustered regions, whereas large volumes indicate dilute regions.

In this work, the tessellation is used to quantify clustering without prescribing an arbitrary length scale. The Voronoi volume is normalized by its mean value, and the resulting probability density function of $v/v_{\rm mean}$ is compared against a Poisson (random) reference; pronounced tails toward very small and very large volumes signal preferential concentration. Additionally, correlating $v/v_{\rm mean}$ with thermochemical quantities (e.g., particle temperature and reaction progress) shows that particles in small-volume cells tend to ignite first, linking clustering, convective heat transport, and the observed reduction in ignition delay.

C. Additional plots

C.1. Fluid isothermal lines

Different threshold values for the fluid temperature have been tested. Figure C.1 shows that at lower thresholds the linearity does not change significantly, while at higher thresholds the behavior follows what was already noted for the isothermal lines obtained from particle temperatures. In any case, the linearity achieved is much better than that obtained using particle grid values.

The plot in Figure C.2 displays the laminar speed velocity is also reported to show the overall expected trend of the flame speed with time: after a first acceleration a decreasing trend is expected. The final peak is artificial due to the algorithm setup.

Additionally, Figure C.3 compares the isotherm with the mean values and the Voronoi-weighted average is shown for the case with a lower particle number. In this plot, the MC output exhibits improved linearity and better agreement with the isotherm case. Consequently to this plot the behavior of the algorithm to the particles number raised the interest.

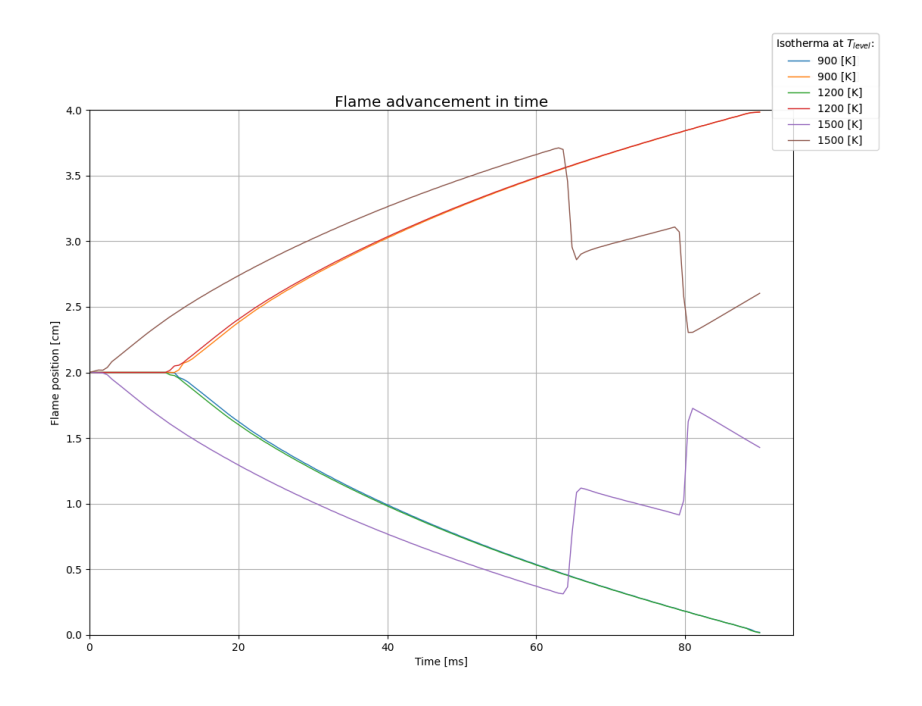


Figure C.1.: Flame position over time computed as the fluid iso-thermal curves at different temperature.

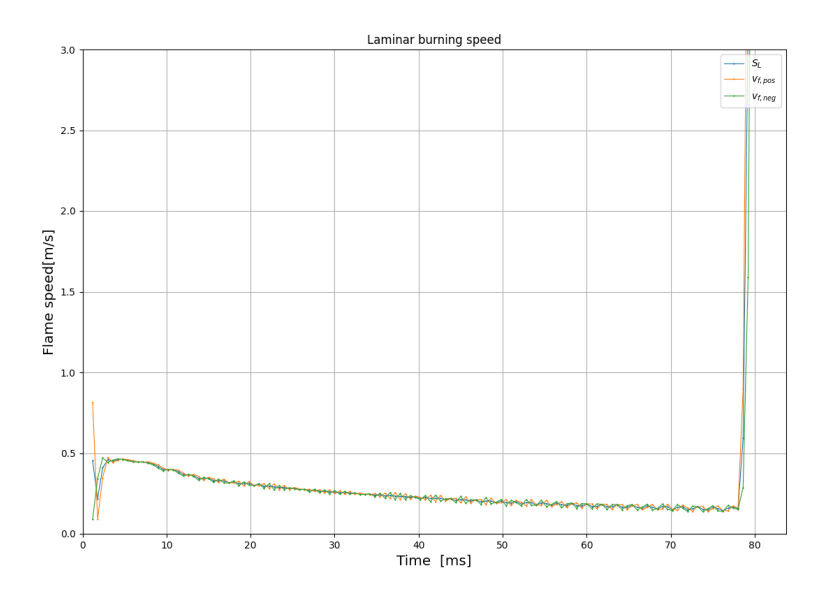


Figure C.2.: Laminar flame speed over time computed with the iso-l line.

C.2. Flame thickness definition

The second method used to compute the flame thickness is based on the vertices obtained as output from the MC algorithm. The thickness is calculated as the average distance between the two flame fronts into which the flame is divided due to the setup of the simulation. Each front thickness is computed as the amplitude of the z-coordinates of the corresponding vertices. It must be noted that this definition is applicable only in the laminar case, where homogeneous propagation is expected.

In the second approach, the thickness is again computed from the vertices of the iso-surface.

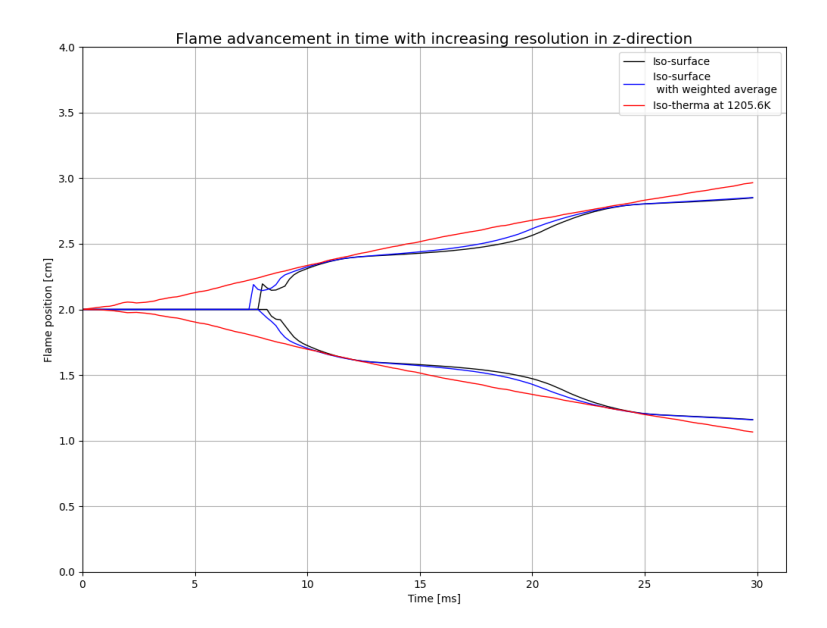


Figure C.3.: Laminar case of simulation setup with $\Phi=0.5$. Flame position evolution in time with isothermal, mean value and weighted average approach. Resolution of $N_{b,z}=10$ and $C_{ox}^{level}=0.5$.

This definition is valid for the present simulation case, where the flame front splits into two homogeneous surfaces. In this case, the thickness is defined as the standard deviation of the z-coordinates of the vertices for each front.

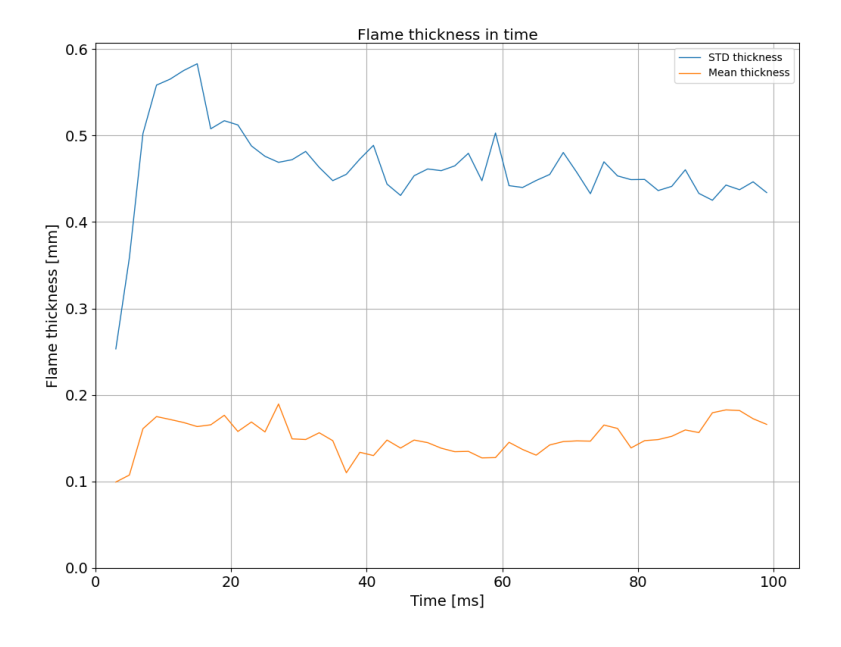


Figure C.4.: Flame thickness for the laminar case simulation. Grid $N_b = (10, 10, 100)$ and $C_{ox}^{level} = 0.5$.

Figure C.4 shows the temporal evolution of the flame thickness according to the two different definitions. The mean-based definition results in smaller values and reduced

fluctuations compared to the standard-deviation-based definition. This can be explained by the fact that, in the mean approach, the positive and negative fronts compensate for each other's fluctuations, leading to more stable results.

The flame thickness has also been related to turbulence intensity, i.e. the root-mean-square of the velocity fluctuations u', and to the integral turbulent length scale, L_T . The latter is defined as the characteristic length scale of turbulence that influences the spectrum levels of sound generated by turbulent flow, as indicated by integrated cross-spectral densities in relation to flow properties[59].

C.3. Different simulation setup

The three dimensional plots for the simulation at St = 3 (Fig. C.5) and St = 5 (Fig. C.6) are here shown to visualize the detected flame with MC algorithm.



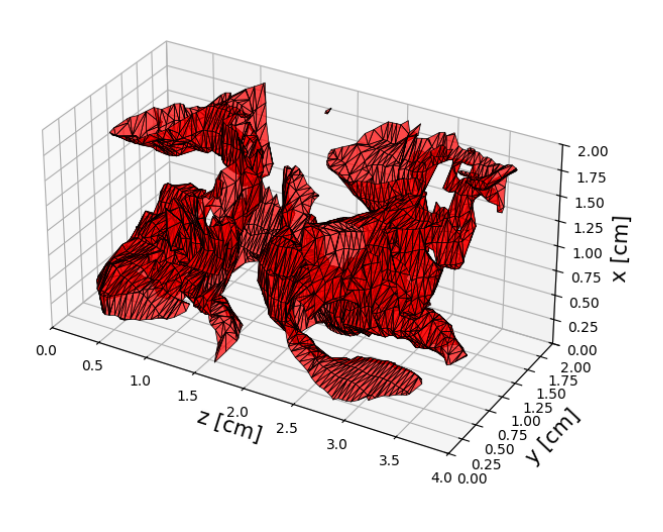


Figure C.5.: Turbulent case at St = 3: reconstructed iso-surface at $C_{ox}^{level} = 0.5$ with a grid $N_b = (10, 10, 100)$.

Isosurface at $C_{ox}^{level} = 0.5$

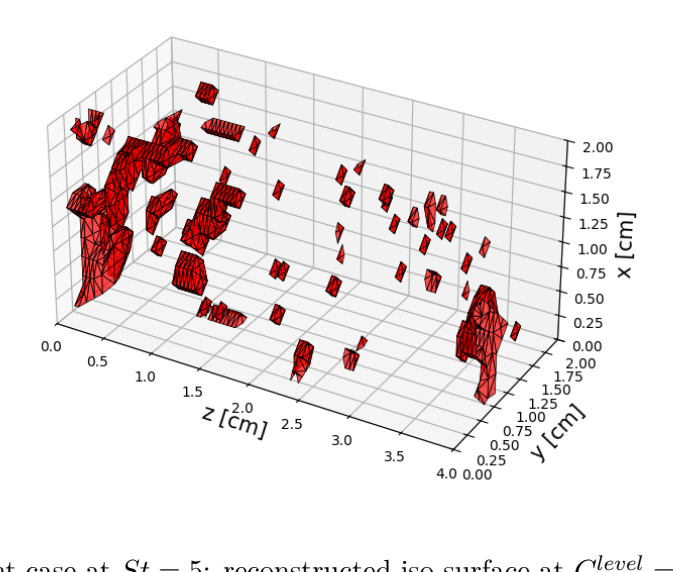


Figure C.6.: Turbulent case at St=5: reconstructed iso-surface at $C_{ox}^{level}=0.5$ with a grid $N_b=(10,10,100)$.